Probing water below the surface: Insights from seismic interferometry with conventional and DAS array

Thesis by
Zhichao Shen

In Partial Fulfillment of the Requirements for the
Degree of
Doctor of Philosophy

CALIFORNIA INSTITUTE OF TECHNOLOGY
Pasadena, California

2022
Defended April 25, 2022

Zhichao Shen
ORCID: 0000-0003-0458-5264

To my beloved family

ACKNOWLEDGEMENTS

"Philosophy is a battle against the bewitchment of our intelligence by means of language" - Ludwig Wittgenstein. Throughout my Ph.D. journey, I was very fortunate to have been surrounded by the encouragement, patience, and generosity of many people.

First and foremost, the completion of my dissertation would not have been possible without the support and nurturing of my advisor Zhongwen Zhan. It is his trust, wisdom and passion that opened my mind to geophysics, cultivated my critical thinking on how seismology can contribute to a broader science community, and inspired me to continue pursuing an academic path after graduation. Much thanks also goes to him for his support during the COVID-19 pandemic, in particular when I was encountering a hard time.

I would also like to express my deepest gratitude to Jennifer Jackson, Micheal Gurnis, and Robert Clayton for serving as my committee members and keeping me on track with research. Thanks to Jennifer for being a great academic advisor and collaborator, looping me into the Deep Earth reading group and offering me mineralogical insights when I was floundering. Thanks to Mike for his patient guidance on helping me set up geodynamic simulations and for intellectual discussions during coffee hour. Thanks to Rob for involving me in urban nodes deployments and sending me the postdoc advertisements. In addition, I would like to extend my sincere thanks to Caltech faculty members: Mark Simons, Joann Stock, Jean-Philippe Avouac, Zachary Ross, Nadia Lapusta, Ruby Fu, and Victor Tsai. I have learnt a lot from them through classes, research, reading groups and coffee hours.

I am grateful for the assistance and support from Kim, Priscilla, Donna, Rosemary, Sarah, Ken, and Scott. Special thanks also go to my friends and colleagues in and outside the Seismo Lab. To dear South Mudd 362: Semechah Lui, Voonhui Lai, Jorge Alberto Castillo Castellanos, Kangcheng Bai, Yuan-kai Liu, Jack Muir, and Lenoid Pereiaslov for your company and entertaining moments. To my phenomenal graduate classmates: Zhe Jia, Stacy Larochelle, Vasilije Dobrosavljevic, Ollie Stephenson, Celeste Labedz, and Valere Lambert for taking care of each other over the past few years. In particual, to Zhe being a classmate, friend, and colleague for so many years since USTC. To the superb Seismo Fam for the memorable moments and for making me feel like I am at home. I will miss you all for sure.

I am also deeply indebted to my former advisor Sidao Ni for first introducing me to seismology, inspiring me with smiles, and helping me to overcome hardship. To Wenbo for constantly discussing research with me and offering me proper life advice. I am grateful for such a long friendship.

Much thanks also go to my friends outside the lab: Cheng Zhang, Ziwei Li, Junyi Shan, Wenlong Ma, Jin Sima, Marcel Veismann, Amanda Bouman, Vinayak Narasimhan, and Abbas Tutcuoglu for their continual help and support. To Peyman, Austin, Parham, Reza, Aryan, Nader, and Saif for having me as a teammate playing soccer together every week. Last but not least to the USC crew for playing poker on weekends and enriching my Ph.D. life with joys.

Finally, I would like to give my most heartfelt gratitude to my parents and my whole extended family. Thank you for your unconditional love, for raising me, for educating me with the best resources, for believing in my decisions, and for having faith in my success. Without you, this couldn't have been possible.

ABSTRACT

Water is essential to our daily lives, yet its subsurface behavior remains challenging to track using remote observations. By extracting seismic waves traveling through the Earth, seismic interferometry is a powerful tool to image the Earth's interior, in particular the long-term and short-term behavior of water circulation. With conventional dense seismic networks and emerging distributed acoustic sensing (DAS), I demonstrate how seismic interferometry brings new insights on water below the surface ranging from the depths of the mantle transition zone (MTZ) to the subsurface aquifers of our planet.

By applying a novel inter-source interferometry method that turns deep earthquakes into virtual seismometers, I not only present evidence for an intermediate-scale metastable olivine wedge and small-scale intra-slab scatterers in the MTZ beneath the Japan Sea, but also reveal their dimensions and velocity perturbations more accurately than before. Beyond the relative independent scales of slab structures, these results point toward a consistent picture of transformational faulting of metastable olivine as the initiation mechanism of deep earthquakes, petrologic processes associated with dehydration of subducting slabs, and an extremely dry slab core below 410-km. Borrowing the idea from inter-source interferometry, I develop a slab operator method by utilizing the waveform broadening due to the high-velocity anomaly. With synthetic tests and real data, I illustrate the feasibility of this method for accurately determining large-scale slab velocity perturbations.

Shifting from the Earth's interior to the subsurface, I investigate the feasibility of vadose zone water monitoring with DAS. DAS provides an affordable and scalable solution for deploying ultra-dense seismic arrays by transforming existing optic-fiber cables into thousands of seismic sensors. With two years of ambient noise recorded on the Ridgecrest DAS array, the time-lapse images of seismic changes (dv/v) reveal an unprecedented high-resolution spatiotemporal evolution of water saturation in vadose zone. A striking correlation between the dv/v amplitude and the sedimentary thickness is observed, while the frequency analysis of dv/v measurements suggests an uppermost 10 m hydrologic source as the cause for dv/v temporal variability. The results demonstrate the great potential of DAS for long-term subsurface water monitoring.

PUBLISHED CONTENT AND CONTRIBUTIONS

Atterholt, J., Z. Zhan, **Shen, Zhichao**, and Z. Li (2022). A unified wavefield-partitioning approach for distributed acoustic sensing. In: *Geophysical Journal International* 228.2, pp. 1410–1418. DOI: 10.1093/gji/ggab407.
`Z.S. processed the seismic data and performed the analysis.`

Yang, Y., J. W. Atterholt, **Shen, Zhichao**, J. B. Muir, E. F. Williams, and Z. Zhan (2022). Sub-kilometer correlation between near-surface structure and ground motion measured with distributed acoustic sensing. In: *Geophysical Research Letters*, e2021GL096503. DOI: 10.1029/2021GL096503.
`Z.S. processed the seismic data and performed the analysis.`

Li, Z., **Shen, Zhichao**, Y. Yang, E. Williams, X. Wang, and Z. Zhan (2021). Rapid response to the 2019 Ridgecrest earthquake with distributed acoustic sensing. In: *AGU Advances* 2.2, e2021AV000395. DOI: 10.1029/2021AV000395.
`Z.S. processed the seismic data and performed the analysis.`

Shen, Zhichao, Z. Zhan, and J. M. Jackson (2021). Small-scale intra-slab heterogeneity weakens into the mantle transition zone. In: *Geophysical Research Letters*, e2021GL094470. DOI: 10.1029/2021GL094470.
`Z.S. processed the seismic data, performed the analysis, and wrote the manuscript. Z.Z. conceptualized the project. J.J. contributed to the interpretation of the results and participated in writing the paper.`

Jia, Z., **Shen, Zhichao**, Z. Zhan, C. Li, Z. Peng, and M. Gurnis (2020). The 2018 Fiji Mw 8.2 and 7.9 deep earthquakes: One doublet in two slabs. In: *Earth and Planetary Science Letters* 531, p. 115997. DOI: 10.1016/j.epsl.2019.115997.
`Z.S. contributed to the seismic data analysis, prepared figures and edited the manuscript.`

Shen, Zhichao and Z. Zhan (2020). Metastable olivine wedge beneath the Japan Sea imaged by seismic interferometry. In: *Geophysical Research Letters* 47.6, e2019GL085665. DOI: 10.1029/2019GL085665.
`Z.S. processed the seismic data, performed the analysis, and wrote the manuscript. Z.Z. conceptualized the project.`

TABLE OF CONTENTS

LIST OF ILLUSTRATIONS

Number *Page*

LIST OF TABLES

Number *Page*

Chapter 1

INTRODUCTION

Water is all around us in all its forms, from the atmosphere to the oceans, to lakes, to rivers, to snow and glaciers, and chemically bound into mineral crystal structures. Water is deemed essential to nearly every natural process on Earth, such as supporting terrestrial life on a biological level and regulating climate across the globe, thus rendering the compound one of the most intriguing for investigations. Not only above and on the Earth's surface, but water also exists below the surface. For instance, soil moisture controls the heat and energy exchange between the atmosphere and solid earth, water in unsaturated vadose zone can feed plants, and groundwater is the largest freshwater reservoir for domestic, agricultural, and industrial use. In the Earth's interior, even though no longer present as H_2O molecules, water is abundant in the form of hydrogen dissolved in various minerals, providing important information on the evolution of plate tectonics and volcanism throughout the history (Peslier et al., 2017; Ohtani, 2020). However, because of its remoteness, subsurface water is challenging to detect using remote observations.

Meanwhile, seismology overcomes some of these challenges. Emmitted from earthquake or other vibrational sources, seismic waves travel through the Earth and are recorded by seismometers, thus providing subtle signatures of the interior regions that they sample. By exploiting the details of seismic recordings, seismology provides a feasible way to make the invisible visible. For instance, earthquake traveltime-based tomography has successfully revealed the ultimate fate of subducted slabs in the mantle (Fukao and Obayashi, 2013). Rather than waiting for earthquakes to occur, seismic interferometry extraordinarily extends seismologists' arsenal by taking advantage of noise data. In general, seismic interferometry can be classified into inter-receiver interferomtery and inter-source interferometry. Inter-receiver interferometry reconstructs passive noise recordings into seismograms propagating from one receiver to the other, whereas inter-source interferometry transforms earthquakes into virtual sensors that record seismic signals from other real earthquakes (Galetti and Curtis, 2012). In this thesis, using both conventional seismic networks and an advanced distributed acoustic sensing (DAS) technology, I will demonstrate how seismic interferometry can help to gain new insights on water below the surface ranging from the depths of the mantle transition zone (MTZ)

(Chapters 2 through 4) to the subsurface aquifers (Chapter 5).

In Chapter 2, I investigate an intermediate-scale (10-100 km) seismic structure called metastable olivine wedge (MOW) which is significant for understanding the hydrous state within the slab core and the physics of deep earthquakes. For example, a small amount of water can break the existence of MOW, which would in turn rule out the transformational faulting hypothesis as the cause of deep earthquakes. However, the existence and dimension of MOW remains debatable because of its small size and remoteness. To overcome this challenge, I apply novel inter-source interferometry which converts deep earthquakes into virtual seismometers closer to our target without influence from shallow complexities. With real data, I not only present strong evidence for a metastable olivine wedge beneath the Japan Sea, but also constrain its dimension and velocity perturbation more accurately than before. This finding suggests that the MOW could be a initial mechanism for deep earthquakes, and indicates that only negligible amount of water can be transported into the MTZ, forming an extremely dry slab core below 410 km.

In Chapter 3, I study the small-scale (<10 km) heterogeneity within the subducted Japan slab. These intra-slab scatterers have been well documented in multiple subduction zones above 350 km, but their origin is elusive without unveiling their fate at greater depth (melt bands vs. hydrated faults). For instance, the intra-slab heterogeneity, if located along hydrated faults, can be much weaker at depth due to the slab dehydration. By turning some deep earthquakes into virtual sensors using inter-source interferometry, I find that the small-scale scatterers within the slab core fade substantially as slab subducts. The fading signal favors that the scatterers are caused by heterogeneous hydration of the slab in the outer rise that decreases as the slab core dehydrates. Combining with Chapter 2, the resolved slab structures, despite of their independent scales, point toward a consistent picture of a dry slab core below 410 km beneath the Japan Sea.

Borrowing the idea from inter-source interferometry, I develop a slab operator method for estimating the large-scale (>100 km) slab velocity perturbation in Chapter 4. The slab velocity perturbation is believed to reflect the slab thermal status which in turn affects the deep water cycle. For example, warm slab would become entirely anhydrous at subarc depths while cold slabs can transport water to MTZ. However, the absolute amplitude of slab velocity is ubiquitously underestimated by the traveltime based tomography. The slab operator method takes advantage of the fact that high-velocity slabs act similarly as an attenuation operator broadening waveforms. With 2D synthetics, I demonstrate that this method is capable of mea-

suring the slab velocity perturbation. With real data, I resolve a velocity amplitude of 4% for the subducted Kuril slab core. Nevertheless, the slab operator method still requires appropriate source-receiver configurations for global applications.

Shifting from the interior to the subsurface, I conduct seismic monitoring of the vadose zone water in Chapter 5. Water in the critical zone is particularly vital for sustaining life on Earth, but current monitoring techniques are mostly for surface water content with few probing below the surface. By reconstructing the surface waves propagating between two receivers on a daily base, inter-receiver interferometry provides a complimentary tool to fill in this gap. Yet, limited by the conventional seismic network spacing (tens of kilometers), only long wavelength surface waves can be retrieved, thus lacking depth resolution for vadose zone monitoring. As an emerging technology, DAS transforms the existing telecommunication optic-fiber cable into thousands of seismic sensors in a few meters spacing, opening a window for the uppermost subsurface monitoring. Taking the Ridgecrest DAS array as an example, I illustrate the feasibility of long-term vadose zone monitoring using DAS. The resulting time-lapse seismic images reveal an unprecedented high-resolution spatiotemporal evolution of water content in vadose zone.

References

Fukao, Y. and M. Obayashi (2013). Subducted slabs stagnant above, penetrating through, and trapped below the 660 km discontinuity. In: *Journal of Geophysical Research: Solid Earth* 118.11, pp. 5920–5938. ISSN: 2169-9356. DOI: 10.1002/2013JB010466.

Galetti, E. and A. Curtis (2012). Generalised receiver functions and seismic interferometry. In: *Tectonophysics* 532, pp. 1–26. DOI: 10.1016/j.tecto.2011.12.004.

Ohtani, E. (2020). The role of water in Earth's mantle. In: *National Science Review* 7.1, pp. 224–232. ISSN: 2095-5138. DOI: 10.1093/nsr/nwz071.

Peslier, A. H. et al. (2017). Water in the Earth's interior: distribution and origin. In: *Space Science Reviews* 212.1, pp. 743–810. DOI: 10.1007/s11214-017-0387-z.

Chapter 2

METASTABLE OLIVINE WEDGE BENEATH THE JAPAN SEA IMAGED BY SEISMIC INTERFEROMETRY

Shen, Zhichao and Z. Zhan (2020). Metastable olivine wedge beneath the Japan Sea imaged by seismic interferometry. In: *Geophysical Research Letters* 47.6, e2019GL085665. DOI: 10.1029/2019GL085665.

2.1 Abstract

The metastable olivine wedge (MOW) within subducted slabs has long been hypothesized to host deep-focus earthquakes (>300 km). Its presence would also rule out hydrous slabs being subducted into the mantle transition zone. However, the existence and dimensions of MOW remain debatable. Here, we apply inter-source interferometry, which converts deep earthquakes into virtual seismometers, to detect the seismic signature of MOW without influence from shallow heterogeneities. With data from the Hi-net, we confirm the existence of MOW beneath the Japan Sea and constrain its geometry to be ~30 km thick at 410-km depth and gradually thinning to a depth of 580 km at least. Our result supports transformational faulting of metastable olivine as the initiation mechanism of deep earthquakes, although large events (M7.0+) probably rupture beyond the wedge. Furthermore, the slab core must be dehydrated at shallower depth and only transports negligible amount of water into the transition zone.

2.2 Introduction

Global earthquakes mostly occur in the crust, but can extent to ~700-km depth within subducting plates. Crustal earthquakes are thought to be driven by brittle frictional failure (Scholz, 1998), while the nature of deep-focus earthquakes (depth >300 km) has been posed to geophysicists as a long-standing puzzle (Brace and Kohlstedt, 1980). Several mechanisms have been proposed for deep earthquakes, including the dehydration embrittlement (Meade and Jeanloz, 1991), thermal shear instability (Kanamori et al., 1998; Ogawa, 1987), and transformational faulting (Green II and Burnley, 1989). Among them, transformational faulting, which triggers the slip instability through a sudden phase change from metastable olivine to spinel, can naturally explain the depth dependent seismicity distribution that resurges

in the transition zone with an abruptly cessation below 660 km (Houston, 2015). Moreover, recent laboratory experiments have shown fracture nucleation and later intense acoustic emissions associated with the olivine-to-pinel phase transformation (Schubnel et al., 2013; Wang et al., 2017), thus making the transformational faulting hypothesis more appealing.

For transformational faulting to happen, it is hypothesized that the low-pressure polymorphs of olivine inside cold slabs could metastably extend into the mantle transition zone (MTZ), forming a tongue-shaped "metastable olivine wedge" (MOW). Furthermore, the positively buoyant MOW, if present, may slow down the subducting slab in the MTZ (Bina et al., 2001), or even resist the slab from penetrating into the lower mantle (Tetzlaff and Schmeling, 2000). The dimension of MOW is generally thought to correlate with the slab thermal parameter (Kirby et al., 1996), but the water content of subducted slab and the latent heat due to the phase changes also play crucial roles (Du Frane et al., 2013; Kubo et al., 1998; Mosenfelder et al., 2001). Laboratory experiments demonstrated that incorporation of a small amount of H_2O leads to a remarkable boost in the olivine to ringwoodite transformation rate via hydrolytic weakening process (Du Frane et al., 2013). The latent heat feedback together with an additional intracrystalline transformation mechanism significantly reduces the maximum depth that MOW can reach as suggested from an updated thermo-kinetic model (Mosenfelder et al., 2001). Therefore, the existence and exact geometry of MOW would provide essential constraints on the thermal-petrological properties of subducting slabs.

However, seismic imaging of the low-velocity MOW structure has been particularly challenging. For instance, body wave travel time analysis ubiquitously suffers from the wavefront healing effect. A thermal slab without MOW could satisfactorily predict high-resolution seismic arrival times, but the inclusion of MOW merely offers a subtle improvement on the data fitting (Koper et al., 1998). It has also been illustrated that the metastable olivine can be unveiled from waveform distortions of some seismic phases that travel through it (Koper and Wiens, 2000; Vidale et al., 1991). Nonetheless, deterministically examining the seismogram involves great effort because lithospheric heterogeneities contribute great complexities on the seismogram and smear the illumination of deep slab. Given the difficulty in resolving MOW, its thicknesses reported from preceding studies differ by more than a factor of 2 in Japan subduction zone (Furumura et al., 2016; Iidaka and Furukawa, 1994; Iidaka and Suetsugu, 1992; Jiang and Zhao, 2011; Jiang et al., 2008; Jiang et al., 2015; Kawakatsu and Yoshioka, 2011; Wiens et al., 1993; Kaneshima et al., 2007) (Table

2.1), leaving the metastable persistence of olivine and its detail geometry hitherto ambiguous.

Method	Study Area	Thickness at 410-km	Depth Extend	Reference
Traveltime Inversion	SW. Japan	N/A	~500 km	Iidaka and Suetsugu, 1992
Traveltime Inversion	Japan Sea	50 km	560 km	Jiang et al., 2008
Traveltime Inversion	Japan Sea	50 km	570 km	Jiang and Zhao, 2011
Traveltime Inversion	N. Japan Sea	N/A	580 km	Jiang et al., 2015
Receiver Function	SW. Japan	~25 km	~450 km	Kawakatsu and Yoshioka, 2011
Coda Wave	N. Japan Sea	50 km	600 km	Furumura et al., 2016
Double Seismic Zone	SW. Japan	10~20 km	<500 km	Iidaka and Furukawa, 1994
Double Seismic Zone	Fiji-Tonga	20~40 km	460 km	Wiens et al., 1993
Teleseismic waveform	Mariana	N/A	630 km	Kaneshima et al., 2007

Table 2.1: Comparison of metastable olivine wedge geometry proposed from previous seismic studies. The last two row are the proposed MOW geometries at other subduction zone.

2.3 Inter-source Interferometry

To untangle the potentially subtle seismic signature of metastable olivine from complex shallow Earth heterogeneities, we apply inter-source interferometry (Curtis et al., 2009; Tonegawa and Nishida, 2010) to deep earthquake pairs in the Japan subduction zone (Figure 2.1a). For conventional inter-receiver interferometry, cross correlations of diffusive earthquake coda or ambient noise field reconstruct Green's functions between receiver pairs (Campillo and Paul, 2003). Equivalently, due to reciprocity, by cross-correlating coda waves from an earthquake pair, the inter-source interferometry synthesizes the transient strain triggered by passing seismic waves from one source to the other. This is as if we convert one of the deep earthquakes to a virtual seismometer deployed below the complex shallow layers and record the other event. To avoid violating the impulsive-source condition in reciprocity, we select five deep-focus earthquakes of small magnitudes ($4.0 \leq Mw \leq 5.2$) with simple source process (<10% non-double-couple component). Among them, three earthquakes (S1, S2, and S3) are refined at ~360-km depth whereas the other two (D1 and D2) are at depths of ~580 km (Figures 2.2 and 2.3; see section 2.6 for relocation details), corresponding to the shallow and deep ends of hypothesized MOW, respectively. Although receivers in the inter-source interferometry should have a complete azimuthal coverage, the stationary phase approximation greatly loosens the receiver geometry restriction (Snieder, 2004; see section 2.6 for inter-source interferometry theory). For our targeted slab beneath the Japan Sea, Hi-net stations situate around the stationary phase region of the deep earthquake pairs (the region along the extension of earthquake pairs; Figure 2.1b), hereby providing an

ideal source-receiver configuration to isolate the deep slab structures from other complexities.

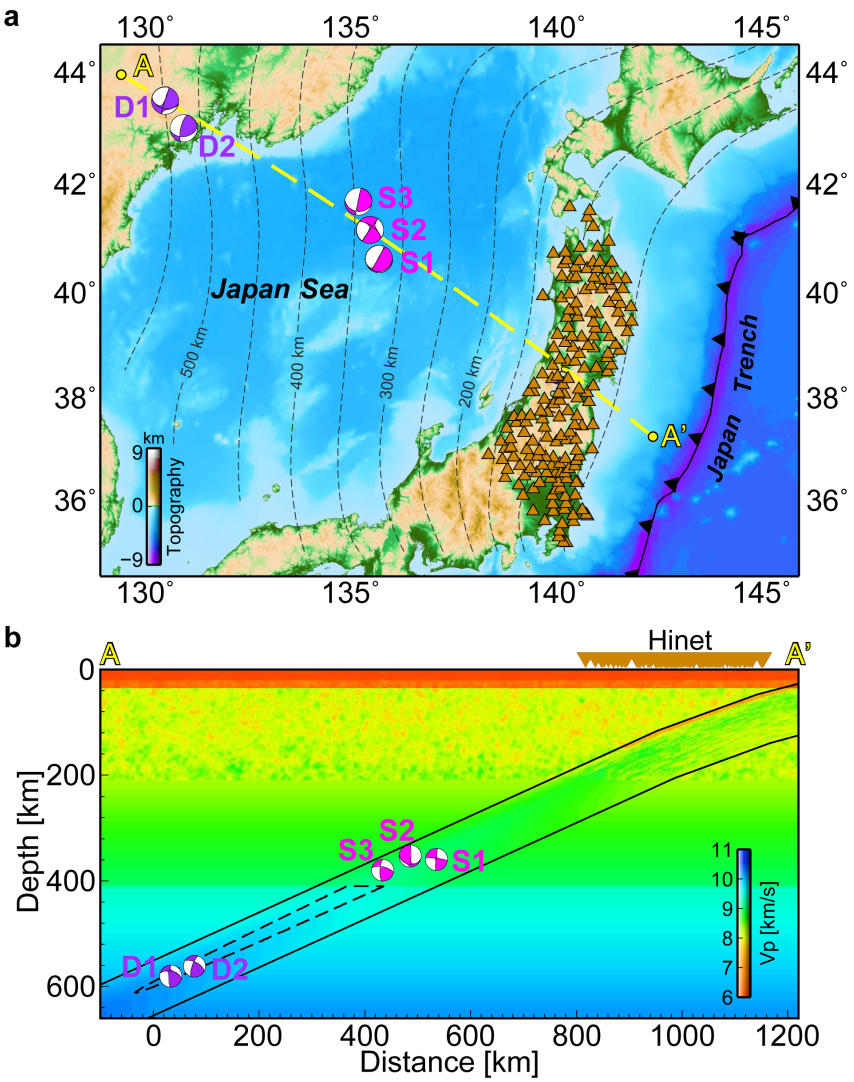

Figure 2.1: Map view of our targeted area and depth profile of Japan subduction zone. (a). Map of this study area. Black dashed lines are the slab depth contours from Slab2.0 model (Hayes et al., 2018). Orange triangles are Hi-net stations used in our interferometry. The purple and magenta beachballs are from National Research Institute for Earth Science and Disaster Resilience (NIED) and represent the earthquake depths of ~580 km (D1, D2) and ~360 km (S1, S2, S3), respectively. (b). P-wave velocity profile derived from thermal modeling along AA'. The black solid line and black dashed line represent the geometry of subducting Pacific slab and hypothesized MOW, respectively. Above 200 km depth, small scale heterogeneities are included. D1/D2 and S1/S2/S3 correspond to the deep (~580 km) and shallow (~360 km) end of the MOW, respectively.

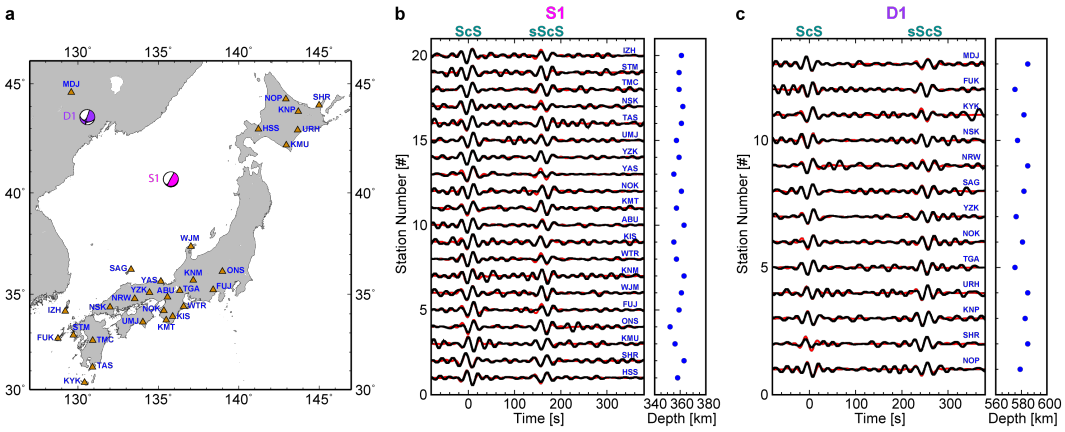

Figure 2.2: Focal depth determination of events S1 and D1 using ScS and sScS. (a). Map view of deep earthquakes D1 and S1 and broadband stations used for determining the focal depth. (b). left panel shows the ScS and sScS tangential waveform comparison between observations (black) and synthetics (red) for earthquake S1. Right panel indicates the optimal focal depth of individual station by searching for the highest cross-correlation coefficient. The averaged optimal focal depth is 359 km for S1. (c). Similar to (b), but for earthquake D1, the averaged focal depth is 580 km.

We first validate the inter-source interferometry method for two synthetic scenarios with and without MOW. The velocity and density profiles of slab and MOW are constructed based on a thermal model tuned for the Japan subduction zone (see section 2.6 for thermal modeling details). Small-scale heterogeneities are implemented at shallow depths to produce realistic coda waves (Figure 2.1b; Furumura and Kennett, 2005). Given the velocity and density profiles, we simulated the elastic wavefield with a GPU-based 2-D finite difference code in Cartesian coordinates, which is eighth order in space and second order in time (Li et al., 2014). With a minimum shear velocity of 2.8 km/s, a grid spacing of 75 m, and time step of 0.001 s, our computed synthetic waveforms are accurate up to 6 Hz with sampling of at least six grids per wavelength. Here, we simplified the problem into a 2-D slab geometry since we mainly focus on the updip direction. Moreover, 2-D and 3-D numerical simulations of the high-frequency trapping/guiding waves have been shown no significant differences (Kennett and Furumura, 2008; Takemura et al., 2015). After computing synthetic seismograms on the surface from deep earthquakes D1 and S1, we filter and cut the vertical-component coda waves from 5 to 45 s after the P wave first arrivals for interferometry. The 40-s-long window is further cut into 10-s-long overlapping segments offset by 2 s. The cross correlations of all the segments are then normalized by the maximum and averaged to account for the coda energy

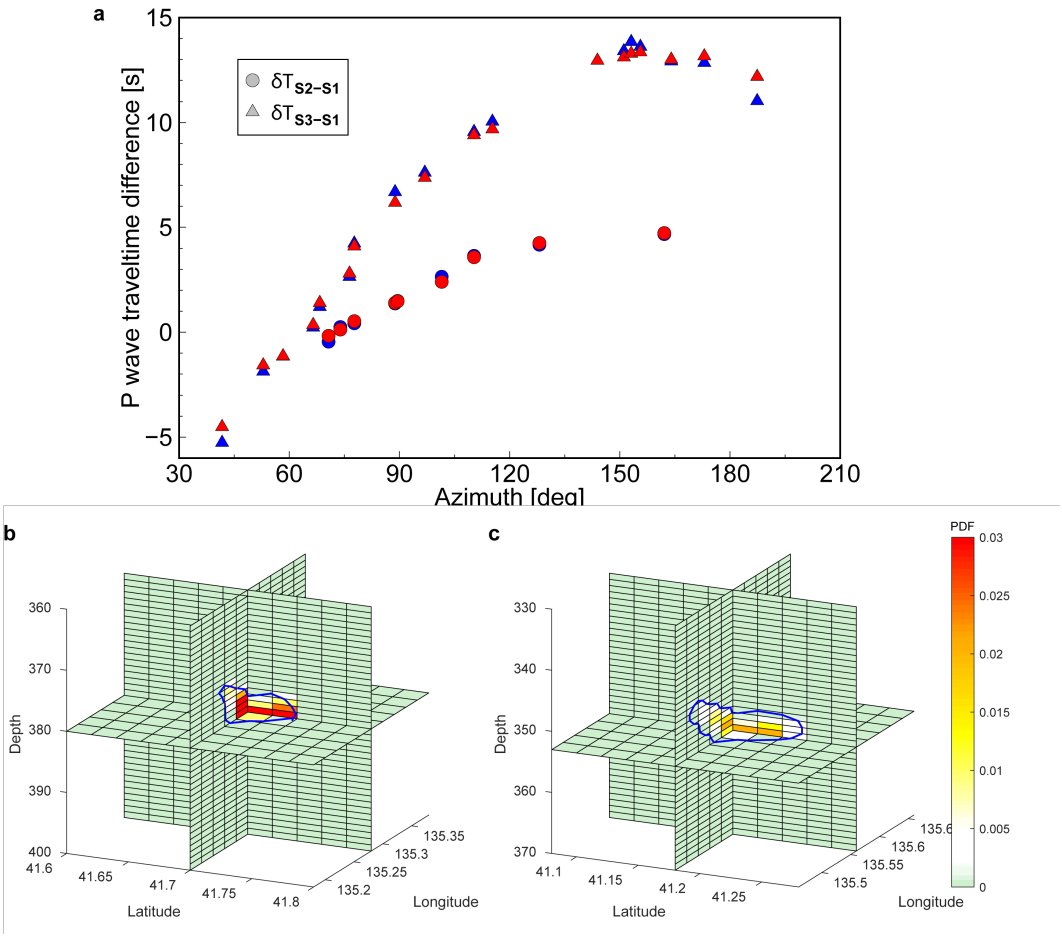

Figure 2.3: Traveltime based relocation results and uncertainty analysis. (a). P wave traveltime differences as a function of azimuth for different events. The circle and triangle symbols represent P wave traveltime differences of S3-S1 and S2-S1, respectively. Observed and predicted P wave traveltime differences are indicated in blue and red, respectively. (b). Relative relocation probability distribution for deep earthquake S2. The blue line denotes 95% probability contour. (c). Similar to (b), but for deep earthquake S3.

decay with time. For the D1-S1 earthquake pair in both scenarios, the 0.2-2 Hz cross-correlation record section presents coherent waveforms with constant arrival time across the profile of Hi-net (Figure 2.4). This indicates that our simulated coda wavefields are diffuse due to shallow heterogeneities and the inter-source Green's function could be extracted by coda interferometry at a single station (Snieder, 2004). To enhance the coherent signal, we stack the cross correlations over all the stations. In both scenarios with and without MOW, the resulting interferometric waveforms match the directly simulated P wave strain seismograms from source D1 to virtual receiver S1 and, meanwhile, capture the polarity flip (Figure 2.4b vs. 2.4c)

caused by the reverberation of P wave within the MOW (Figure 2.5). For the case with MOW, although the P refraction wave arrives earlier than the reverberation, its energy is too weak to be captured (Figure 2.5f). Since absolute arrival times have strong trade-offs with earthquake locations, herein, we focus solely on interpreting the waveform shape.

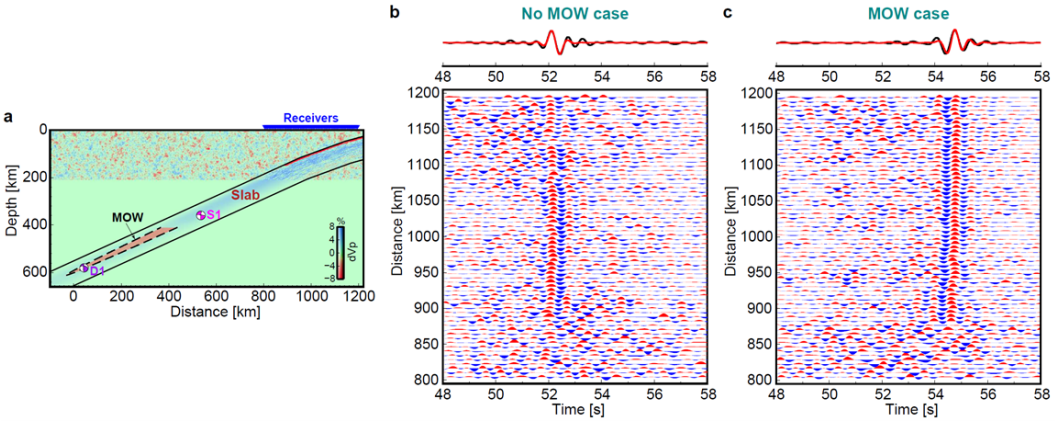

Figure 2.4: 0.2~2 Hz inter-source interferometry benchmark results. (a). P wave velocity perturbation profile derived from the thermal modeling (8 cm/yr, 30 Ma; T_{mow} = 664°C). Heterogeneities are imposed above 200 km. The slab and MOW geometries are delineated by black solid line and black dashed line, respectively. The MOW model is the same as that in Figure 2.14a with a thickness of 29 km at 410 km depth. A 5% velocity reduction is placed within MOW. Deep earthquakes D1 and S1 are used here. Waveforms of a linear array (blue inverted triangles) on the surface are calculated. (b). Inter-source interferometry benchmark result for a case of thermal slab without MOW (NO MOW case). The lower panel shows the cross-correlation record section of the linear array as a function of distance to D1. The upper panel is the waveform comparison between stacked (black) and predicted (red) strain response from D1 to S1. (c). Similar to (b), but for the case of slab with MOW. Note that the waveform polarity flipped after introducing the MOW.

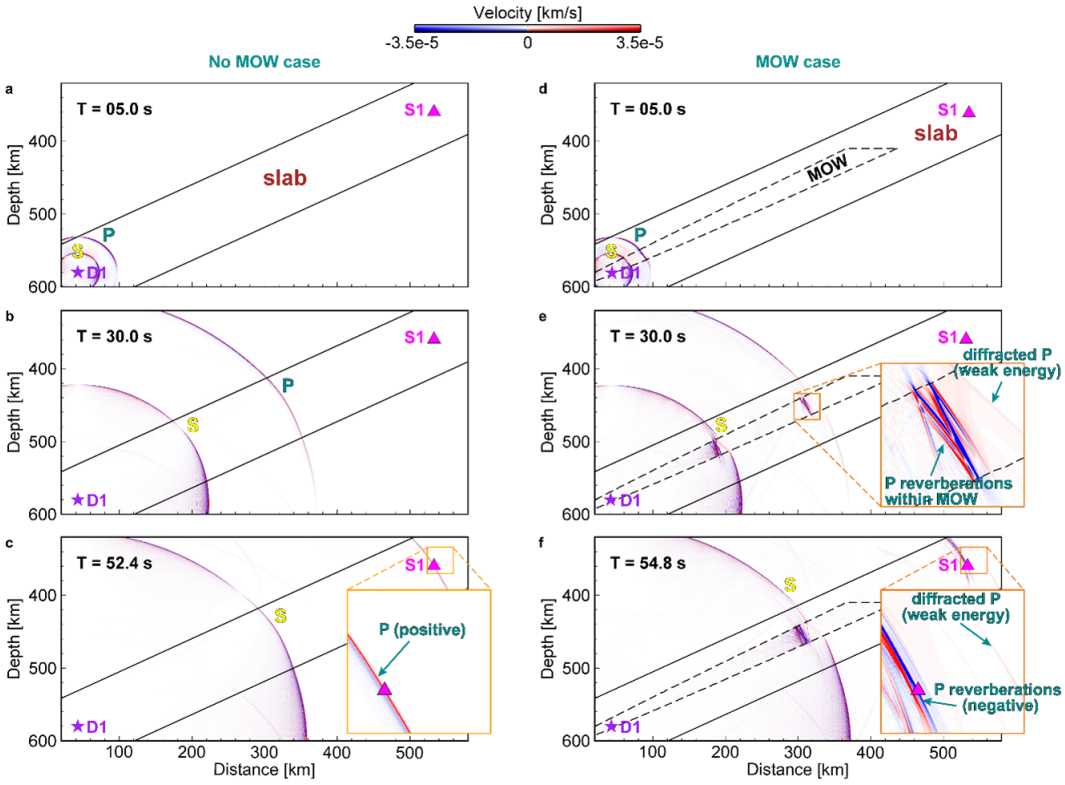

Figure 2.5: Snapshots of wavefield propagating from deep source D1 (purple star) to virtual receiver S1 (magenta triangle) for No MOW and MOW cases. The snapshots of No MOW case are shown for (a). 5.0 s, (b). 30.0 s and (c). 52.4 s after the origin time of D1. (d)~(f). show the snapshots of MOW case at 5.0 s, 30.0 s and 54.8 s after the origin time of D1, respectively. The slab and MOW geometries are delineated by black solid line and black dashed line, respectively. The MOW model (8 cm/yr, 30 Ma; T_{mow} = 664°C) is the same as that in Figure 2.14a with a thickness of 29 km at 410 km depth. Both P and S wavefields are shown in the snapshots. Positive and negative wavefield are indicated in red and blue, respectively.

2.4 Results

Having shown the feasibility to retrieve the P wave strain Green's functions between two deep earthquakes, we apply the inter-source interferometry method to real data on the Hi-net stations (Figure 2.1). As an example, the cross-correlation record section for the D1-S1 earthquake pair at 0.2-2 Hz exhibits coherent signals arriving at a constant time in a wide azimuth range (Figure 2.6a), implying a diffuse coda wavefield. After stacking all the individual cross correlations, the resulting waveform presents a negative trough preceding a positive peak, similar to that of aforementioned synthetic case with a MOW (Figure 2.6c). Furthermore, the interferometric results of other earthquake pairs are in good agreement with that of D1-S1 pair (Figure 2.7), favoring a MOW structure instead of a simple slab

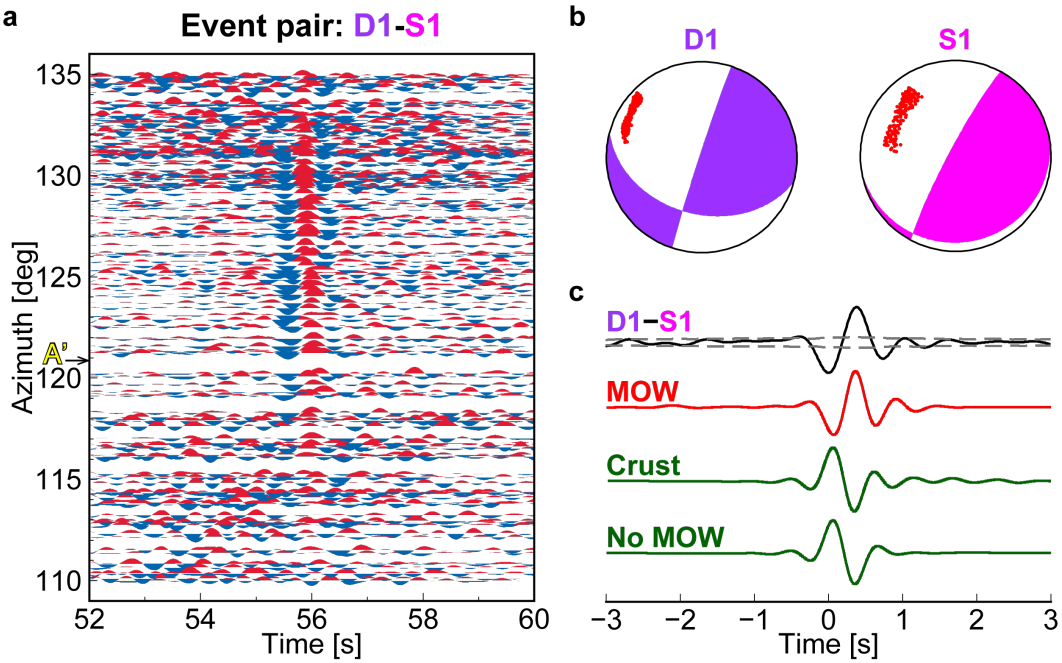

Figure 2.6: Inter-source interferometry results at 0.2~2 Hz suggest the existence of metastable olivine beneath the Japan Sea. (a). The record section of coda wave cross-correlations as a function of azimuth for the D1-S1 earthquake pair. The azimuth (120.7°) of AA' profile in Figure 2.1 is shown as A' with a black arrow. Blue and red color correspond to the negative and positive phases, respectively. Coherent signals with negative polarities arrive at a constant time across Hi-net stations. (b). First motion analysis for deep earthquake D1 and S1. At Hi-net stations (red dots), both events share the same P-wave polarities. (c). Waveform comparison of observations and synthetics. The top black trace is the stacked cross-correlation waveform from all the traces shown in (a) for D1-S1 deep earthquake pair. The gray dashed lines denote the noise level. The red and dark green lines are the synthetic strain waveforms for cases of a thermal slab with MOW (MOW), a thermal slab with hydrous oceanic crust (Crust) and a thermal slab only (No MOW). All the traces are aligned by their peak phases. Only the MOW model predicts the waveform shape observed in D1-S1 pair.

model without MOW (Figures 2.8a and 2.8b). Note that there are some waveform differences among our observed waveforms (e.g., weakening of positive phase after the negative phase: D1-S2 vs. D2-S2). In fact, those differences can be explained by the location difference between D1 and D2, which will be shown later. Beside the MOW cause, we also scrutinize other alternatives that could result in the negative pulse, such as opposite focal mechanisms and a low-velocity hydrous oceanic crust on top of the slab. First motion analysis shows that the Hi-net stations used for interferometry share same P wave polarities for all the selected deep earthquakes (Figures 2.6b and 2.9), so radiation patterns alone cannot explain the negative

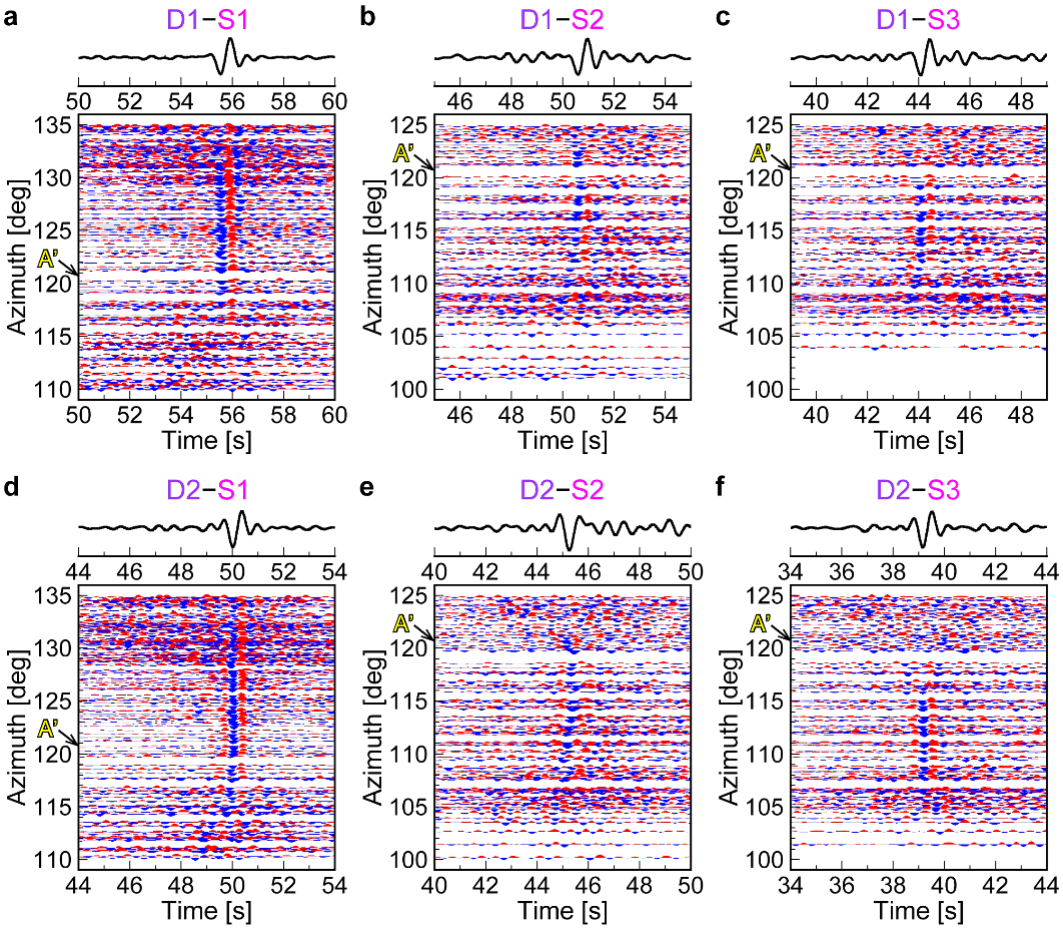

Figure 2.7: Inter-source interferometry results of all the six earthquake pairs (a~f) at the frequency band of 0.2~2 Hz. In each subplot, the lower panel is the record section of cross-correlations at individual Hi-net stations. The top panel represents the stacked cross-correlation waveform from the individual waveforms shown in the lower panel. The azimuth (120.7°) of AA' profile in Figure 2.1 is shown as A' with a black arrow.

polarities of the correlations. An 8-km-thick oceanic crust with a velocity reduction of 8% extending to 660 km fails to reproduce our observations as well (Figures 2.6c and 2.10). With these alternative possibilities ruled out, we suggest the existence of metastable olivine beneath the Japan Sea as the preferred interpretation.

To better quantify the MOW dimension and depth extent, which are both important for understanding deep earthquake physics and slab hydrous state, we need to appeal to higher frequency interferometric waveforms. For example, we show that the 0.2-2 Hz cross-correlation waveforms are insensitive to the location of S1/S2/S3 relative to the MOW (Figure 2.11), which in turn provide little information on the thickness of MOW at the shallow end. On the other hand, at 0.2-5 Hz, synthetic strains are

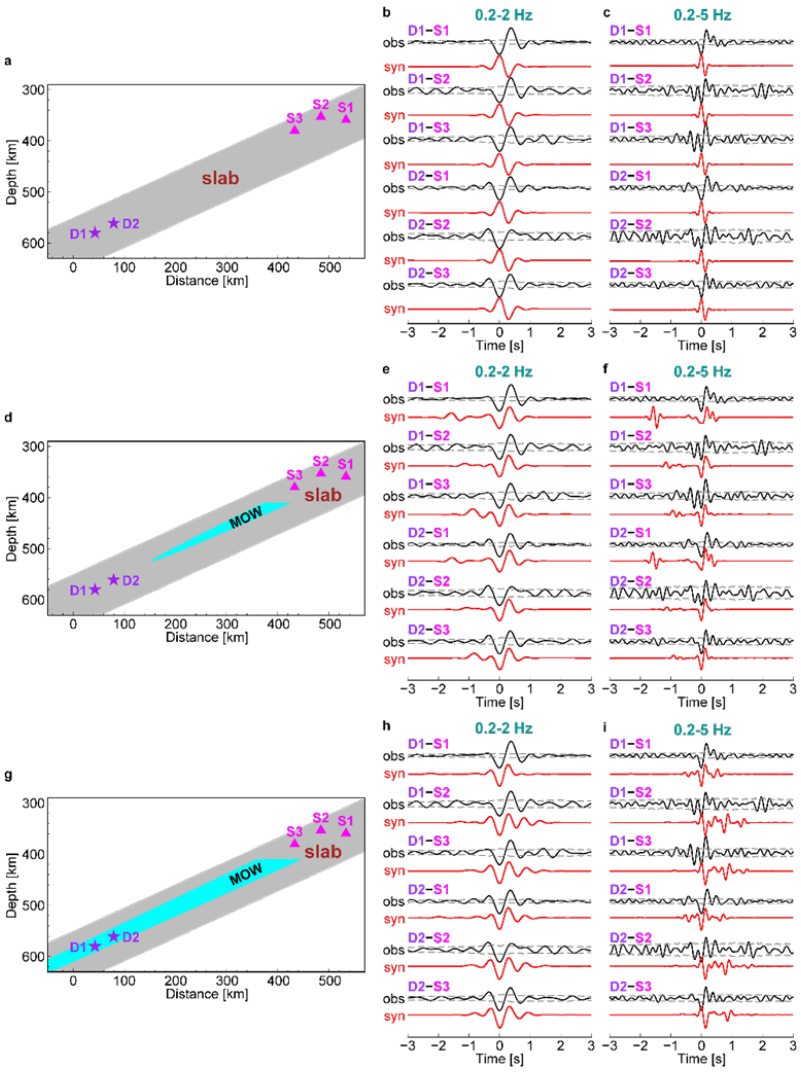

Figure 2.8: MOW thickness effects on the inter-source interferometric waveform fitting for 0.2~2 Hz and 0.2~5 Hz. (a). A simple slab profile with deep earthquakes D1/D2 and three virtual receivers (S1-S3). (b). 0.2~2 Hz waveform comparison of inter-source interferometric observations (black lines) and synthetics from a simple thermal slab model as shown in (a) for all deep earthquake pairs. The gray dashed line denotes the noise level. (c). Similar to (b), but for 0.2~5 Hz waveforms. (d). Slab profile with a thin MOW model (8 cm/yr, 30 Ma; T_{mow} = 620°C). The MOW at 410 km is 22 km thick. (e). and (f). are the waveform comparison of observations and corresponding synthetics from thin MOW model at 0.2~2 Hz and 0.2~5 Hz, respectively. (g). Slab profile with a thick MOW model (8 cm/yr, 30 Ma; T_{mow} = 720°C). The thickness of MOW at 410 km is ~40 km. (h). and (j). are the waveform comparison of observations and corresponding synthetics from thick MOW model at 0.2~2 Hz and 0.2~5 Hz, respectively.

significantly distorted across a short distance range (Figure 2.11). The rapid high-frequency waveform variations are due to the receiver locations with respect to the

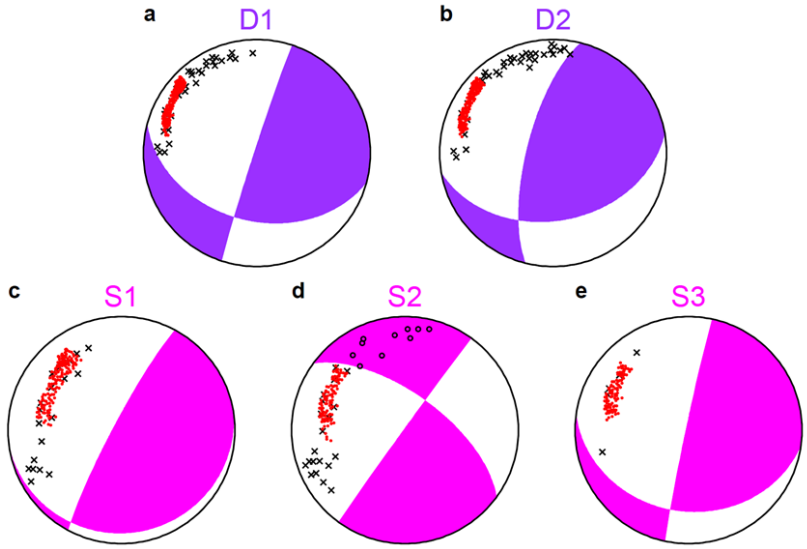

Figure 2.9: First motion analysis for all deep earthquakes (a~e) used in this study. The fault planes are from National Research Institute for Earth Science and Disaster Resilience (NIED). Red dots represent Hi-net stations used in the inter-source interferometry. Black crosses and circles indicate negative and positive polarities identified on F-net seismograms, respectively.

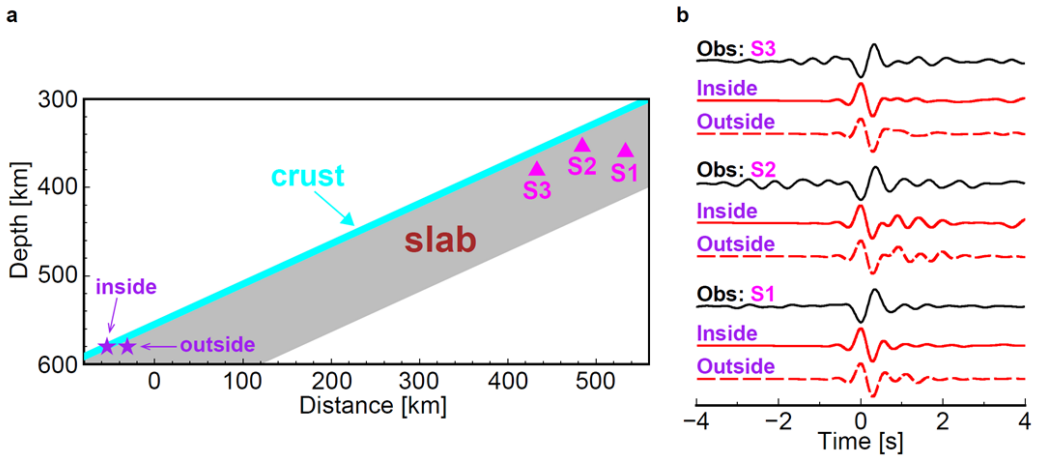

Figure 2.10: Oceanic crust fails to reproduce observed inter-source interferometry results. (a). Slab profile and source-receiver configuration. The grey and cyan area represent the slab and crust, respectively. The crust is 8 km thick with 8% reduction in velocity and density. Synthetic waveforms at three virtual receivers (magenta triangles) are calculated for cases of deep earthquakes (purple stars) inside and outside the crust. (b). 0.2~2 Hz waveform comparison between observations (black) and synthetics (red). The red solid lines and red dashed lines indicate synthetics for cases of deep earthquake inside and outside the crust, respectively.

P multiples (Figures 2.5e, 2.5f, and 2.11d–f). Hence, with well-constrained relative locations among the virtual sensors S1, S2, and S3, we can use higher frequency

(up to 5 Hz) waveform details at different locations to determine the geometry of metastable olivine. Indeed, for synthetic tests with a set of earthquake pairs, the inter-source interferometry is shown to be capable of extracting 5-Hz transient strains and capturing the waveform variations at different virtual sensors (Figure 2.12). Furthermore, 15° variation in focal mechanisms (Kubo et al., 2002) barely changes the stacked strain waveform shapes in our synthetic tests (Figure 2.12d).

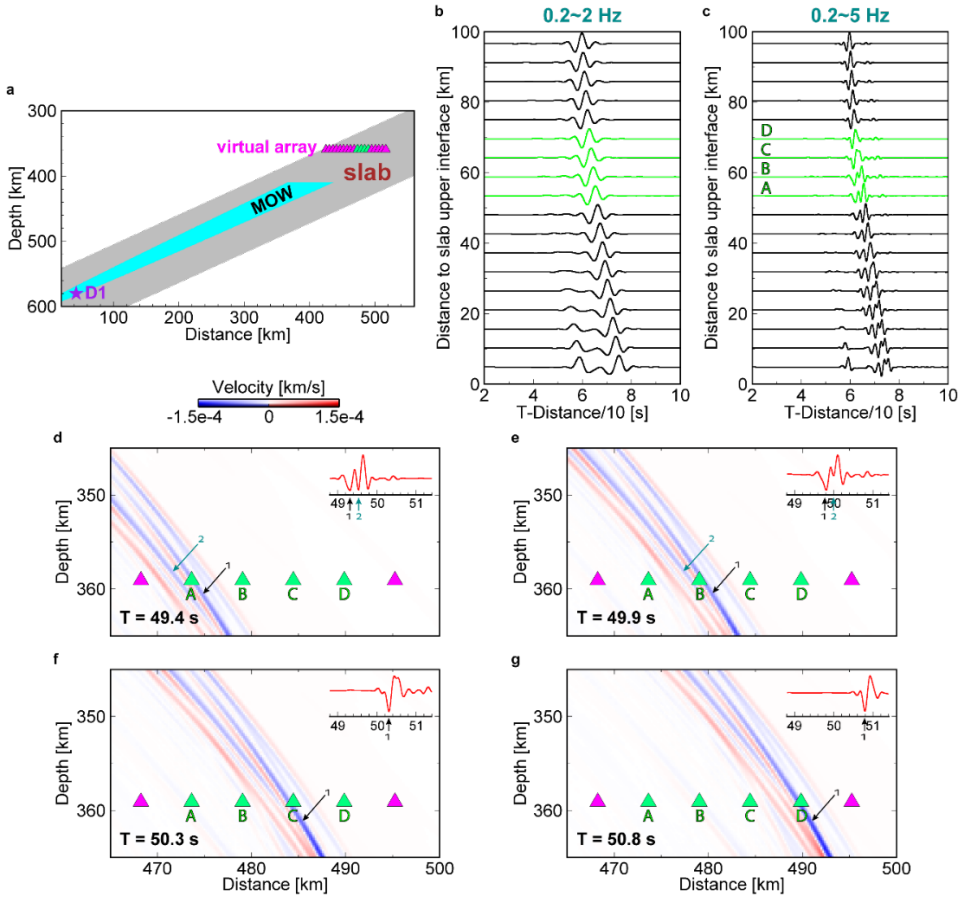

Figure 2.11: Frequency dependence of the inter-source interferometry. (a). Slab profile and source-receiver configuration. The gray and cyan region represent the slab and MOW, respectively. The MOW model (8 cm/yr, 30 Ma; T_{mow} = 664°C) is the same as that in Figure 2.14a with a thickness of 29 km at 410-km depth. The P-wave velocity within MOW decreases 5%. A virtual linear array (magenta triangles) is placed from the slab upper interface toward the slab center at a depth of 359 km. Deep earthquake D1 (purple star) is within MOW with a depth of 580 km. (b). Record section of 0.2~2 Hz waveforms for the virtual array. (c). Similar to (b), but for 0.2~5 Hz waveforms. Note the rapid change of 0.2~5 Hz waveforms (shown in green) at the distance range of 50~70 km (from receiver A to D), while 0.2~2 Hz waveforms are kept the same. (d).~(e). are the snapshots of simulated wavefield from deep earthquake D1 to receiver A~D, respectively. The spitting waveforms recorded at stations A and B are marked by arrows.

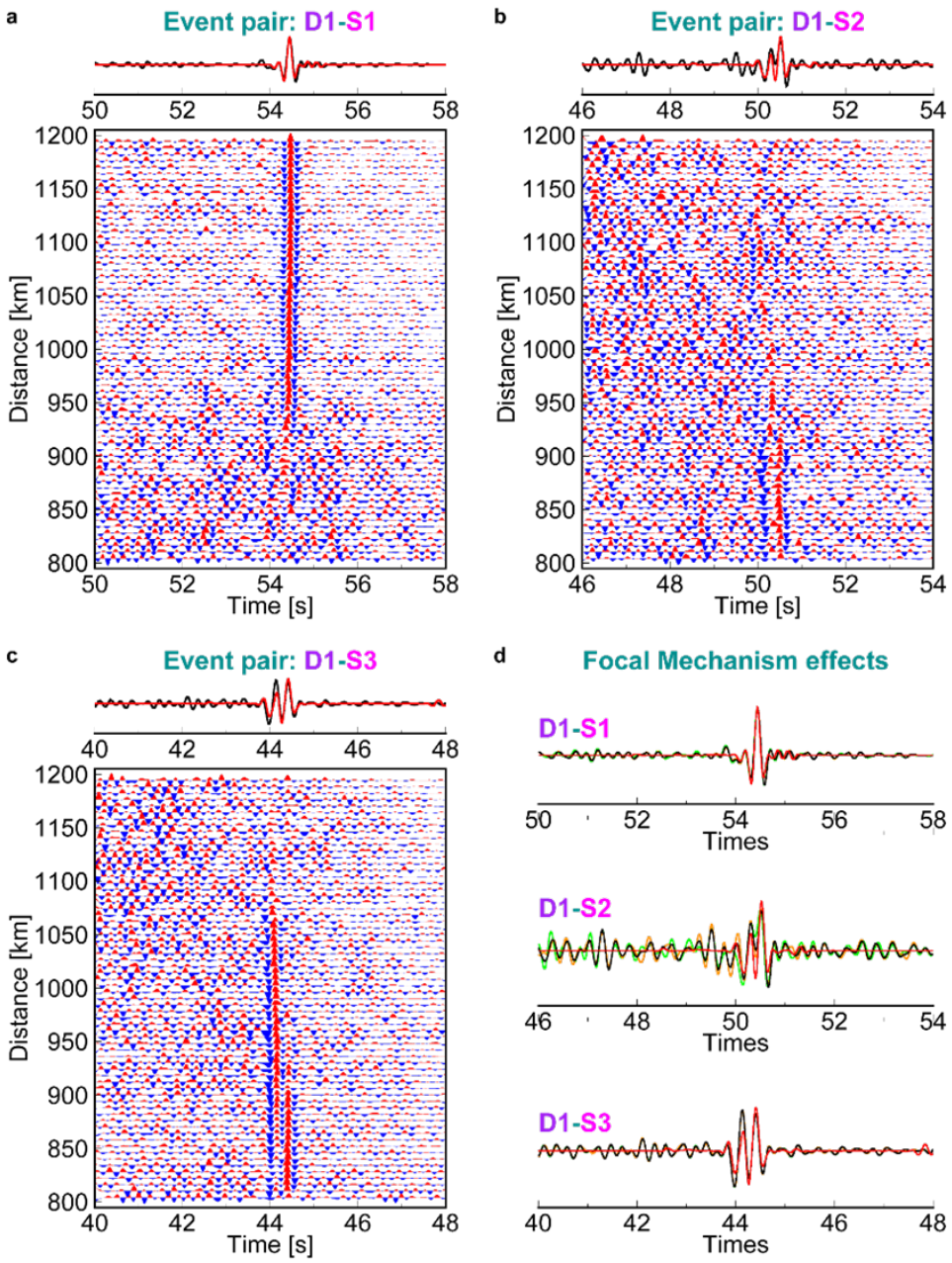

Figure 2.12: 0.2~5 Hz inter-source interferometry benchmark results for event pairs: (a). D1-S1, (b). D1-S2 and (c). D1-S3. The lower panel shows the coda wave cross-correlation record section of a linear array on the surface (Figure 2.4a). The upper panel is the waveform comparison between stacked (black) and synthetic (red) strain response. (d). Focal mechanism sensitivity tests for event pairs D1-S1/S2/S3. The black and red waveforms are the stacked and synthetic strain waveforms for the NIED focal mechanism solutions of S1/S2/S3. The orange and green waveforms represent the stacked cross-correlations for perturbing (±)15° in strike, dip and rake of NIED solutions, respectively. Note that 15° variation in S1, S2 and S3 focal mechanisms barely changes the obtained strain waveform shapes.

Subsequently with the real data from Hi-net, we retrieve the 0.2-5 Hz strain responses for all six earthquake pairs from D1/D2 to S1/S2/S3 following the same interferometry procedures (Figure 2.13). Taking D1 as an example, virtual sensor S1 records a simple trace with negative polarity, but the other two (S2 and S3) present splitting waveforms that consist of two phases (Figure 2.14c).

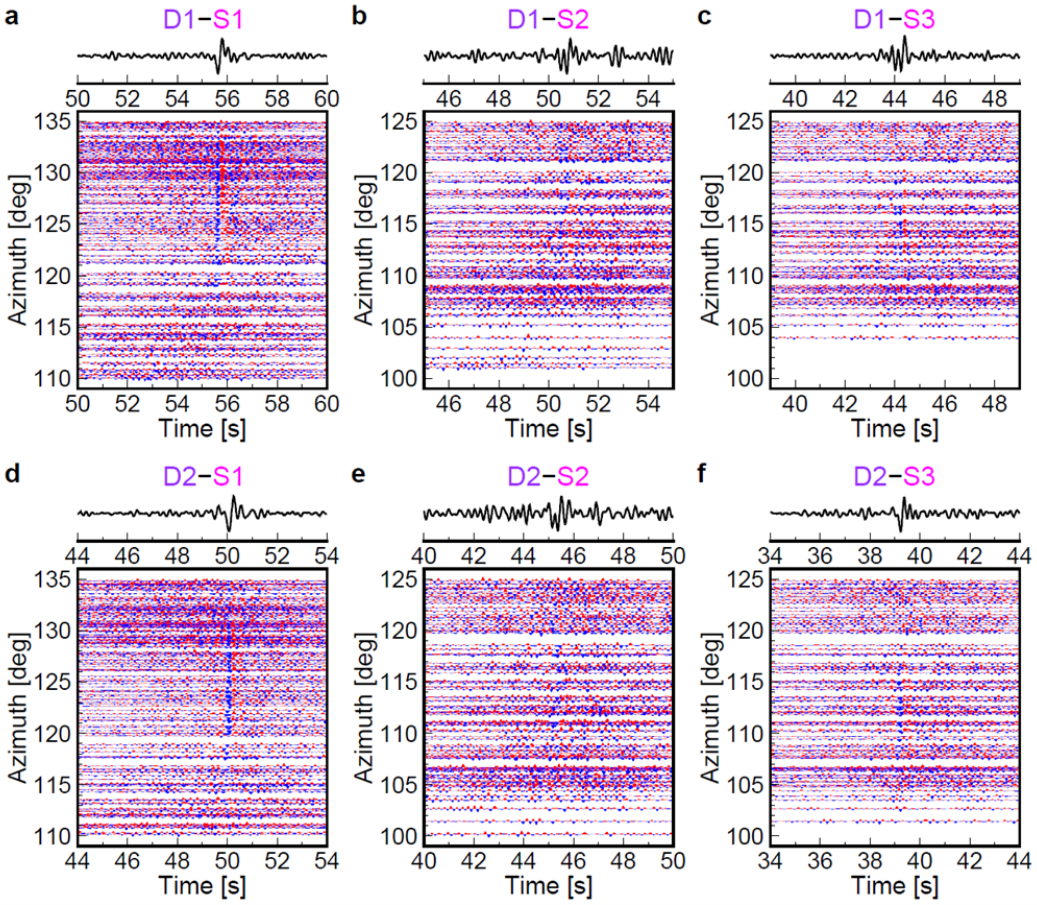

Figure 2.13: 0.2~5 Hz inter-source interferometry results. Similar to Figure 2.7, but for the frequency band of 0.2~5 Hz.

To evaluate the robustness of observed waveform complexity, we estimated their noise level by computing the 95% confidence intervals for stacked cross correlations using a bootstrapping technique (Figure 2.15). All the coherent signals among D1-S1/S2/S3 evidently stand above the noise level; thus, the traces characterized by splitting phases are unlikely caused by noise (Figure 2.15). Also, S1 and S3 have similar beachballs, but present apparent waveform variations, ruling out the focal mechanism cause. Instead, the distinct interferometric waveforms appear to correlate with the spatial distribution of virtual sensors: S2 and S3 with splitting

phases are close to the slab upper interface, whereas S1 with a single phase sits near the slab core (Figure 2.14a). In addition, similar interferometric results from the other deep earthquake D2, though with higher noise levels (Figure 2.14c).

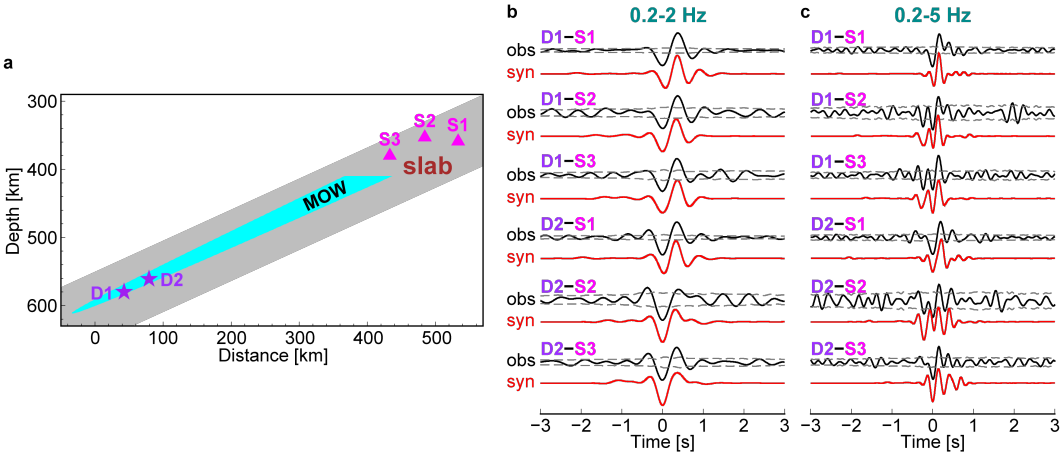

Figure 2.14: Proposed MOW dimension can reproduce our inter-source interferometry observations. (a). Slab profile with deep earthquakes D1/D2 and three virtual receivers (S1–S3). The gray and cyan region denote the slab and our proposed MOW, respectively. The P wave velocity within MOW decreases 5%. Both D1 and D2 need to be within MOW to explain the interferometric waveforms. (b). The 0.2-2 Hz waveform comparison of inter-source interferometric observations (black lines) and synthetics (red lines) for all deep earthquake pairs. The gray dashed lines denote the noise level. (c). Similar to (b), but for higher frequency up to ~5 Hz. All six waveforms are well fitted by our suggested MOW model.

To account for these high-frequency waveform variations, we grid-searched a variety of MOW geometries through physics-based modeling. Assuming that temperature is the first-order control on the olivine phase transformation, the MOW would thus be defined as the region colder than a kinetic cutoff temperature (T_{mow}) in our initial thermal slab. In searching for the optimal MOW geometry to fit our interferometric observations, we directly computed the synthetic waveforms at virtual seismometer S1/S2/S3 from deep earthquake D1/D2. When comparing the synthetics with observations, we tested different kinetic kick-off temperatures as well as the deep earthquake locations relative to MOW allowing a maximum arrival time difference of 1.5 s. We found that both 0.2-2 and 0.2-5 Hz interferometric waveforms can be adequately fitted when T_{mow} is defined as 664 °C with D1 and D2 situating close to, but at different distances from, the lower boundary of metastable olivine (Figure 2.14). The resolved P wave velocity within MOW is 4-5% lower than the surrounding slab velocity (2-3% lower than that of ambient mantle; Figure 2.16),

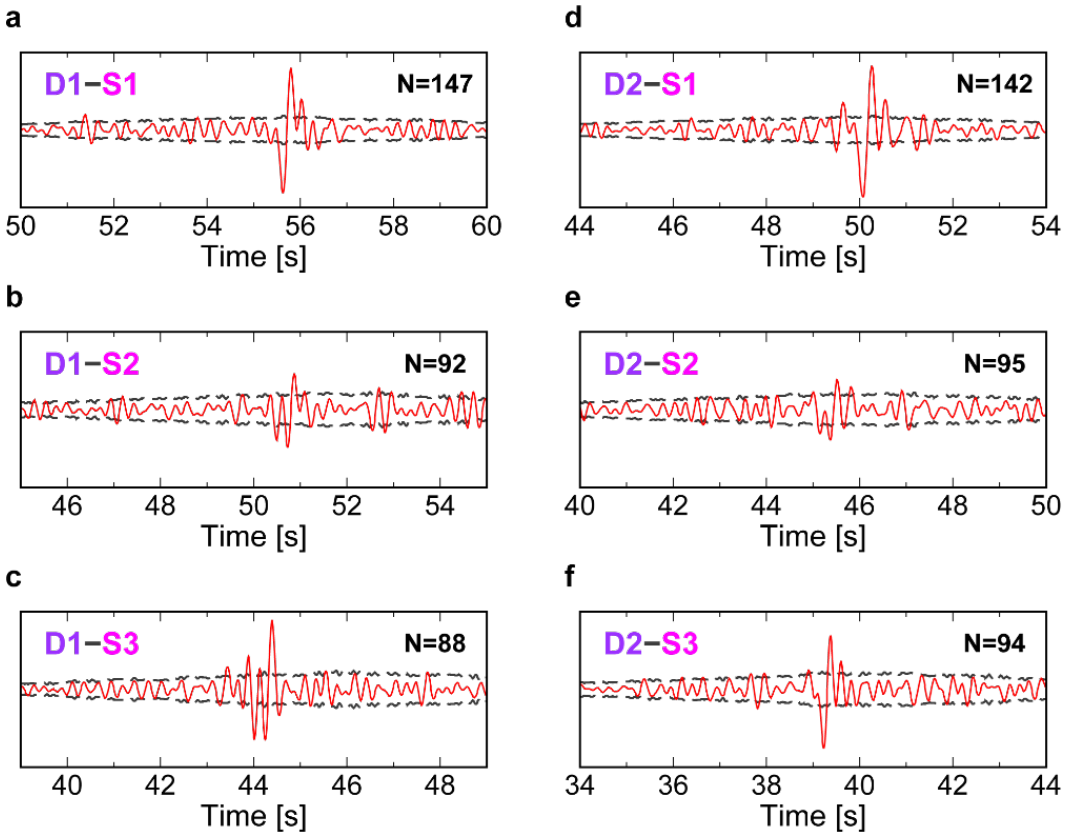

Figure 2.15: Bootstrapping tests of the 0.2~5 Hz inter-source interferometry results from all six deep earthquakes pairs (a~f). The red waveforms are the stacked cross-correlations and gray dashed lines indicate the noise level. The number of stacked cross-correlations are noted in the top right corner. Note that the splitting waveforms can not be alternatively interchanged with a single phase within two standard deviations.

which is consistent with previous studies (Furumura et al., 2016; Jiang and Zhao, 2011). Furthermore, our MOW model also provides a good fit to interferometric observations at the three virtual receivers from the other deep earthquake D2 (Figure 2.14). For instance, as discussed earlier, the observed D2-S2/S3 2-Hz waveform presents a much weaker positive phase after the negative one than that of D1-S2/S3 (Figure 2.14b). These waveform differences are well captured by our MOW model, while a simple slab model cannot produce such waveform variations (Figures 2.8a-c). Despite that the 2-Hz and 5-Hz interferometric waveform details are not fully explained due to lateral variations in slab structures, the observed waveform features (polarities, single, or splitting phases) are generally retained in synthetic seismograms. Given the same thermal model, neither a thinner MOW (T_{mow} = 620°C) and a thicker MOW (T_{mow} = 720°C) can reproduce most of the 5-Hz

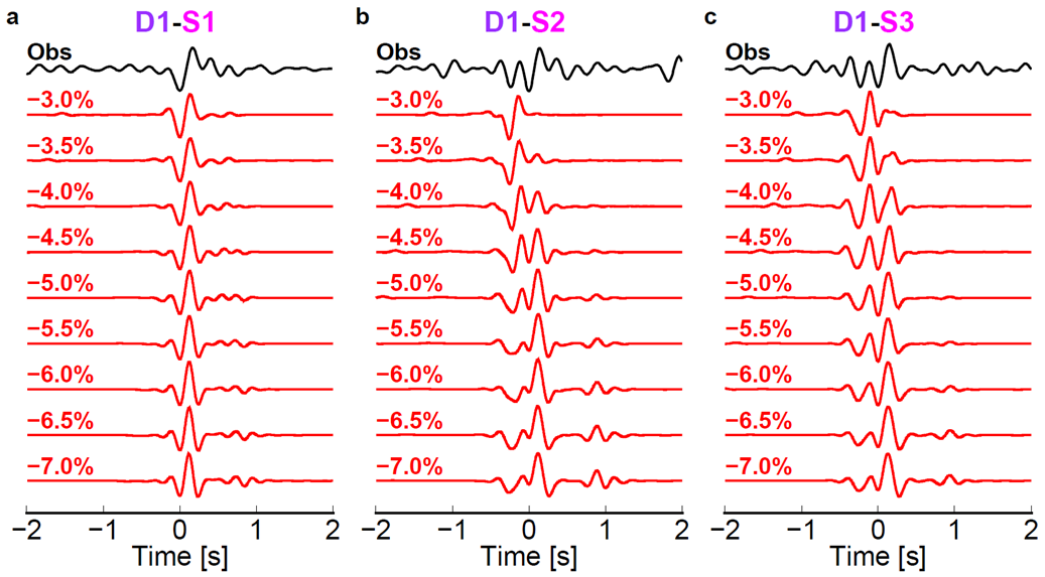

Figure 2.16: 5 Hz waveform comparison of observations (black) and synthetics (red) with different P-wave velocity anomalies within MOW for (a). D1-S1 pair, (b). D1-S2 pair and (c). D1-S3 pair. The velocity perturbation is indicated in the left of each trace. Note that synthetics with a P-wave perturbation of $-4\% \sim -5\%$ generally fit observations.

observations (Figures 2.8d–i). Moreover, we computed the waveform similarity among observations and synthetics for a variety of T_{mow} models. The allowed MOW dimension is quantified to a narrow range of T_{mow} (Figure 2.17), corresponding to 28-30 km thick at 410 km and gradually thinning to a depth of 600-620 km. Here, we emphasize that our new interferometry observations constrain the MOW geometry and velocity reduction, instead of the cutoff temperature (T_{mow}) or the thermal model. For scenarios with different combinations of slab parameters (e.g., subduction rate and age), T_{mow} that fits the data best can vary by tens of degrees (Figure 2.18). Nonetheless, the MOW structures consistently resemble a thickness of ~30 km across the slab at 410 km and gradually diminish to a depth of ~610 km at least. We also test a few different MOW models by varying its thicknesses at ~610 km (Figure 2.19a) to reduce the thermal constrain to some extent. MOWs thicker than ~20 km at bottom cannot reproduce our observed waveforms (Figures 2.19b-d), suggesting that the thinning of MOW is required. Still, it is possible that MOW can extend to greater depth (Figure 2.20), since our inter-source interferometry method cannot resolve even deeper slab structure due to our current deep earthquake geometry (Figure 2.19b).

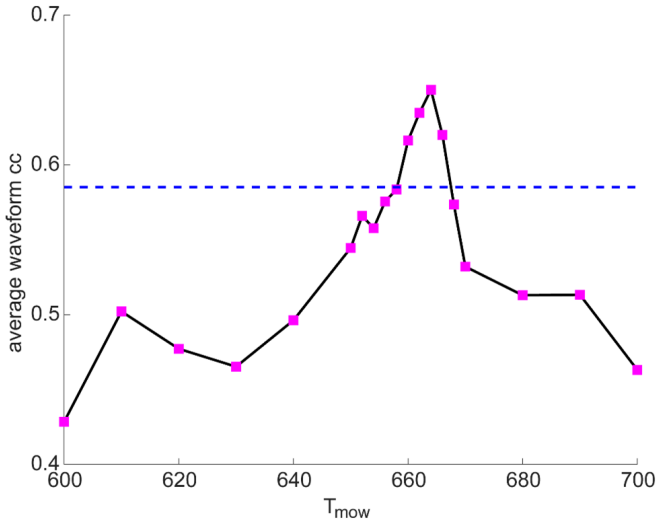

Figure 2.17: 5 Hz waveform correlation coefficients between observations and synthetics as a function of T_{mow}. Taking 5% reduction from our max correlation coefficient as the threshold (blue dashed line), the allowed T_{mow} ranges from 658°C to 668°C corresponding to a MOW thickness of 28~30 km at 410-km and gradually diminishes to a depth of 600 ~ 620 km.

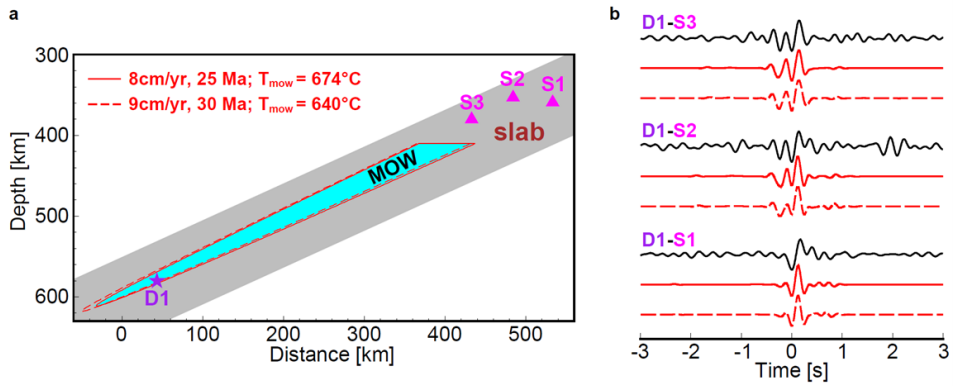

Figure 2.18: Trade-off between thermal modeling parameterizations and cut-off temperature (T_{mow}). (a). Slab profile with different MOW geometries. The cyan region represents our proposed model (8 cm/yr, 30 Ma; T_{mow} = 664°C) in Figure 2.14a. The red solid line and red dashed line indicate suggested MOW geometries for a slab with a subducting velocity of 8 cm/yr and thermal evolution time of 25 Ma, and a slab with a subducting velocity of 9 cm/yr and thermal evolution time of 30 Ma, respectively. The slab subducting velocity, thermal evolution time and kinetic cut-off temperature (T_{mow}) for each scenario are shown in the upper left corner. Note that although T_{mow} differs tens of degrees, the overall dimensions are nearly invariant. (b). 0.2~5 Hz waveform comparison of observations (black) and synthetics (red) with different MOW models shown in (a).

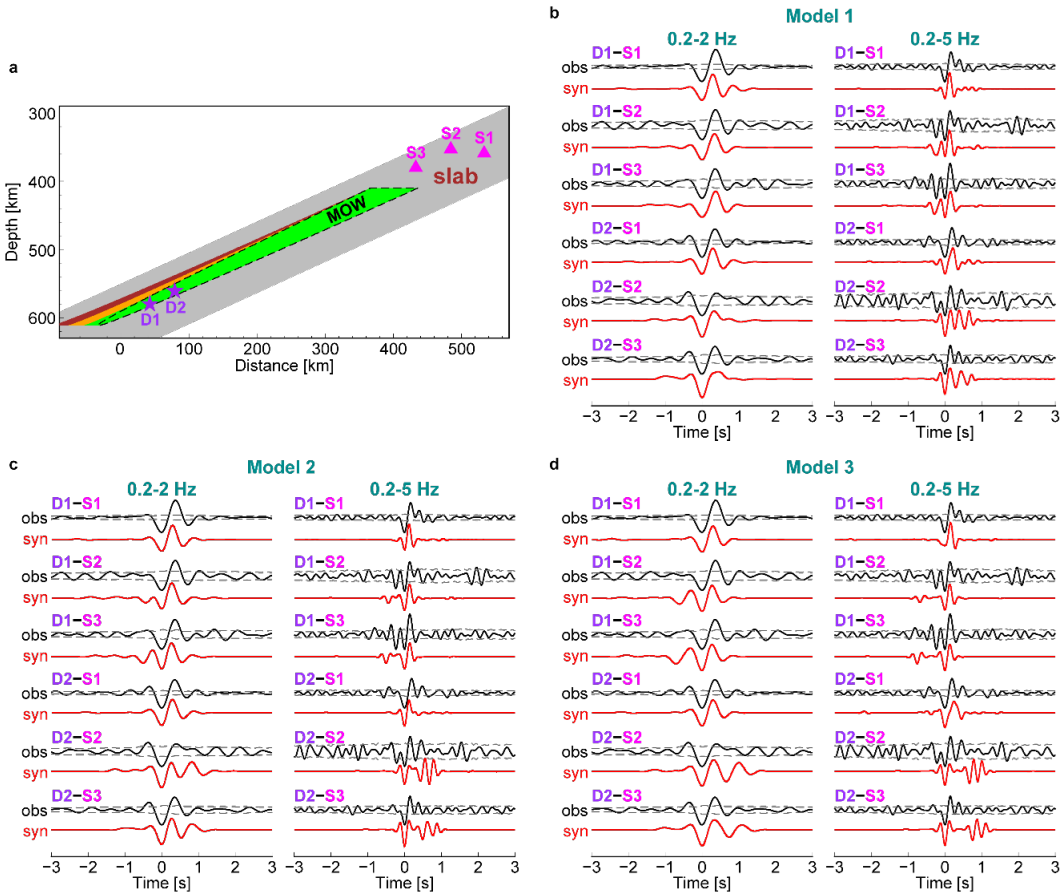

Figure 2.19: MOW geometry effect on the inter-source interferometric waveform fitting. (a). Slab profile with different MOW geometries. The black dashed line denotes our thermal modeling based best fitting model (T_{mow} = 664°C). The thickness of MOW gradually reduces to 10 km (green, Model 1), 20 km (orange, Model 2) and 30 km (brown, Model 3) at ~600 km from a thickness of 29 km at 410-km depth. (b). The waveform comparison of synthetics and observations for Model 1 at 0.2~2 Hz and 0.2~5 Hz. (c). and (d). are similar to (b), but for Model 2 and Model 3, respectively. Thicker MOWs at 600 km (Model 2 and Model 3) fail to reproduce the 2 Hz and 5 Hz observations for event pairs D1/D2-S2/S3.

2.5 Discussion and Conclusions

Compared to previously proposed MOW geometries in nearby regions, our MOW at 410-km depth is similar to that imaged by the receiver function (Kawakatsu and Yoshioka, 2011), but considerably thinner than that derived from travel time-based studies (Table 2.1). With our resolved MOW dimension, the delay of olivine phase transformation is estimated to increase the slab buoyancy by 1% below 410 km, which is comparable to the thermal slab buoyancy force (2–3%; Cammarano et al., 2003). Such extra buoyancy force generated by the metastable olivine could in turn reduce the slab subduction rate (Tetzlaff and Schmeling, 2000). Given

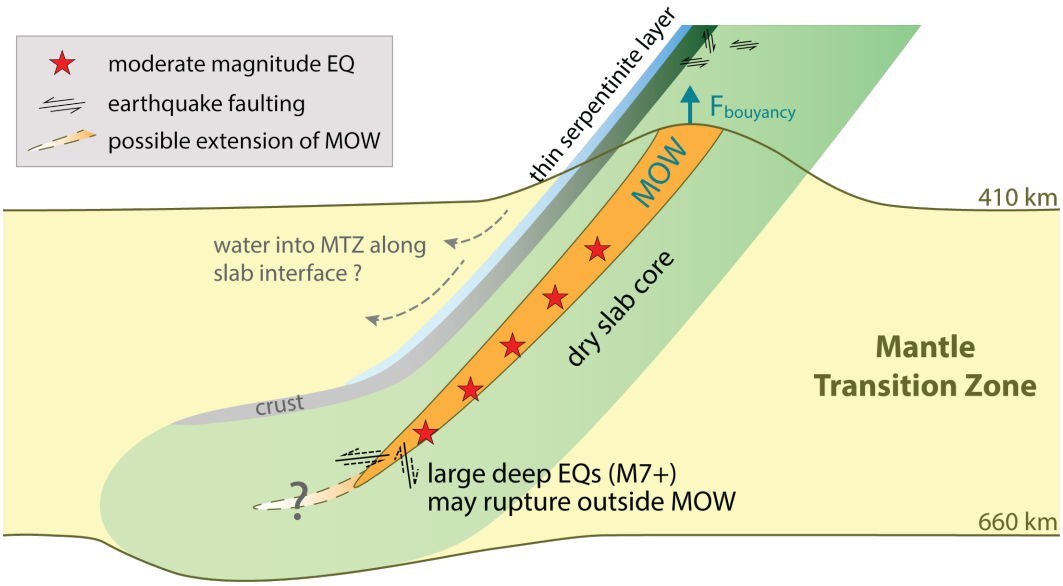

Figure 2.20: Schematic cross-section of subducted slab in the mantle transition zone. Metastable olivine persists in the slab core as a wedge extending down to the bottom of MTZ. The red stars indicate moderate magnitude earthquakes. Deep earthquakes can initiate within MOW by transformational faulting, but larger deep earthquakes (black dashed faulting) may potentially rupture outside MOW driven by other mechanisms. The existence of MOW requires that the core of subducted slab must carries negligible amount of water. But it is still possible that the water can be transported into the mantle transition zone along the slab interface.

the age of Japan trench (Sdrolias and Müller, 2006), the associated metastable olivine for a 130-Ma oceanic lithosphere is estimated to slow down the subduction rate by up to ~12% (Bina et al., 2001). For colder slabs, such as Tonga, the effect might be even stronger, due to the presumably larger MOW. In our preferred scenario (Figure 3.4), deep earthquakes D1 and D2 occur within MOW, supporting transformational faulting as the cause of deep earthquakes. Assuming a circular crack and a constant strain drop (Vallée, 2013), the metastable olivine thickness at 600-km depth is equivalent to the dimension of a moderate-magnitude earthquake (Mw7) that ruptures across the slab. To host larger deep earthquakes (e.g., Mw7+) with larger rupture dimensions, which did occur beneath the Japan Sea and in other warmer subduction zones with potentially thinner MOWs, the slip instability probably nucleates within MOW by transformational faulting and later propagate outside driven by other mechanisms (e.g., the thermal shear instability). The switch of mechanism around M6–7 would break the self-similarity of deep earthquake sizes and cause a change in the Gutenberg-Richter distributions (i.e., b values), which is recently observed (Zhan, 2017). Furthermore, models of great deep earthquakes,

such as the 1994 Mw8.2 Bolivia earthquake and the 2018 Mw8.0 Fiji-Tonga doublet, also imply two-stage rupture processes and exemplify local slab temperature as the critical factor for deep earthquakes (Jia et al., 2020; Zhan et al., 2014b).

The depth extent of our proposed MOW indicates an extremely dry Pacific slab core (<75 wt ppm) in the MTZ beneath the Japan Sea (Figure 2.20; Kawakatsu and Yoshioka, 2011; Du Frane et al., 2013). However, the arc volcanism, intermediate-depth earthquakes, and high-resolution tomography models all point to substantially hydrated slab above 200-km depth (Cai et al., 2018; Hasegawa and Nakajima, 2017), potentially through outer-rise plate-bending faults that cut deep into the incoming plate as pathways for water (Ranero et al., 2003). Therefore, the water associated with these faults must be expelled almost completely into the mantle at intermediate depths (Kawakatsu and Watada, 2007), carrying negligible amount of water into the MTZ (Green II et al., 2010). Conversely, garnering evidences from ultradeep diamond inclusions (Pearson et al., 2014), mineral experiments (Kohlstedt et al., 1996) and electromagnetic induction data (Kelbert et al., 2009) have demonstrated that the MTZ can, at least locally, harbor substantial amount of water (up to ~2.5 wt%). Given the distance between our MOW and plate interface (~24 km) and the hydrogen diffusion coefficients of olivine and its polymorphs (Hae et al., 2006), it is still possible that a thin layer near the subducting plate provide potential pathways for transporting water into MTZ, such as a narrow serpentinite channel on top of the slab (Kawakatsu and Watada, 2007). Or instead of linking the water reservoir in MTZ to current subduction, the wet MTZ might be possibly associated with other tectonic processes (Green II et al., 2010; Hirschmann, 2006).

2.6 Appendix

Inter-source interferometry theory

Given two sources that located at x_1 and x_2 being surrounded by a boundary S of receivers $x^{'}$, (Curtis et al., 2009) derived the theory of inter-source interferometry based on the representation theorem and source-receiver reciprocity. For actual earthquake recordings in elastic media, the inter-source interferometric response between x_1 and x_2 in the frequency domain can be approximated as (equation 16 in Curtis et al., 2009 Supplementary Material):

$$M^2_{ip} M^1_{mq} \partial_p \partial_q G^h_{im}(x_2|x_1) = iK\omega \oint_S u_n(x^{'}|x_2) u^*_n(x^{'}|x_1) dx^{'} \tag{2.1}$$

where M^1_{mq} represents the moment tensor component of source x_1 with a pair of

opposite force couples acting in mth direction and separated in qth direction. M^2 corresponds to the moment tensor of source x_2. ∂_q and ∂_p are the partial derivatives with respect to the qth and pth direction at location x_1 and x_2, respectively. $G^h_{im}(x_2|x_1)$ is defined as $G^h_{im}(x_2|x_1) = G_{im}(x_2|x_1) - G^*_{im}(x_2|x_1)$, where $G_{im}(x_2|x_1)$ represents the causal Green's function from x_1 to x_2 and $G^*_{im}(x_2|x_1)$ represents the acausal Green's function due to the wavefield propagating from receivers on S to x_2 before refocusing at x_1. Subscripts i and m are the ith component of the displacement at x_2 and mth direction for a point source at x_1, respectively. K is a constant and ω is the frequency. $u_n(x^{'}|x_2)$ is the displacement recorded at location $x^{'}$ from source x_2 and $u^*_n(x^{'}|x_1)$ is the conjugate form of $u_n(x^{'}|x_1)$. Essentially, the integral at the right side of equation 2.1 is the summation of cross-correlations of displacements recorded at receiver $x^{'}$ from earthquake x_1 and x_2. To better understand the quantity that is estimated by the cross correlations, we rewrite the left side of equation 2.1 as

$$M^2_{ip} M^1_{mq} \partial_p \partial_q G^h_{im}(x_2|x_1) = M^2_{ip} \partial_p [M^1_{mq} \partial_q G^h_{im}(x_2|x_1)] \tag{2.2}$$

In the frequency domain, the term $M^1_{mq} \partial_q G^h_{im}(x_2|x_1)$ is, by definition, the ith component displacement u_i from source x_1 to 'virtual receiver' x_2:

$$u_i(x_2|x_1) = M^1_{mq} \partial_q G^h_{im}(x_2|x_1) \tag{2.3}$$

Then equation 2.1 can be written as:

$$M^2_{ip} \partial_p u_i(x_2|x_1) = iK\omega \oint_S u_n(x^{'}|x_2) u^*_n(x^{'}|x_1) dx^{'} \tag{2.4}$$

For the left side, $\partial_p u_i(x_2|x_1)$ is the dynamic strain at 'virtual receiver' x_2 triggered by passing waves from earthquake x_1. The moment tensor M^2_{ip} of the earthquake occurred at x_2 determines the combination of dynamic strains measured in the inter-source interferometry. Although $x^{'}$ should have a complete azimuthal coverage along S, the stationary phase approximation theory has shown that the integral on the right side of equation 2.4 is mainly contributed from $x^{'}$ near the region along the extension between earthquake x_1 and x_2 (Snieder, 2004). Thus, when applying the inter-source interferometry to real data, the stationary phase approximation greatly loosens the receiver geometry restriction. This theory has been successfully applied to surface waves (Curtis et al., 2009), but in general, the above conclusion also works for other types of seismic wave, such as the body wave. Here we consider the compressional P wave displacement $u^P_i(x_2|x_1)$, substituting into equation 2.4:

$$M_{ip}^{2}\partial_{p}u_{i}^{P}(x_{2}|x_{1}) = iK\omega \oint_{S} u_{n}^{P}(x^{'}|x_{2})u_{n}^{P*}(x^{'}|x_{1})dx^{'} \tag{2.5}$$

For a vertical strike slip earthquake, the moment tensor is given by $M_{xy} = M_{yx} = 1$ with other components being 0. Therefore, the left-hand side of equation 2.5 becomes:

$$\partial_{y}u_{x}^{P}(x_{2}|x_{1}) + \partial_{x}u_{y}^{P}(x_{2}|x_{1}) = e_{xy}^{P}(x_{2}|x_{1}) + e_{yx}^{P}(x_{2}|x_{1}) \tag{2.6}$$

where e_{xy}^{P} and e_{yx}^{P} are the horizontal transient strains at virtual receiver x_2. The strain combination for other types of earthquake mechanisms is summarized in Table 2.2.

Source Mechanism	Strain Components
45° dip slip	$e_{zz} - e_{yy}$
Vertical dip slip	$-e_{yz} - e_{zy}$
Vertical strike slip	$-e_{xy} - e_{yx}$
Isotropic explosion	$e_{xx} + e_{yy} + e_{zz}$

Table 2.2: Combinations of strain components measured for difference source mechanisms. Here we take coordinates (x,y,z) at the source as (North, East, Down).

Earthquake relocation and uncertainty estimation

We refined the centroid depth of D1 and S1 using ScS and sScS waveforms. Since the ScS and sScS phase propagate near-vertically through the earth interior at short distances, time differences between ScS and sScS are sensitive to the earthquake focal depth. We downloaded three component seismograms of regional stations (0-30 degrees) from F-net (Okada et al., 2004) and GSN (station MDJ), removed the instrumental response, rotated into tangential components, and filtered with a two-pole Butterworth band-pass filter of 0.02-0.05 Hz. We used a frequency-wavenumber method to synthesize ScS and sScS waveforms. In the calculation, the velocity model was constructed by combining the Crust1.0 (Laske et al., 2013) and IASP91 (Kennett and Engdahl, 1991). We cross-correlated the observed tangential seismograms with synthetic waveforms computed for different focal depths in a time window from 50 s before to 350 s after the predicted ScS (Figure 2.2). The highest correlation coefficient case corresponds to the optimal focal depth at each station. We then averaged values over all the stations to estimate the centroid depths of S1 and D1 to be 359 ± 6.1 km and 580 ± 7.8 km at 95% confidence level, respectively.

For the horizontal locations of D1 and S1, we adopted the results from ISC-EHB catalog based on which the Slab2.0 model was constructed (Hayes et al., 2018). Given S1 as a reference earthquake, we relatively relocated the other two events S2 and S3 using the traveltime data documented by Japan Meteorological Agency (JMA). Only P wave arrival times labelled as high-precision onset picks were used for the traveltime data. We performed a grid-search method to invert for the longitude, latitude and depth that minimizes the L2-norm misfit between predicted and reported traveltime differences. The horizontal locations and depths of all earthquakes are listed in Table 2.3, and the arrival time difference comparison between observed and predicted is shown in Figure 2.3a. With a Gaussian assumption, we calculated the earthquake location probability density function (PDF), which is proportional to $e^{-\frac{1}{2}(g(\mathbf{m})-d)^T C_D^{-1}(g(\mathbf{m})-d)}$, where $g(\mathbf{m})$ and d are the estimated and observed arrival times, respectively. C_D is the covariance matrix representing the measurement and model uncertainty. Here, we assigned a 0.2 s arrival time uncertainty to the covariance matrix, and the resulting PDFs for D2 and D3 are shown in Figure 2.3b and 2.3c, respectively. The maximum likelihood point is taken as our best location and the 95% probability contour represents our relative location error (Figure 2.3). In fact, we found that the our relocated S2 and S3 locations are consistent with ISC-EHB results. So, for deep earthquakes D1 and D2, we directly adopted their horizontal locations from ISC-EHB catalog and systematically shifted them at depth to anchor D1 at 580 km that given by ScS-sScS waveform fitting.

It has been shown that the EHB catalog globally provides 25 km accuracy at the 90% confidence level by relocating the ground true events (GT5) using the EHB procedures (Bondár et al., 2004). Similarly, to calculate the ISC-EHB location uncertainties near Japan, we selected 139 ISC-EHB reported earthquakes that occurred within the Japanese network after 2004. Assuming these event locations reported by JMA are "ground truth" within an uncertainty of 5 km (GT5), the estimated horizontal and vertical location errors of ISC-EHB are 9.55 km and 9.62 km at 95% confidence level, respectively (Table 2.3), which are more accurate than the global value due to denser teleseismic networks in the past decade.

Event ID	YYYY/MM/DD	Magnitude	Depth [km]	Longitude [°]	Latitude [°]
D1	2009/08/10	mb 4.8	580 ± 7.8	130.58 ± 0.09	43.52 ± 0.09
D2	2011/01/07	mb 4.8	561 ± 9.6	131.04 ± 0.09	43.02 ± 0.09
S1	2010/02/05	mb 5.0	359 ± 6.1	135.78 ± 0.09	40.64 ± 0.09
S2	2012/07/17	mb 4.4	353 ± 9.6	135.56 ± 0.09	41.18 ± 0.09
S3	2012/07/17	N/A	380 ± 9.6	135.28 ± 0.09	41.70 ± 0.09

Table 2.3: Earthquake origin date, magnitude and relocation results for earthquakes used in our inter-source interferometry study. The earthquake date and magnitude information are from ISC-EHB catalog.

Thermal modeling for the Japan slab

For modeling the two-dimensional slab thermal profile, we used a finite element code UNDERWORLD2 (Moresi et al., 2007) to solve the convection-diffusion equation.

$$\frac{\partial T}{\partial t} = \nabla \cdot (\kappa \nabla T) - \nabla \cdot (vT) \tag{2.7}$$

where T, t, κ and v are the temperature, time, thermal diffusivity and mantle flow velocity. The thermal diffusivity is set to be $10^{-6}\ m^2/s$. The initial thermal structure of subducting slab is constructed from a plate cooling model of a 95 km thick lithosphere with the age (~130 Ma) of Pacific plate at the trench position (Sdrolias and Müller, 2006). The mantle flow velocity field is given by the analytical solution for a corner flow model (Turcotte and Schubert, 2002), assuming a convergence velocity of 8 cm/yr (Sdrolias and Müller, 2006) and a 30° dip slab that is close to the slab surface delineated in Slab2.0 model (Hayes et al., 2018). In the corner flow model, the viscous mantle is divided by the descending slab into two parts: the arc corner above the slab and the oceanic corner below the slab. Given the velocity (U) and dipping angle (θ) of subducting slab, the velocity in arc corner, oceanic corner and subducting slab can be calculated as:

$$\begin{cases} v_x &= \frac{3\pi}{\pi^2-9} - \frac{18-3\sqrt{3}\pi}{\pi^2-9} \arctan\frac{y}{x} + (\frac{3\pi}{\pi^2-9}x + \frac{18-3\sqrt{3}\pi}{\pi^2-9}y)(\frac{-x}{x^2+y^2}) \\ v_y &= \frac{3\pi}{\pi^2-9} \arctan\frac{y}{x} + (\frac{3\pi}{\pi^2-9}x + \frac{18-3\sqrt{3}\pi}{\pi^2-9}y)(\frac{-y}{x^2+y^2}) \end{cases} \quad for\ arc\ corner \tag{2.8}$$

$$\begin{cases} v_x &= -\frac{(1-3\sqrt{3})\pi}{5\pi+3} - \frac{3\sqrt{3}-6}{5\pi+3} \arctan\frac{y}{x} + (\frac{-3}{5\pi+3}x + \frac{3\sqrt{3}-6}{5\pi+3}y)(\frac{-x}{x^2+y^2}) \\ v_y &= \frac{3\pi}{5\pi+3} - \frac{3}{5\pi+3} \arctan\frac{y}{x} + (\frac{-3}{5\pi+3}x + \frac{3\sqrt{3}-6}{5\pi+3}y)(\frac{-y}{x^2+y^2}) \end{cases} \quad for\ oceanic\ corner \tag{2.9}$$

$$\begin{cases} v_x &= U \cdot \sin\theta \\ v_y &= U \cdot \cos\theta \end{cases} for\ subducting\ slab \tag{2.10}$$

where v_x and v_y are the horizontal and vertical components of the mantle flow, respectively.

The simulated box dimension is 800 km × 2400 km with a discretized element spacing of 1 km. In the simulation, we placed the Dirichlet boundary condition on the surface and Neumann boundary conditions at the other three sides for the temperature field. In the meantime, the velocity field is kept invariant. For solving the governing equation, variables in equation 2.7 are non-dimensionalized with the following characteristic values:

$$\begin{cases} x_i &= dx_i^{'} \\ \kappa &= \kappa_o \kappa^{'} \\ v_i &= \frac{\kappa_o}{d} dv_i^{'} \\ t &= \frac{d^2}{\kappa_o} t^{'} \\ T &= T_m T^{'} \end{cases} \tag{2.11}$$

where symbols with primes are dimensionless. κ_0 is the reference thermal diffusivity with a value of 10^{-6} m^2/s. d and T_m denote the mantle thickness and mantle temperature which are 800 km and 1450 °C for our case. The slab is diffused and advected over a duration of 30 Ma which is long enough for surface material descending to the depth with assumed convergence rate.

Slab velocity profile setup

Assuming an olivine-rich pyrolite assemblage, we mapped the thermal anomalies in the depth range of 200~800 km into velocity and density perturbations using a scaling from (Cammarano et al., 2003). This scaling relation accounts for both anharmonic and anelastic effects with depth. For shallow velocity profile, we extended the seismic velocity and density perturbations inside slab at 200 km upward to the surface. The maximum P and S wave velocity perturbations within the slab are 4.5% and 6.0%, respectively, which agree well with the inferred velocity anomalies from seismic waveform studies (Zhan et al., 2014a). Our seismic velocity and density reference model is the IASP91 model (Kennett and Engdahl, 1991).

To simulate realistic coda waves, we added small scale heterogeneities in the lithosphere (above 200 km) described by a Von K*árm*á*n* type autocorrelation function (Sato et al., 2012) given as:

$$P(k_x, k_z) = \frac{4\pi\kappa\varepsilon^2 a_x a_z}{(1 + a_x^2 k_x^2 + a_z^2 k_z^2)^{\kappa+1}} \tag{2.12}$$

where P is the power spectral density function (PSDF), κ is the Hurst exponent which is assigned as 0.5 in our model. k_i is the wavenumber in ith direction. a_x and a_z are the correlation distances in the x and z components, respectively and ε is the mean square fractional fluctuation. For the velocity and density structures above 200 km, we imposed isotropic scatters outside the slab with $a_x = a_z = 5$ km and $\varepsilon = 2.0\%$, and elongated scatters within the slab with $a_x = 0.5$ km, $a_z = 10$ km and $\varepsilon = 2.5\%$, which is suggested by long duration coda wave observation in Japan (Furumura and Kennett, 2005).

2.7 Acknowledgement

We are grateful to Micheal Gurnis, Paul Asimow, Sidao Ni, and Wenbo Wu for discussions and suggestions. We are also grateful for reviews from two anonymous reviewers, which helped to improve the manuscript. Seismic data are collected from the Data Management Center of the Incorporated Research Institutions for Seismology (https://www.iris.edu/dms/nodes/dmc), Hi-net (http://www.hinet.bosai.go.jp/) and F-net (http://www.fnet.bosai.go.jp/). The earthquake catalog and focal mechanisms are downloaded from ISC-EHB distributed by the International Seismological Centre (ISC, http://www.isc.ac.uk/) and National Research Institute for Earth Science and Disaster Resilience (NIED, http://www.fnet.bosai.go.jp/event/search.php?LANG=en). The earthquake arrival time data is available at the Japan Meteorological Agency (JMA, http://www.data.jma.go.jp/svd/eqev/data/bulletin/index_e.html).

References

Bina, C. R. et al. (2001). Implications of slab mineralogy for subduction dynamics. In: *Physics of the Earth and Planetary Interiors* 127.1. Publisher: Elsevier, pp. 51–66. DOI: 10.1016/S0031-9201(01)00221-7.

Bondár, I. et al. (2004). Epicentre accuracy based on seismic network criteria. In: *Geophysical Journal International* 156.3. Publisher: Blackwell Science Ltd Oxford, UK, pp. 483–496. DOI: 10.1111/j.1365-246X.2004.02070.x.

Brace, W. F. and D. L. Kohlstedt (1980). Limits on lithospheric stress imposed by laboratory experiments. In: *Journal of Geophysical Research: Solid Earth* 85 (B11). Publisher: Wiley Online Library, pp. 6248–6252. DOI: 10.1029/JB085iB11p06248.

Cai, C. et al. (2018). Water input into the Mariana subduction zone estimated from ocean-bottom seismic data. In: *Nature* 563.7731. Publisher: Nature Publishing Group, pp. 389–392. DOI: 10.1038/s41586-018-0655-4.

Cammarano, F. et al. (2003). Inferring upper-mantle temperatures from seismic velocities. In: *Physics of the Earth and Planetary Interiors* 138.3. Publisher: Elsevier, pp. 197–222. DOI: 10.1016/S0031-9201(03)00156-0.

Campillo, M. and A. Paul (2003). Long-range correlations in the diffuse seismic coda. In: *Science* 299.5606. Publisher: American Association for the Advancement of Science, pp. 547–549. DOI: 10.1126/science.1078551.

Curtis, A. et al. (2009). Virtual seismometers in the subsurface of the Earth from seismic interferometry. In: *Nature Geoscience* 2.10. Publisher: Nature Publishing Group, pp. 700–704. DOI: 10.1038/ngeo615.

Du Frane, W. L. et al. (2013). Ringwoodite growth rates from olivine with 75 ppmw H_2O: Metastable olivine must be nearly anhydrous to exist in the mantle transition zone. In: *Physics of the Earth and Planetary Interiors* 219. Publisher: Elsevier, pp. 1–10. DOI: 10.1016/j.pepi.2013.04.001.

Furumura, T. and B. L. N. Kennett (2005). Subduction zone guided waves and the heterogeneity structure of the subducted plate: Intensity anomalies in northern Japan. In: *Journal of Geophysical Research: Solid Earth* 110 (B10). Publisher: Wiley Online Library. DOI: 10.1029/2004JB003486.

Furumura, T. et al. (2016). Enhanced waveguide effect for deep-focus earthquakes in the subducting Pacific slab produced by a metastable olivine wedge. In: *Journal of Geophysical Research: Solid Earth* 121.9. Publisher: Wiley Online Library, pp. 6779–6796. DOI: 10.1002/2016JB013300.

Green II, H. W. and P. C. Burnley (1989). A new self-organizing mechanism for deep-focus earthquakes. In: *Nature* 341.6244. Publisher: Nature Publishing Group, pp. 733–737. DOI: 10.1038/341733a0.

Green II, H. W. et al. (2010). Seismic evidence of negligible water carried below 400-km depth in subducting lithosphere. In: *Nature* 467.7317. Publisher: Nature Publishing Group, pp. 828–831. DOI: 10.1038/nature09401.

Hae, R. et al. (2006). Hydrogen diffusivity in wadsleyite and water distribution in the mantle transition zone. In: *Earth and Planetary Science Letters* 243.1. Publisher: Elsevier, pp. 141–148. DOI: 10.1016/j.epsl.2005.12.035.

Hasegawa, A. and J. Nakajima (2017). Seismic imaging of slab metamorphism and genesis of intermediate-depth intraslab earthquakes. In: *Progress in Earth and Planetary Science* 4.1. Publisher: Springer, pp. 1–31. DOI: 10.1186/s40645-017-0126-9.

Hayes, G. P. et al. (2018). Slab2, a comprehensive subduction zone geometry model. In: *Science* 362.6410. Publisher: American Association for the Advancement of Science, pp. 58–61. DOI: 10.1126/science.aat4723.

Hirschmann, M. M. (2006). Water, melting, and the deep Earth H_2O cycle. In: *Annu. Rev. Earth Planet. Sci.* 34. Publisher: Annual Reviews, pp. 629–653. DOI: 10.1146/annurev.earth.34.031405.125211.

Houston, H. (2015). 4.13 - Deep Earthquakes. In: *Treatise on Geophysics (Second Edition)*. Ed. by G. Schubert. Oxford: Elsevier, pp. 329–354. ISBN: 978-0-444-53803-1. DOI: 10.1016/B978-0-444-53802-4.00079-8.

Iidaka, T. and Y. Furukawa (1994). Double seismic zone for deep earthquakes in the Izu-Bonin subduction zone. In: *Science* 263.5150. Publisher: American Association for the Advancement of Science, pp. 1116–1118. DOI: 10.1126/science.263.5150.1116.

Iidaka, T. and D. Suetsugu (1992). Seismological evidence for metastable olivine inside a subducting slab. In: *Nature* 356.6370. Publisher: Nature Publishing Group, pp. 593–595. DOI: 10.1038/356593a0.

Jia, Z. et al. (2020). The 2018 Fiji Mw 8.2 and 7.9 deep earthquakes: One doublet in two slabs. In: *Earth and Planetary Science Letters* 531. Publisher: Elsevier, p. 115997. DOI: 10.1016/j.epsl.2019.115997.

Jiang, G. and D. Zhao (2011). Metastable olivine wedge in the subducting Pacific slab and its relation to deep earthquakes. In: *Journal of Asian Earth Sciences* 42.6. Publisher: Elsevier, pp. 1411–1423. DOI: 10.1016/j.jseaes.2011.08.005.

Jiang, G. et al. (2008). Seismic evidence for a metastable olivine wedge in the subducting Pacific slab under Japan Sea. In: *Earth and Planetary Science Letters* 270.3. Publisher: Elsevier, pp. 300–307. DOI: doi.org/10.1016/j.epsl.2008.03.037.

Jiang, G. et al. (2015). Detection of metastable olivine wedge in the western Pacific slab and its geodynamic implications. In: *Physics of the Earth and Planetary Interiors* 238. Publisher: Elsevier, pp. 1–7. DOI: 10.1016/j.pepi.2014.10.008.

Kanamori, H. et al. (1998). Frictional melting during the rupture of the 1994 Bolivian earthquake. In: *Science* 279.5352. Publisher: American Association for the Advancement of Science, pp. 839–842. DOI: 10.1126/science.279.5352.839.

Kaneshima, S. et al. (2007). Evidence for a metastable olivine wedge inside the subducted Mariana slab. In: *Earth and Planetary Science Letters* 258.1. Publisher: Elsevier, pp. 219–227. DOI: 10.1016/j.epsl.2007.03.035.

Kawakatsu, H. and S. Watada (2007). Seismic evidence for deep-water transportation in the mantle. In: *Science* 316.5830. Publisher: American Association for the Advancement of Science, pp. 1468–1471. DOI: 10.1126/science.1140855.

Kawakatsu, H. and S. Yoshioka (2011). Metastable olivine wedge and deep dry cold slab beneath southwest Japan. In: *Earth and Planetary Science Letters* 303.1. Publisher: Elsevier, pp. 1–10. DOI: 10.1016/j.epsl.2011.01.008.

Kelbert, A. et al. (2009). Global electromagnetic induction constraints on transition-zone water content variations. In: *Nature* 460.7258. Publisher: Nature Publishing Group, pp. 1003–1006. DOI: 10.1038/nature08257.

Kennett, B. L. N. and E. R. Engdahl (1991). Traveltimes for global earthquake location and phase identification. In: *Geophysical Journal International* 105.2. Publisher: Oxford University Press, pp. 429–465. DOI: 10.1111/j.1365-246X.1991.tb06724.x.

Kennett, B. L. N. and T. Furumura (2008). Stochastic waveguide in the lithosphere: Indonesian subduction zone to Australian craton. In: *Geophysical Journal International* 172.1. Publisher: Blackwell Publishing Ltd, pp. 363–382. DOI: 10.1111/j.1365-246X.2007.03647.x.

Kirby, S. H. et al. (1996). Metastable mantle phase transformations and deep earthquakes in subducting oceanic lithosphere. In: *Reviews of Geophysics* 34.2. Publisher: Wiley Online Library, pp. 261–306. DOI: 10.1029/96RG01050.

Kohlstedt, D. L. et al. (1996). Solubility of water in the α, β and γ phases of $(Mg, Fe)_2SiO_4$. In: *Contributions to Mineralogy and Petrology* 123.4. Publisher: Springer, pp. 345–357. DOI: 10.1007/s004100050161.

Koper, K. D. and D. A. Wiens (2000). The waveguide effect of metastable olivine in slabs. In: *Geophysical Research Letters* 27.4. Publisher: Wiley Online Library, pp. 581–584. DOI: 10.1029/1999GL011007.

Koper, K. D. et al. (1998). Modeling the Tonga slab: Can travel time data resolve a metastable olivine wedge? In: *Journal of Geophysical Research: Solid Earth* 103 (B12). Publisher: Wiley Online Library, pp. 30079–30100. DOI: 10.1029/98JB01517.

Kubo, A. et al. (2002). NIED seismic moment tensor catalogue for regional earthquakes around Japan: quality test and application. In: *Tectonophysics* 356.1. Publisher: Elsevier, pp. 23–48. DOI: 10.1016/S0040-1951(02)00375-X.

Kubo, T. et al. (1998). Effects of water on the α-βtransformation kinetics in San Carlos olivine. In: *Science* 281.5373. Publisher: American Association for the Advancement of Science, pp. 85–87. DOI: 10.1126/science.281.5373.85.

Laske, G. et al. (2013). Update on CRUST1. 0—A 1-degree global model of Earth's crust. In: *Geophysical Research Abstracts*. Vol. 15, p. 2658.

Li, D. et al. (2014). Global synthetic seismograms using a 2-D finite-difference method. In: *Geophysical Journal International* 197.2, pp. 1166–1183. ISSN: 0956-540X. DOI: 10.1093/gji/ggu050.

Meade, C. and R. Jeanloz (1991). Deep-focus earthquakes and recycling of water into the Earth's mantle. In: *Science* 252.5002. Publisher: American Association for the Advancement of Science, pp. 68–72. DOI: 10.1126/science.252.5002.68.

Moresi, L. et al. (2007). Computational approaches to studying non-linear dynamics of the crust and mantle. In: *Physics of the Earth and Planetary Interiors* 163.1. Publisher: Elsevier, pp. 69–82. DOI: 10.1016/j.pepi.2007.06.009.

Mosenfelder, J. L. et al. (2001). Experimental constraints on the depth of olivine metastability in subducting lithosphere. In: *Physics of the Earth and Planetary Interiors* 127.1. Publisher: Elsevier, pp. 165–180. DOI: 10.1016/S0031-9201(01)00226-6.

Ogawa, M. (1987). Shear instability in a viscoelastic material as the cause of deep focus earthquakes. In: *Journal of Geophysical Research: Solid Earth* 92 (B13). Publisher: Wiley Online Library, pp. 13801–13810. DOI: 10.1029/JB092iB13p13801.

Okada, Y. et al. (2004). Recent progress of seismic observation networks in Japan—Hi-net, F-net, K-NET and KiK-net—. In: *Earth, Planets and Space* 56.8. Publisher: SpringerOpen, pp. xv–xxviii. DOI: 10.1186/BF03353076.

Pearson, D. G. et al. (2014). Hydrous mantle transition zone indicated by ringwoodite included within diamond. In: *Nature* 507.7491. Publisher: Nature Publishing Group, pp. 221–224. DOI: 10.1038/nature13080.

Ranero, C. R. et al. (2003). Bending-related faulting and mantle serpentinization at the Middle America trench. In: *Nature* 425.6956. Publisher: Nature Publishing Group, pp. 367–373. DOI: 10.1038/nature01961.

Sato, H. et al. (2012). *Seismic wave propagation and scattering in the heterogeneous earth*. Springer Science & Business Media. ISBN: 978-3-642-44318-3. DOI: 10.1007/978-3-642-23029-5.

Scholz, C. H. (1998). Earthquakes and friction laws. In: *Nature* 391.6662. Publisher: Nature Publishing Group, pp. 37–42. DOI: 10.1038/34097.

Schubnel, A. et al. (2013). Deep-focus earthquake analogs recorded at high pressure and temperature in the laboratory. In: *Science* 341.6152. Publisher: American Association for the Advancement of Science, pp. 1377–1380. DOI: 10.1126/science.1240206.

Sdrolias, M. and R. D. Müller (2006). Controls on back-arc basin formation. In: *Geochemistry, Geophysics, Geosystems* 7.4. Publisher: Wiley Online Library. DOI: 10.1029/2005GC001090.

Snieder, R. (2004). Extracting the Green's function from the correlation of coda waves: A derivation based on stationary phase. In: *Physical Review E* 69.4. Publisher: APS, p. 046610. DOI: 10.1103/PhysRevE.69.046610.

Takemura, S. et al. (2015). Velocity increase in the uppermost oceanic crust of subducting Philippine Sea plate beneath the Kanto region due to dehydration inferred from high-frequency trapped P waves. In: *Earth, Planets and Space* 67.1. Publisher: SpringerOpen, pp. 1–14. DOI: 10.1186/s40623-015-0210-6.

Tetzlaff, M. and H. Schmeling (2000). The influence of olivine metastability on deep subduction of oceanic lithosphere. In: *Physics of the Earth and Planetary Interiors* 120.1. Publisher: Elsevier, pp. 29–38. DOI: 10.1016/S0031-9201(00)00139-4.

Tonegawa, T. and K. Nishida (2010). Inter-source body wave propagations derived from seismic interferometry. In: *Geophysical Journal International* 183.2. Publisher: Blackwell Publishing Ltd Oxford, UK, pp. 861–868. DOI: 10.1111/j.1365-246X.2010.04753.x.

Turcotte, D. L. and G. Schubert (2002). *Geodynamics*. Cambridge University Press. ISBN: 9780521186230. DOI: 10.1017/CBO9780511843877.

Vallée, M. (2013). Source time function properties indicate a strain drop independent of earthquake depth and magnitude. In: *Nature Communications* 4.1. Publisher: Nature Publishing Group, pp. 1–6. DOI: 10.1038/ncomms3606.

Vidale, J. E. et al. (1991). Waveform effects of a metastable olivine tongue in subducting slabs. In: *Geophysical Research Letters* 18.12. Publisher: Wiley Online Library, pp. 2201–2204. DOI: 10.1029/91GL02588.

Wang, Y. et al. (2017). A laboratory nanoseismological study on deep-focus earthquake micromechanics. In: *Science Advances* 3.7. Publisher: American Association for the Advancement of Science, e1601896. DOI: 10.1126/sciadv.1601896.

Wiens, D. A. et al. (1993). Evidence for transformational faulting from a deep double seismic zone in Tonga. In: *Nature* 364.6440. Publisher: Nature Publishing Group, pp. 790–793. DOI: 10.1038/364790a0.

Zhan, Z. (2017). Gutenberg–Richter law for deep earthquakes revisited: A dual-mechanism hypothesis. In: *Earth and Planetary Science Letters* 461. Publisher: Elsevier, pp. 1–7. DOI: 10.1016/j.epsl.2016.12.030.

Zhan, Z. et al. (2014a). Imaging subducted slab structure beneath the Sea of Okhotsk with teleseismic waveforms. In: *Physics of the Earth and Planetary Interiors* 232. Publisher: Elsevier, pp. 30–35. DOI: 10.1016/j.pepi.2014.03.008.

Zhan, Z. et al. (2014b). Rupture complexity of the 1994 Bolivia and 2013 Sea of Okhotsk deep earthquakes. In: *Earth and Planetary Science Letters* 385. Publisher: Elsevier, pp. 89–96. DOI: 10.1016/j.epsl.2013.10.028.

Chapter 3

SMALL-SCALE INTRA-SLAB HETEROGENEITY WEAKENS INTO THE MANTLE TRANSITION ZONE

Shen, Zhichao, Z. Zhan, and J. M. Jackson (2021). Small-scale intra-slab heterogeneity weakens into the mantle transition zone. In: *Geophysical Research Letters*, e2021GL094470. DOI: 10.1029/2021GL094470.

3.1 Abstract

Small-scale intra-slab heterogeneity is well documented seismically in multiple subduction zones, but its nature remains elusive. Previous efforts have been mostly focusing on the scattering strength at intermediate depth (<350 km), without constraining its evolution as a function of depth. Here, we illustrate that the inter-source interferometry method, which turns deep earthquakes into virtual receivers, can resolve small-scale intra-slab heterogeneity in the mantle transition zone. The interferometric waveform observations in the Japan subduction zone require weak scattering (<1.0%) within the slab below 410 km. Combining with previous studies that suggest high heterogeneity level (~2.5%) at intermediate depth, we conclude that the small-scale intra-slab heterogeneity weakens as slabs subduct. We suggest that the heterogeneities are caused by intra-slab hydrous minerals, and the decrease in their scattering strength with depth reveals processes associated with dehydration of subducting slabs.

3.2 Introduction

Multiscale seismic structures of subducting slabs provide fundamental constraints on the slab thermal and petrological properties. Extensive investigations have been conducted on the large- (>100 km) and intermediate-scale (10–100 km) slab structures. For example, subducting plates imaged from tomographic models are characterized as large-scale high-velocity anomalies descending into the mantle with complicated destinies (e.g., Fukao and Obayashi, 2013; Goes et al., 2017; Li et al., 2008; Lu et al., 2019; Ritsema et al., 2011; Simmons et al., 2012; Zhao, 2004). These high velocities are thought to be primarily temperature controlled and thus can be used to constrain the thermal-petrological state of the slab core (Cammarano et al., 2003; Zhan et al., 2014). On the intermediate scale, deterministic seismic

waveform modeling suggests that distinct oceanic crusts remain to a depth of ~150 km globally with a velocity reduction up to 15%, implying a vigorous slab hydration process along the top of subducting plates (Abers, 2000; Abers et al., 2003; Garth and Rietbrock, 2014b; Garth and Rietbrock, 2017; Omori et al., 2004; Savage, 2012). As another example of an intermediate-scale slab structure, low-velocity metastable olivine wedge (MOW), which consists of low-pressure olivine polymorphs within a cold slab in the mantle transition zone (MTZ), has been confirmed beneath the Japan Sea (Iidaka and Suetsugu, 1992). The recently revealed dimension of MOW supports transformational faulting as the initial mechanism of deep-focus earthquakes and a dry slab core (Shen and Zhan, 2020; Zhan, 2020).

In contrast to studies on the large and intermediate scales, small-scale (<10 km) slab structures have been mostly studied by stochastically modeling high-frequency scattered waves. To explain the high-frequency coda of long duration and large amplitude along the Japan trench from deep earthquakes, Furumura and Kennett (2005) proposed a laminar intra-slab heterogeneity model after ruling out slab attenuation and hydrous oceanic crust as possible causes. The intra-slab scatterers are described by a Von K*á*rm*á*n distribution with a downdip correlation wavelength of 10 and 0.5 km in thickness with a velocity fluctuation of 2.5%. Since then, a similar heterogeneity level at intermediate depth (<350 km) has been suggested in a few other old subducting plates (Furumura and Kennett, 2008; Sun et al., 2014). Such stochastic structure is conjectured to represent melt-rich shear bands or channels which initially formed near the mid-ocean ridge, preserved during the thickening of the oceanic plate and aligned to the horizontal direction by the relative shear mantle flow (Sun et al., 2014). Alternatively, Garth and Rietbrock (2014b) attributed the extended P wave coda to an elongated intra-slab heterogeneity model oriented with an angle similar to the fault angles at the outer rise. In this manner, the fine-scale structures are associated with serpentinized faults that can penetrate deeper in the slab due to unbending forces and cycle a great amount of water into the mantle. Yet, given the limited seismological observations at intermediate depth range, there is no broadly accepted petrological understanding for the small-scale intra-slab heterogeneity.

To interrogate the nature of these elongated scatterers, it may help to unveil their fate at larger depth using seismic scattering strength as an indicator. For example, the small-scale scatterers can be much weaker at depth due to the slab dehydration if they are located along (previously) hydrated faults. However, compared to intermediate depth, seismic signatures of intra-slab heterogeneity in the MTZ are difficult to

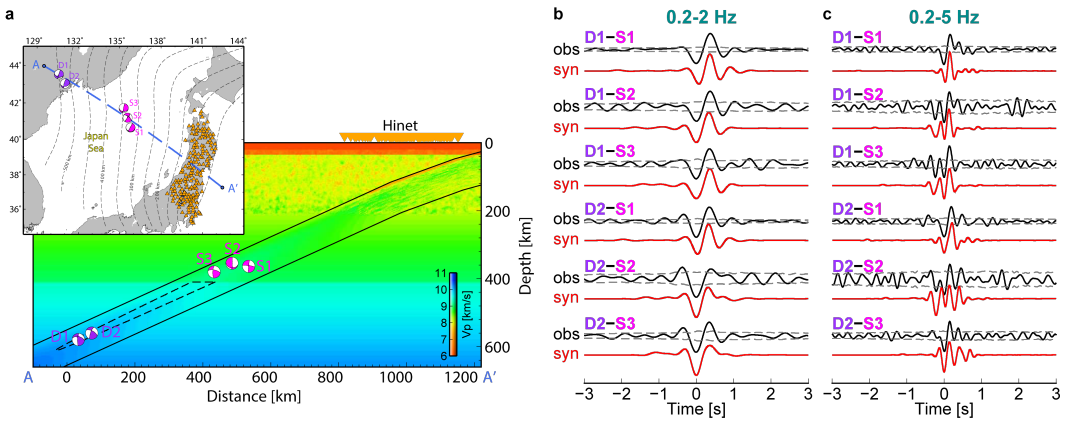

Figure 3.1: Metastable olivine wedge (MOW) model beneath the Japan Sea. (a) Map view of our studied region and the P wave velocity profile along AA'. The black solid and dashed lines denote the subducting Pacific slab (Hayes et al., 2018) and a MOW model beneath the Japan Sea (Shen and Zhan, 2020). Orange triangles are Hi-net stations used for inter-source interferometry. (b) 0.2-2 Hz and (c) 0.2-5 Hz waveform comparison between interferometric observations and synthetics (no scattering is imposed here) for all six deep earthquake pairs. The gray dashed lines denote the noise level.

separate from the waveform complexities caused by the shallower slab, lithospheric, and crustal scattering (Chen et al., 2007), as well as deep slab structure MOW (Furumura et al., 2016). To address this challenge, we incorporate the MOW model from (Shen and Zhan, 2020) and investigate intra-slab heterogeneity using an inter-source interferometry method which has been shown effective in isolating deep slab signals. In this paper, we first validate the inter-source interferometry technique for small-scale intra-slab heterogeneity with numerical simulations. Then, to explain the interferometric observations, we invoke different intra-slab heterogeneity models in the MTZ beneath the Japan Sea. Combining previous studies for the intermediate depth range, we suggest that the intra-slab scattering level decreases with depth and correlates with the process associated with slab dehydration.

3.3 Deep Slab Model for Inter-source Interferometry

Inter-receiver interferometry has been widely used to reconstruct the Green's function between receiver pairs given a diffusive seismic wavefield (Campillo and Paul, 2003; Shapiro et al., 2005). Similarly, due to the reciprocity theorem that interchanges the receivers and sources, the inter-source interferometry synthesizes the transient strain triggered by passing seismic waves from one source to the other (Curtis et al., 2009). This is as if we convert one of the earthquakes into a virtual

"seismometer" and record the other event. The inter-source interferometry method has succeeded in retrieving the seismic response between earthquakes in both global (Curtis et al., 2009) and regional scales (Eulenfeld, 2020; Tonegawa and Nishida, 2010), providing unprecedented resolution in revealing the source-side velocity structure. In particular, for the subducting slab scenario, this novel approach can isolate the deep slab from shallow lithospheric structures by cross-correlating coda waves from deep earthquakes at common stations. Previously, with Hi-net data, Shen and Zhan (2020) found that the inter-source interferometric waveforms from six deep earthquake pairs present coherent negative pulses at long period (0.2-2 Hz) while vary sharply at shorter period (0.2-5 Hz; Figure 3.1). After ruling out errors in the focal mechanism and signals related to the subducting crust, they confirmed the existence of MOW beneath the Japan Sea ~30-km thick at 410-km depth and gradually thinning to a depth of at least 580 km with a velocity reduction of 5% for P wave and 7% for S wave (Figure 3.1a).

Building on the Shen and Zhan (2020) result, we construct the slab profile initially from a thermal model tuned for the Japan subduction zone (Moresi et al., 2007; Sdrolias and Müller, 2006) and implement a MOW delineated by a temperature contour of $T_{mow} = 664^{\circ}C$ within the slab below 410 km. To describe the small-scale heterogeneity, we adopt the Von K*á*rm*á*n type autocorrelation function (ACF) given as (Sato et al., 2012)

$$P(k_x, k_z) = \frac{4\pi\kappa\varepsilon^2 a_x a_z}{(1 + a_x^2 k_x^2 + a_z^2 k_z^2)^{\kappa+1}} \tag{3.1}$$

where P is the power spectral density function and κ is the Hurst exponent set as 0.5 in this study. k_i is the wavenumber in ith direction, ε is the mean square fractional fluctuation, and a_x and a_z are the correlation distances in the orthogonal x (slab-parallel) and z (slab-normal) components, respectively. Note that the Von K*á*rm*á*n type ACF is designed to describe a turbid scenario enriching short-scale components using a few parameters and thus cannot capture the full range of heterogeneity effects that may be present in the slab. To produce realistic coda on the surface stations, we incorporate isotropic heterogeneity with $a_x = a_z = 10$ km and $\varepsilon = 2.0\%$ in the lithosphere (<210 km) and laminar intra-slab scatterers with $a_x = 10$ km, $a_z = 0.5$ km and $\varepsilon = 2.5\%$ at intermediate depth (70-350 km) following Furumura and Kennett (2005).

Guided by previous small-scale scatter studies for intermediate depths, we test a variety of intra-slab heterogeneity models below 410 km. The heterogeneity models are simultaneously superimposed on our background P and S wave velocities and

densities of the subducting slab and can be generally categorized into two groups (Melt-type and Fault-type) with different combinations of ACF parameters and the orientation of elongation (apparent dipping angle to the slab surface; Table 3.1). Melt-type models: slab-parallel scatterers with a_x = 10 km, a_z = 0.5 km, and a set of heterogeneity level ε ranging from 0.0% to 2.5% with an interval of 0.5% (Furumura and Kennett, 2005), which are referred to as Melt_constant models. We also linearly increase ε from the slab surface (0.5%) to the bottom (2.5%), termed the Melt_basal model. This strong basal heterogeneity model is proposed to resolve a discrepancy between seismological and experimental observations (Kennett and Furumura, 2015). Fault-type models: elongated scatterers with a dipping angle of 25° to the slab surface, a_x = 10 km, a_z = 0.5 km, and a set of constant heterogeneity level ε ranging from 0.0% to 2.5% with an interval of 0.5% (Garth and Rietbrock, 2014b), referred to as Fault_constant models. Once the slab model is set up, we simulate the seismic wavefield using a fully elastic GPU-based two-dimensional finite difference code (Li et al., 2014). With a grid spacing of 75 m and time steps of 0.001 s, the synthetic seismograms are accurate for frequencies up to 6 Hz.

Heterogeneity models	a_x **[km]**	a_z **[km]**	ε [%]	**Orientation**
Melt_constant0.0	10	0.5	0.0%	Slab-parallel
Melt_constant0.5	10	0.5	0.5%	Slab-parallel
Melt_constant1.0	10	0.5	1.0%	Slab-parallel
Melt_constant1.5	10	0.5	1.5%	Slab-parallel
Melt_constant2.0	10	0.5	2.0%	Slab-parallel
Melt_constant2.5	10	0.5	2.5%	Slab-parallel
Melt_basal	10	0.5	0.5%-2.5%	Slab-parallel
Fault_constant0.0	10	0.5	0.0%	25° to the slab surface
Fault_constant0.5	10	0.5	0.5%	25° to the slab surface
Fault_constant1.0	10	0.5	1.0%	25° to the slab surface
Fault_constant1.5	10	0.5	1.5%	25° to the slab surface
Fault_constant2.0	10	0.5	2.0%	25° to the slab surface
Fault_constant2.5	10	0.5	2.5%	25° to the slab surface

Table 3.1: Summary of the intra-slab heterogeneity model parameters.

3.4 Synthetic Test

With synthetic seismograms, we proceed to first validate the inter-source interferometry for small-scale intra-slab scatterers. Figure 3.2a shows the 0.2–2 Hz benchmark result for the Melt_constant1.0 model (ε = 1.0%) with earthquake pair D1–S1. The coda wave cross correlations of individual stations present coherent negative pulses at a constant arrival time (~54 s), suggesting a diffuse coda wavefield

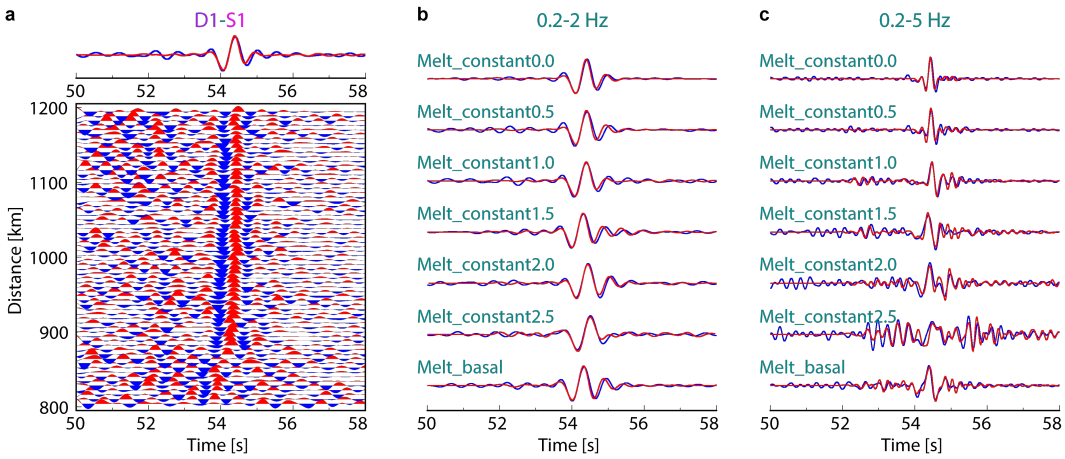

Figure 3.2: Inter-source interferometry synthetic benchmark for different intra-slab heterogeneity models. (a) 0.2–2 Hz inter-source interferometry benchmark result for the Melt_constant1.0 model (ε = 1.0%) with D1–S1 pair. The lower panel shows the cross-correlation record section. The upper panel is the waveform comparison between stacked cross correlation (blue) and theoretical strain response (red). (b) 0.2–2 Hz waveform comparison between the stacked cross correlations (blue) and theoretical strain responses (red) for Melt-type models with D1–S1 pair. (c) Similar to (b), but for 0.2–5 Hz.

in the stationary phase zone. The negative polarity of the 2 Hz cross correlations, as demonstrated from Shen and Zhan (2020), is the result of P wave reverberations within the low-velocity MOW. By averaging over all the cross correlations, the stacked interferometric waveform matches the directly simulated P wave strain seismograms from source D1 to virtual receiver S1 (Figure 3.2a, top panel). Following the same procedure, we also compare the stacked cross correlations to theoretical strain waveforms for other intra-slab heterogeneity models. As shown in Figure 3.2 and 3.3, the inter-source interferometry recovers the strain Green's function well at both 0.2-2 and 0.2-5 Hz in all scenarios, validating the applicability of inter-source interferometry for scattering slabs. Intriguingly, regardless of the type of intra-slab heterogeneity, the long period (0.2-2 Hz) interferometric waveforms do not differ substantially in waveform shape, confirming that the MOW (the controlling factor in this frequency band) is required to fit the inter-source interferometric observations in Japan (Figure 3.1b; Shen and Zhan, 2020). Moreover, the arrival time differences among all the 0.2-2 Hz interferometric signals are less than 0.2 s, which is within the earthquake location uncertainty. Hence, we solely focus on interpreting the waveform shape in this study. In contrast, the intra-slab heterogeneity level ε strongly affects the high-frequency (0.2-5 Hz) waveforms. For instance, weak scattering models (e.g., Melt_constant0.5) present simple pulses, whereas strong

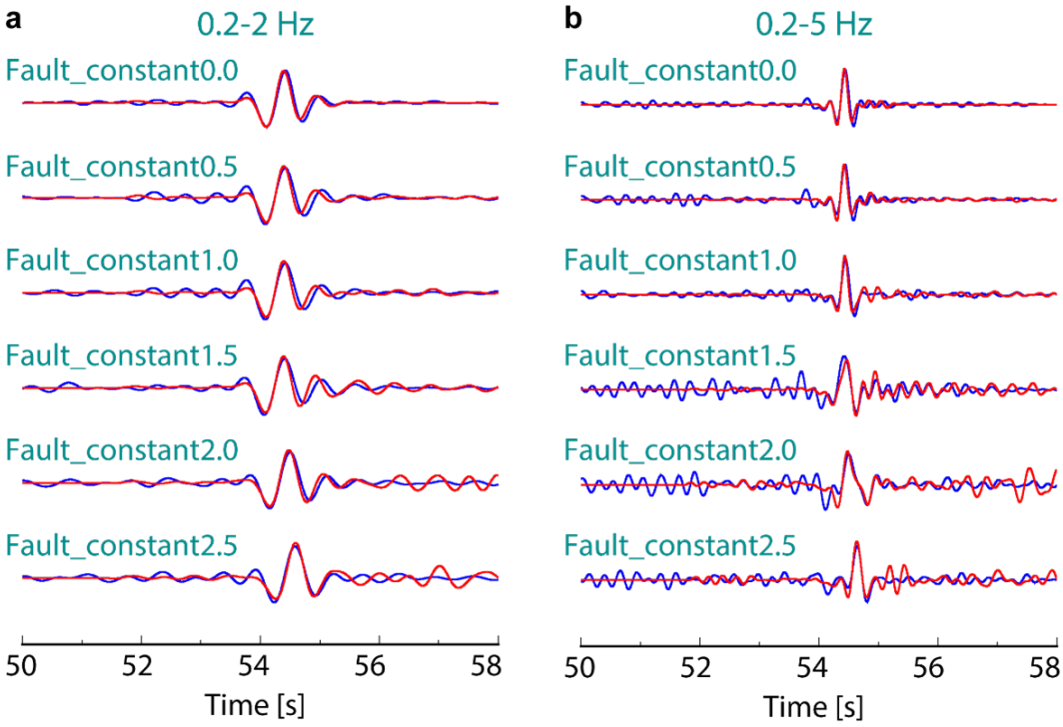

Figure 3.3: Inter-source interferometry benchmark results of Fault-type intra-slab heterogeneity models for (a). 0.2-2 Hz and (b). 0.2-5 Hz. The blue and red waveforms denote the stacked interferometric cross-correlations and synthetic strain waveforms, respectively. The heterogeneity type is indicated on the left side of waveforms.

scattering cases (e.g., Melt_constant2.5) exhibit lengthy wave trains (Figure 3.2c). Compared to Melt models, the Fault-type models show similar waveform variations, but less complicated for the heterogeneity level ε larger than 1.5% (Figure 3.3b). This is probably because the dipping configuration of laminate scatterers is less effective in trapping the high-frequency signals along the raypath from D1 to S1. Overall, the elongated small-scale heterogeneity acts as a frequency selective waveform modulator that weakly perturbs the low frequency, but efficiently channels the high-frequency energy, which is consistent with previous seismic observations (Furumura and Kennett, 2005). Therefore, the 5 Hz interferometric waveforms are crucial to constrain the small-scale intra-slab heterogeneity in MTZ.

3.5 Results

Having shown the sensitivity of inter-source interferometry to small-scale intra-slab scatterers, we compute the synthetic seismograms of all six deep earthquake pairs for different heterogeneity models (Figures 3.4 and 3.5) and compare them to the

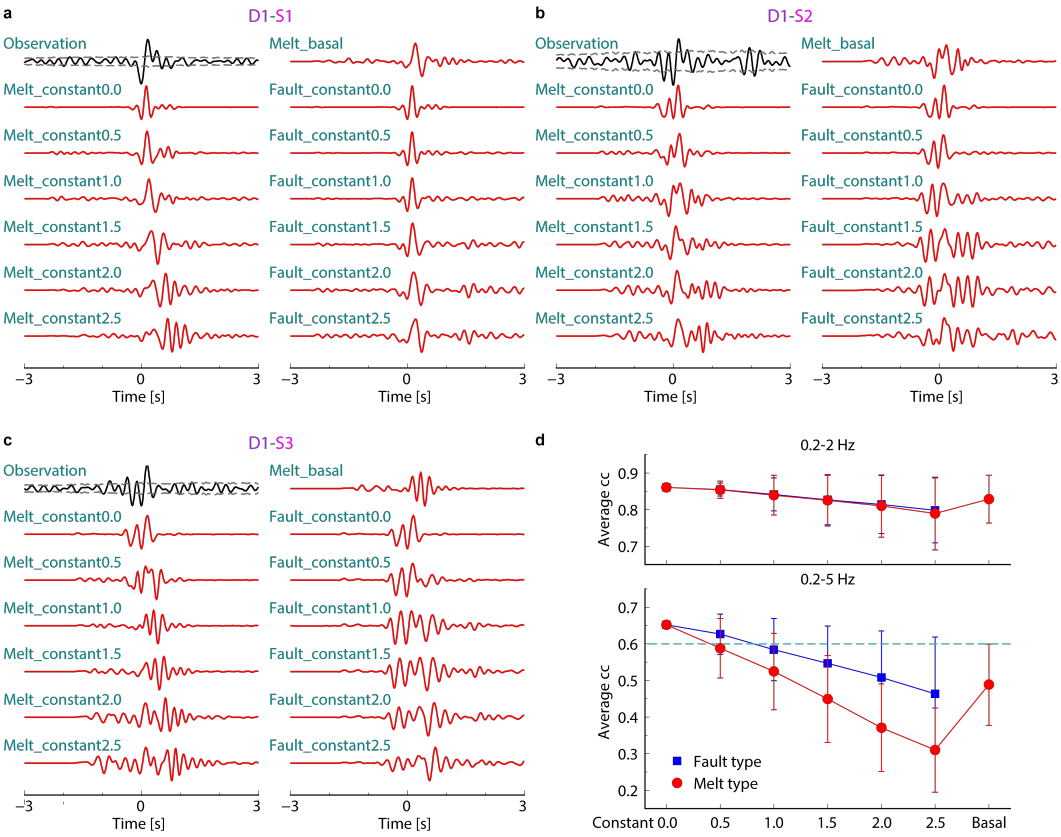

Figure 3.4: Data suggest weak intra-slab heterogeneity level below 410 km. 0.2–5 Hz waveform comparisons between inter-source interferometric observations (black) and synthetic strain waveforms (red) of Melt- and Fault-type heterogeneity models for (a) D1-S1 pair, (b) D1-S2 pair, and (c) D1-S3 pair in one realization. (d) Average cross-correlation coefficients (cc) of all six event pairs between observations and synthetics for Melt-type (red circles) and Fault-type (blue squares) heterogeneity models. The error bars indicate the 95% confidence interval, and the cyan dashed line denotes a cc threshold of 0.6.

interferometric waveforms obtained by Shen and Zhan (2020). Similarly to the benchmark tests above, the high-frequency strain waveform complexity of D1-S1 pair correlates with the scattering strength (ε) for the Melt-type models, but shows little dependencies on heterogeneity level of the Fault-type models (Figure 3.4a). Even so, the simple waveforms for strong Fault-type scattering cases contradict the observations with nearly opposite waveform shapes. As for the D1-S2 and D1-S3 pairs, both Melt- and Fault-type models with large ε introduce lengthy coda or secondary arrivals at 5 Hz, failing to capture the interferometric observations which exhibit "W-shape" waveforms (two negative wiggles preceding a positive one; Figures 3.4b and 3.4c). Note that the Melt_constant1.0/1.5 and Melt_basal models yield better fit to the D1–S3 observation than the Melt_constant0.5 case,

but perform worse for D1-S1/S2 and D2-S1 pairs (Figures 3.4 and 3.5). Thus, in general, increasing the heterogeneity level reduces the overall similarity between interferometric observations and synthetic seismograms.

In fact, because of the stochastic nature of small-scale scatterers, the 5 Hz waveforms can vary substantially in a set of realizations of the same intra-slab heterogeneity types with $\varepsilon > 1.5\%$ (Figure 3.6). To statistically quantify the effect of random media on the waveform fitting, we conduct 100 realizations for each intra-slab heterogeneity type. In each realization, we cross correlate the synthetics with observed interferometric waveforms in a 6-s time window and average the six cross-correlation coefficients (cc) by signal to noise ratios to represent the similarity between observations and simulations. For each intra-slab heterogeneity type, the

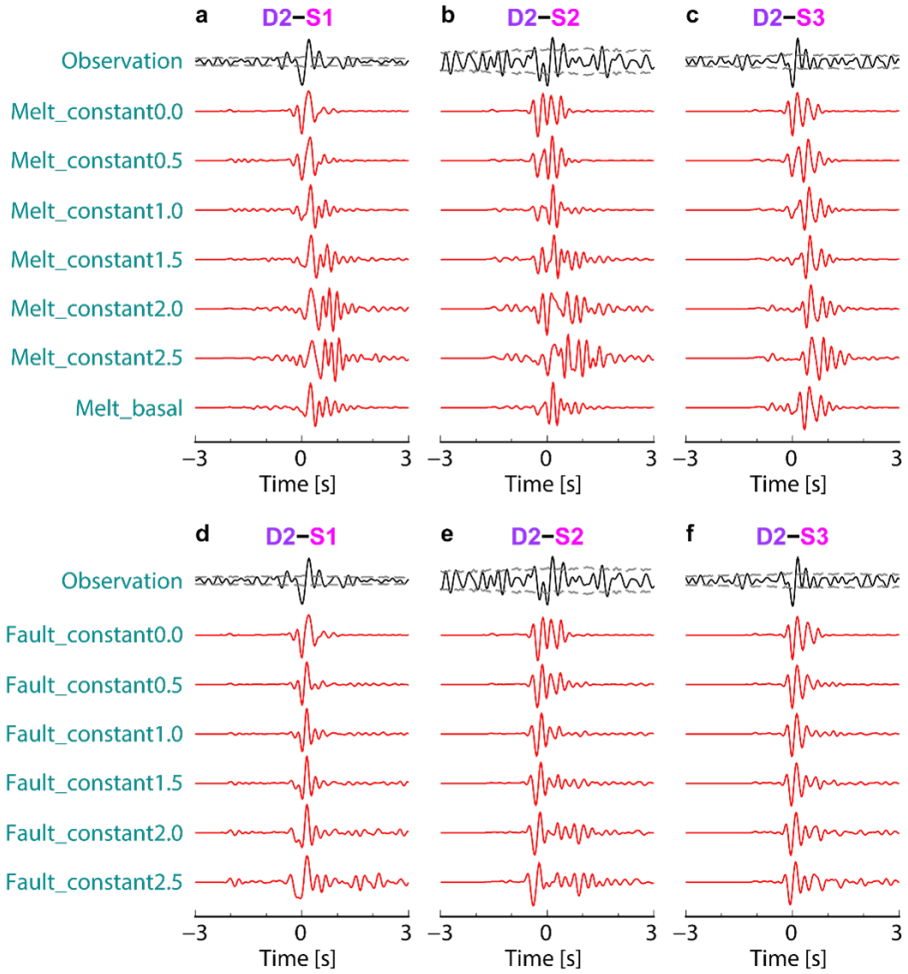

Figure 3.5: 0.2-5 Hz waveform comparisons between inter-source interferometric observations (black) and synthetic strain waveforms (red) of (a~c). Melt- and (d~f). Fault-type models for D2-S1/S2/S3 deep earthquake pairs in one realization.

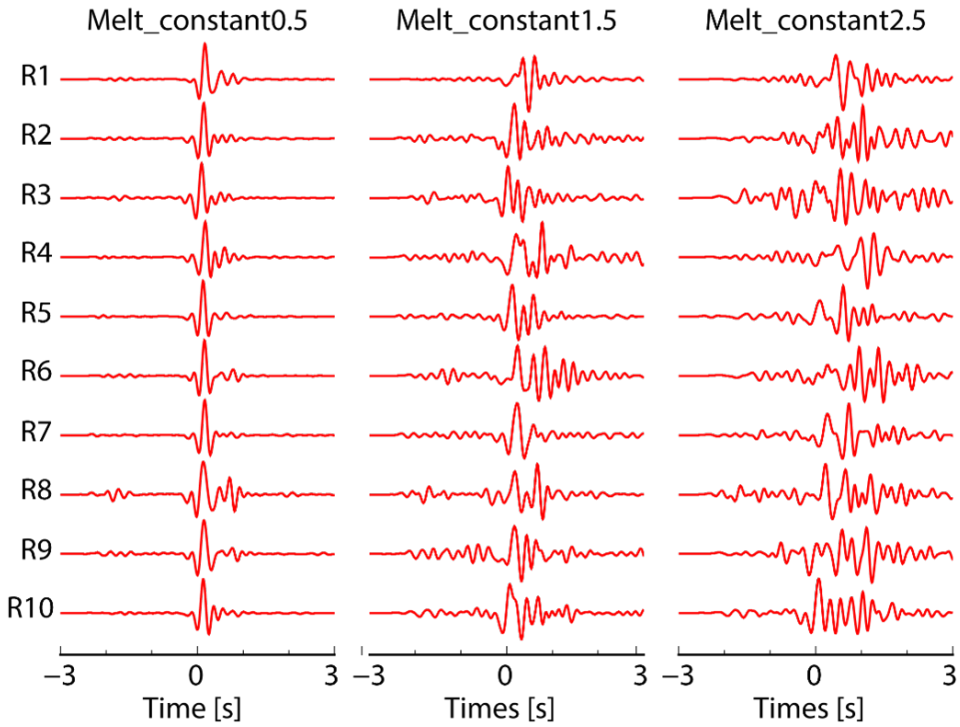

Figure 3.6: 5 Hz synthetic strain waveform comparisons of 10 realizations of three Melt-type models for the D1-S1 event pair.

distribution of averaged cc can be approximated by a Gaussian distribution (Figure 3.7). As shown in Figure 3.4d, the mean value of averaged cc slightly drops from 0.88 (ε = 0.0%) to 0.80 (ε = 2.5%) at 0.2–2 Hz for both Melt- and Fault-type models. Whereas the averaged cc for 0.2–5 Hz starts at a lower value of 0.65 possibly due to elevated observational noise level and decreases dramatically to 0.46 and 0.30 for the Fault_constant2.5 and Melt_constant2.5 models, respectively. The performance of the Melt_basal case falls between the Melt_constant1.0 and Melt_constant1.5. Due to the slab-parallel raypaths of the six earthquake pairs (Figure 3.1), the 5 Hz waveforms are more sensitive to the Melt-type models than the Fault-type models. By defining a cc threshold value of 0.6 that corresponds to a 10% fit reduction from the non-scattering model, we assess the probability of achieving the proper waveform fit to observations for each intra-slab heterogeneity type. The resulting probability reduces abruptly to less than 10% when ε is larger than 1.0% and 1.5% for the Melt- and Fault-type, respectively (Figure 3.8), rejecting the strong scattering model at depth. Moreover, the probability of Melt_constant0.5 and Fault_constant1.0 models does not exceed 30% (Figure 3.8), thus the upper bound of the intra-slab heterogeneity level below 410 km is probably less than 0.5% and 1.0% for the Melt- and Fault-type models, respectively.

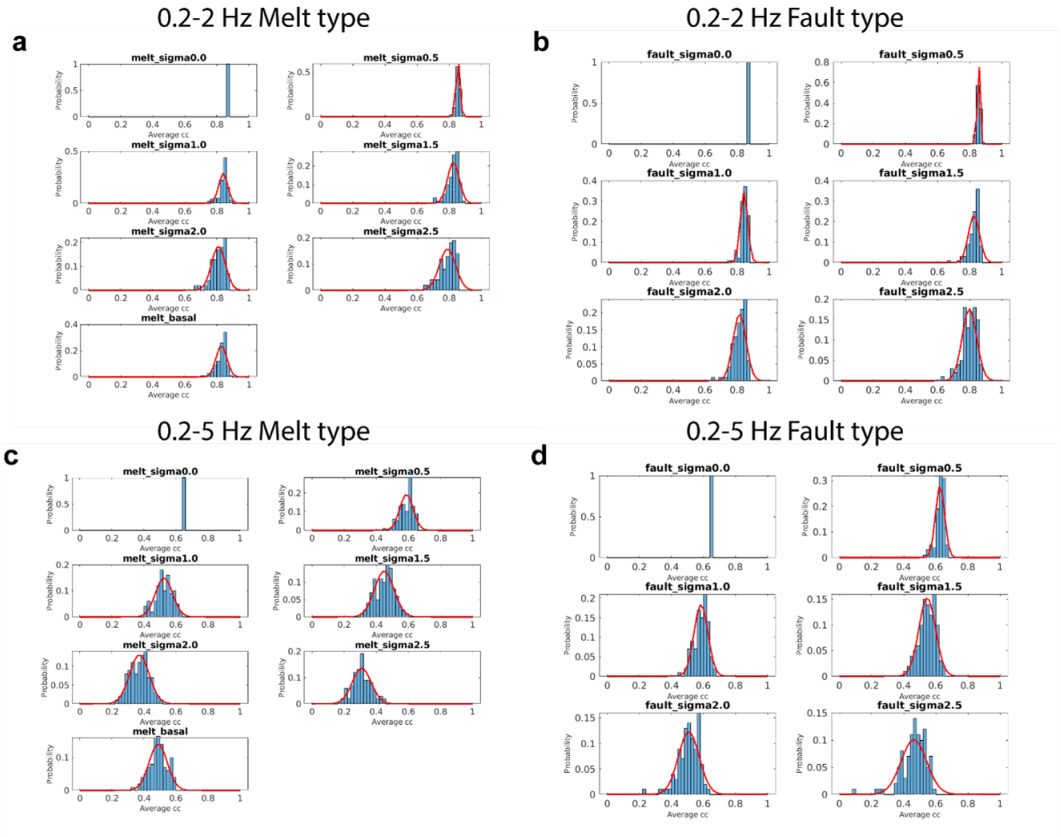

Figure 3.7: Distribution of 100 averaged cross-correlation coefficients for Melt- and Fault-type models. The red lines donate the approximated Gaussian distribution.

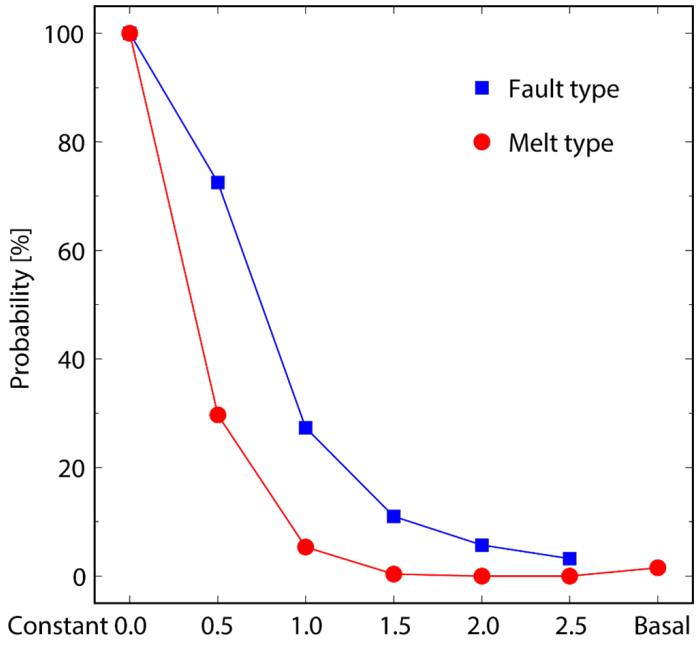

Figure 3.8: Probability of averaged cross-correlation coefficients above threshold (0.6) for both Melt- (red circles) and Fault-type (blue squares) models.

3.6 Discussion

Reduced intra-slab scattering at depth

In this study, we are restricted to 2D simulations because of the computational cost for 3D. Generally, 2D simulation of seismic wave propagation shows different features of the 3D case due to differences in Green's function and geometrical spreading. Nevertheless, the seismic wavefield in our 2D simulations is mostly trapped waves within the MOW and scatterers. Previous studies of high-frequency waves show that differences in effects of trapping are not so significant between 2D and 3D simulations (Furumura and Kennett, 2005; Garth and Rietbrock, 2014a; Takemura et al., 2015). Therefore, our 2D slab model can represent the general feature of intra-slab scatterers within the updip dimension. Still, without comprehensive 3D simulations, we cannot fully understand the character of intra-slab scatterers, such as the presence of strong azimuthal-dependent scatterers (Furumura and Kennett, 2021).

Note that the frequency contents of our interferometric observations are narrow-banded due to the small magnitudes of deep earthquakes. Nonetheless, increasing the small-scale intra-slab heterogeneity level raises the high-frequency strain waveform complexity. For simultaneously fitting the six inter-source interferometric observations which all present distinct signals, the intra-slab scattering level (ε) is preferred to be less than 1.0%. To further reinforce our argument, we investigate the potential influence of MOW geometry as defined by different slab thermal structures. Two cases are examined here: one with slightly thinner MOW produces reasonable overall waveform fits without scatterers, while the other case with thicker MOW presents similar waveform fit at 0.2–2 Hz, but poorly fits the 0.2–5 Hz observations without scatterers (Figure 3.9). Similarly to Figure 3.4d, the cross-correlation coefficients for both scenarios slightly drop at 0.2–2 Hz, but dramatically decrease with the heterogeneity level at 0.2–5 Hz, confirming the robustness of the previously proposed MOW model by Shen and Zhan (2020) and a weakly scattering slab in the MTZ (Figure 3.9).

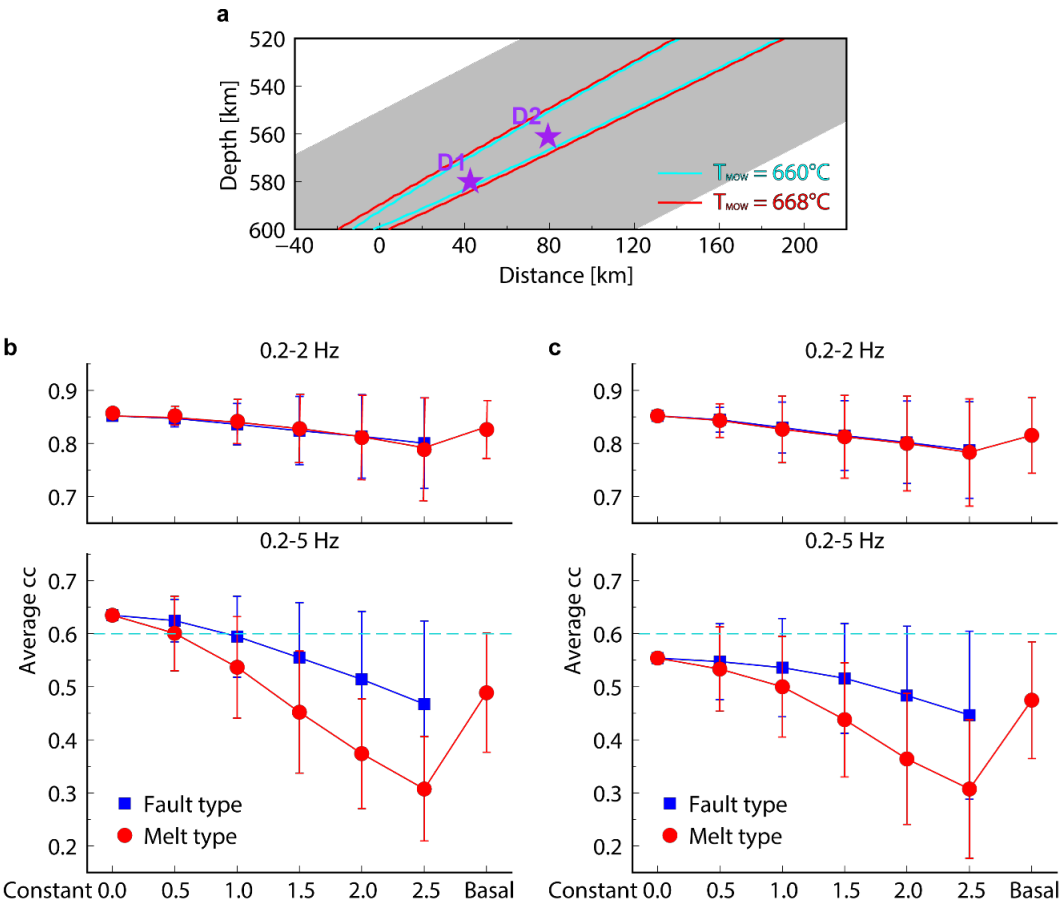

Figure 3.9: MOW geometry effect on the data fit. (a). Depth profile of two MOW geometries described by the temperature contour T_{mow} = 660°C and T_{mow} = 668°C. The grey region represents the subducting slab. (b). Average cross-correlation coefficient plot for the T_{mow} = 660°C case. The Melt- and Fault-type models are denoted as blue squares and red circles, respectively. The top and bottom panels are for 0.2-2 Hz and 0.2-5 Hz, respectively. The error bars indicate the 95% confidence interval, and the cyan dashed line denotes a cc threshold of 0.6. (c). Similar to (b), but for the T_{mow} = 668°C case.

On the other hand, previous studies have suggested a laminar intra-slab heterogeneity with strong scattering (ε = 2.5%) at intermediate depth range for the Japan subduction zone by fitting long-duration coda (Furumura and Kennett, 2005; Garth and Rietbrock, 2014b). So it is also crucial to explain the surface waveform observations with our reduced intra-slab heterogeneity below 410-km. We compared our synthetic waveforms for cases with different intra-slab heterogeneity level below 410-km to the surface observation of a near trench Hi-net station TYOH (Figure 3.10). Due to the small magnitude of our deep earthquake D1 (M4.8), we band-passed the vertical component of TYOH station from 1 to 10 Hz. Our initial model

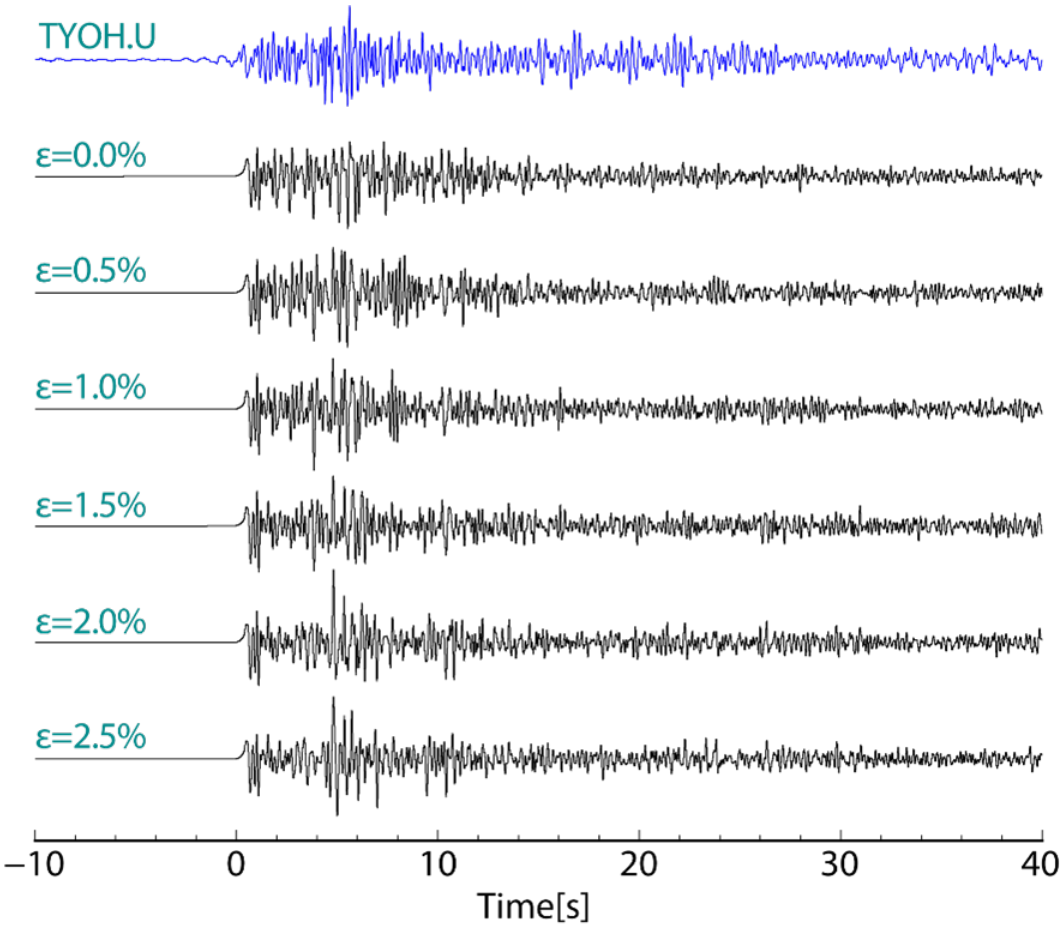

Figure 3.10: Waveform comparison between surface observations of station TYOH (blue line) and scenarios with different intra-slab heterogeneity levels below 410-km for the deep event D1. The station TYOH is located near the trench and its vertical component is bandpass filtered between 1 to 10 Hz. The intra-slab heterogeneity level below 410 km is indicated at the left side of each seismogram. Our background model includes a high-velocity slab, a low-velocity MOW from (Shen and Zhan, 2020) and shallow intra-slab scatterers (<350 km) from Furumura and Kennett (2005)

includes a high-velocity slab, a low-velocity MOW from Shen and Zhan (2020) and the intra-slab scatterers above 350 km from Furumura and Kennett (2005). As shown in Figure 3.10, we found that (i) our preferred heterogeneity model (cases of $\varepsilon \leq 1.0\%$) can also reproduce the surface observation with similar coda strength, (ii) the synthetics from deep earthquake D1 present similar coda durations and body-wave dispersion for different intra-slab scattering levels, suggesting that the surface observations from deep events are predominated by shallower heterogeneities and the low-velocity MOW. The latter conclusion is consistent with Furumura et al. (2016) which suggests that MOW is a major factor below 410-km. Meanwhile, even

though the contribution of deep intra-slab scatterers to coda waves is difficult to be quantified by modeling the surface seismograms, the coda differences between two deep earthquakes (with one below 410-km and the other shallower) extracted by our inter-source interferometry method can highlight the deeper slab structure. Therefore, we propose that the elongated intra-slab heterogeneity decreases from 2.5% to <1.0% in the MTZ beneath the Japan Sea (Figure 3.11).

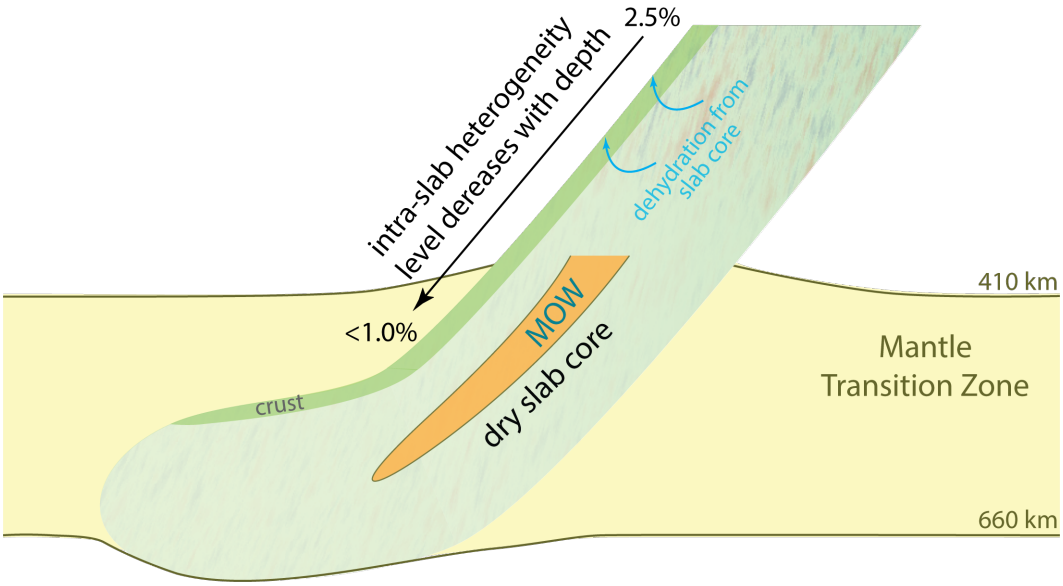

Figure 3.11: Cartoon of intra-slab heterogeneity level with depth beneath the Japan Sea. The strong scattering of 2.5% at intermediate depth and the MOW are suggested by Furumura and Kennett (2005) and Shen and Zhan (2020), respectively. If a MOW is only stabilized by an anhydrous phase assemblage (Du Frane et al., 2013), then the decrease of scattering strength toward greater depth (this study) in combination with the above-mentioned constraints indicates that we are capturing processes associated with slab dehydration.

Interpretation for the origin of intra-slab scatterers

At face value, the reduced heterogeneity level at depth (i.e., decreased seismic visibility) may appear challenging to interpret. However, as discussed above, there is strong evidence for the presence of a MOW at these depths and observations of stronger scattering at shallower depths. Thus, we have a depth trend for which we can attempt to understand. That is, there is a decreasing trend in seismic scatterers with increasing depth to the MTZ, and this trend is resolved for the lithospheric section (core) of the slab. The presence of low-velocity anomalies in the crustal portion of the slab (e.g., hydrous phases) always generates positive polarities of interferometric waveforms at 0.2–2 Hz, contradicting our observed negative polarities (Figure 3.12).

This reinforces that our observations are dominated by the seismic structures in the slab core and have little sensitivity to the slab crust. Therefore, we cannot rule out the possibility of slab crustal complexity.

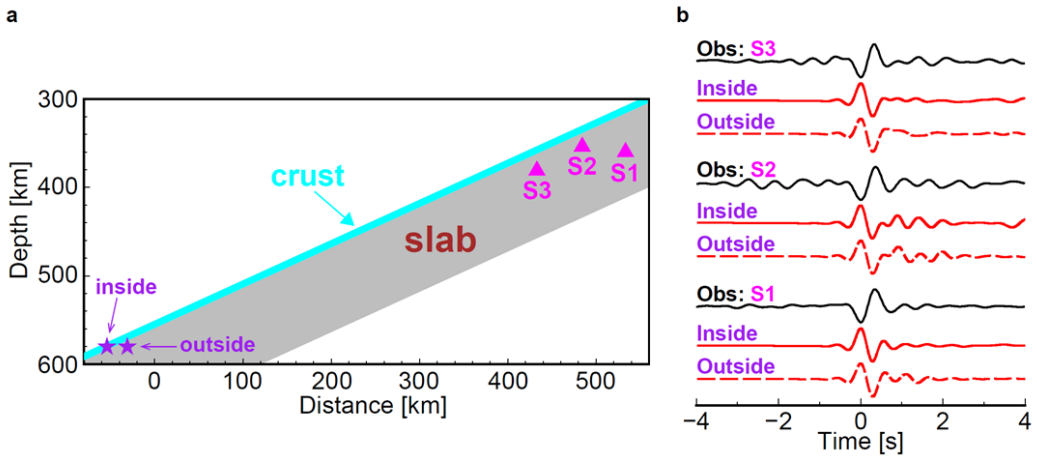

Figure 3.12: Anomalous oceanic crust structure always produces positive polarities (vs. negative polarity for 0.2-2 Hz inter-source interferometry observations) regardless of the deep earthquake locations. (a). Slab profile and source-receiver configuration. The grey and cyan area represent the slab and crust, respectively. The crust is 8 km thick with 8% reduction in velocity and density. Synthetic waveforms at three virtual receivers (magenta triangles) are calculated for cases of deep earthquakes (purple stars) inside and outside the crust. (b). 0.2-2 Hz waveform comparison between observations (black) and synthetics (red). The red solid lines and red dashed lines indicate synthetics for cases of deep earthquake inside and outside the crust, respectively.

Melt bands

It has been suggested that the presence of preserved (and potentially re-activated) melt-bands could explain the strong P wave coda at intermediate depths (Furumura and Kennett, 2008; Sun et al., 2014). To explain the current set of observations here, one would infer that these preserved melt bands would become seismically invisible in the MTZ. Although this is a reasonable hypothesis, the existence and preservation of such melt-rich bands or channels at the kilometer scale along subducting slabs require corroborating observations, such as observations at shallower depths and co-located strong intra-slab anisotropy, as the petrological evidence of melt band lamination have only been derived from experimental and modeling work and are mostly at the micrometer scale (Katz et al., 2006).

Hydrated faults

At the Japan trench, plate bending stress creates pervasive fractures and faults extending to the oceanic lithosphere (Fujie et al., 2016; Fujie et al., 2018; Obana et al., 2019), promoting water penetration in the deeper slab and mantle serpentinization prior to subduction (Faccenda et al., 2009; Iyer et al., 2012). The intra-slab seismic scatterers at intermediate depths along this slab (Furumura and Kennett, 2005) could therefore be explained by the short-scale serpentinized faults (Garth and Rietbrock, 2014b). As the slab subducts, the elevated pressure and temperature lead to a series of breakdown reactions of hydrous minerals, expelling aqueous fluid to refertilize the mantle wedge (Van Keken et al., 2011). The water released from serpentinite breakdown can progressively percolate upward along an intra-slab layer characterized by the tectonic stress gradient (Faccenda et al., 2012). For cold slabs like the Japan subduction zone, the serpentinites could transform to hydrous dense magnesium silicates (HDMS) below the subarc depth (Chen et al., 2019; Faccenda, 2014). Given the existence of a MOW (Shen and Zhan, 2020) which requires an extremely dry slab core (<75 wt ppm) (Du Frane et al., 2013; Kawakatsu and Yoshioka, 2011) and the lack of intra-slab P wave coda in the MTZ (this study), the dehydration process of the slab core is almost complete by 410 km. This would imply that HDMS such as clinohumite could possibly transport "water" into MTZ only along the slab top (Stalder and Ulmer, 2001). As mentioned above, we cannot rule out the presence of a hydrous-rich slab crust. Rather our observations shed light on the dehydration process of slab cores that could lead to (re-)hydration of the slab crust and formation of dense oxyhydroxide phases (e.g., Buchen et al., 2021; Karato, 2006; Ohira et al., 2019; Ohtani, 2020).

3.7 Conclusion

In this study, we applied inter-source interferometry method to constrain the small-scale intra-slab scatterers below 410 km beneath the Japan Sea. By conducting numerical simulations for various intra-slab heterogeneity scenarios, we validated the robustness of previously proposed MOW model by Shen and Zhan (2020) and found that strong scattering models tend to complicate the high-frequency waveforms, leading to a worse fit to the interferometric observations. We quantified the intra-slab heterogeneity level to be less than 1.0% below 410 km. Combining with previous observations of strong scattering (~2.5%) at intermediate depths, we conclude that the intra-slab heterogeneity weakens as the slab subducts. Given the pervasive faults extending to the oceanic lithosphere at the Japan trench and

the existence of a MOW in the MTZ, we suggest that the small-scale scatterers are caused by hydration processes in the outer rise. The observed weakening of scattering strength reveals that the dehydration process of the slab core must be complete by 410 km and could possibly lead to (re-)hydration of the slab crust and formation of dense oxyhydroxide phases.

3.8 Acknowledgement

The authors are grateful to Mike Gurnis, Rob Clayton, and two anonymous reviewers for discussions and suggestions. The authors are grateful to the National Science Foundation's (NSF) Collaborative Study of Earth's Deep Interior under EAR-2009935 for support of this work. Seismic data are collected from Hi-net (www.hinet.bosai.go.jp) and F-net (www.fnet.bosai.go.jp). The earthquake catalog and focal mechanisms are downloaded from ISC-EHB distributed by the International Seismological Centre (http://www.isc.ac.uk/isc-ehb/) and National Research Institute for Earth Science and Disaster Resilience (NIED; https://www.fnet.bosai.go.jp/event/search.php?LANG=en).

References

Abers, G. A. (2000). Hydrated subducted crust at 100–250 km depth. In: *Earth and Planetary Science Letters* 176.3, pp. 323–330. ISSN: 0012-821X. DOI: 10.1016/S0012-821X(00)00007-8.

Abers, G. A. et al. (2003). The wet Nicaraguan slab. In: *Geophysical Research Letters* 30.2. ISSN: 1944-8007. DOI: 10.1029/2002GL015649.

Buchen, J. et al. (2021). Vibrational anisotropy of δ-(Al,Fe)OOH single crystals as probed by nuclear resonant inelastic X-ray scattering. In: *European Journal of Mineralogy* 33.4. Publisher: Copernicus GmbH, pp. 485–502. ISSN: 0935-1221. DOI: 10.5194/ejm-33-485-2021.

Cammarano, F. et al. (2003). Inferring upper-mantle temperatures from seismic velocities. In: *Physics of the Earth and Planetary Interiors* 138.3. Publisher: Elsevier, pp. 197–222. DOI: 10.1016/S0031-9201(03)00156-0.

Campillo, M. and A. Paul (2003). Long-range correlations in the diffuse seismic coda. In: *Science* 299.5606. Publisher: American Association for the Advancement of Science, pp. 547–549. DOI: 10.1126/science.1078551.

Chen, M. et al. (2007). Waveform modeling of the slab beneath Japan. In: *Journal of Geophysical Research: Solid Earth* 112 (B2). ISSN: 2156-2202. DOI: 10.1029/2006JB004394.

Chen, M. et al. (2019). Genesis of Intermediate-Depth and Deep Intraslab Earthquakes beneath Japan Constrained by Seismic Tomography, Seismicity, and Thermal Modeling. In: *Geophysical Research Letters* 46.4, pp. 2025–2036. ISSN: 1944-8007. DOI: 10.1029/2018GL080025.

Curtis, A. et al. (2009). Virtual seismometers in the subsurface of the Earth from seismic interferometry. In: *Nature Geoscience* 2.10. Publisher: Nature Publishing Group, pp. 700–704. DOI: 10.1038/ngeo615.

Du Frane, W. L. et al. (2013). Ringwoodite growth rates from olivine with 75 ppmw H_2O: Metastable olivine must be nearly anhydrous to exist in the mantle transition zone. In: *Physics of the Earth and Planetary Interiors* 219. Publisher: Elsevier, pp. 1–10. DOI: 10.1016/j.pepi.2013.04.001.

Eulenfeld, T. (2020). Toward source region tomography with intersource interferometry: Shear wave velocity from 2018 West Bohemia swarm earthquakes. In: *Journal of Geophysical Research: Solid Earth* 125.9, e2020JB019931. ISSN: 2169-9356. DOI: 10.1029/2020JB019931.

Faccenda, M. (2014). Water in the slab: A trilogy. In: *Tectonophysics* 614, pp. 1–30. ISSN: 0040-1951. DOI: 10.1016/j.tecto.2013.12.020.

Faccenda, M. et al. (2009). Deep slab hydration induced by bending-related variations in tectonic pressure. In: *Nature Geoscience* 2.11, pp. 790–793. ISSN: 1752-0908. DOI: 10.1038/ngeo656.

Faccenda, M. et al. (2012). Fluid flow during slab unbending and dehydration: Implications for intermediate-depth seismicity, slab weakening and deep water recycling. In: *Geochemistry, Geophysics, Geosystems* 13.1. ISSN: 1525-2027. DOI: 10.1029/2011GC003860.

Fujie, G. et al. (2016). Along-trench variations in the seismic structure of the incoming Pacific plate at the outer rise of the northern Japan Trench. In: *Geophysical Research Letters* 43.2, pp. 666–673. ISSN: 1944-8007. DOI: 10.1002/2015GL067363.

Fujie, G. et al. (2018). Controlling factor of incoming plate hydration at the northwestern Pacific margin. In: *Nature Communications* 9.1, p. 3844. ISSN: 2041-1723. DOI: 10.1038/s41467-018-06320-z.

Fukao, Y. and M. Obayashi (2013). Subducted slabs stagnant above, penetrating through, and trapped below the 660 km discontinuity. In: *Journal of Geophysical Research: Solid Earth* 118.11, pp. 5920–5938. ISSN: 2169-9356. DOI: 10.1002/2013JB010466.

Furumura, T. and B. L. N. Kennett (2005). Subduction zone guided waves and the heterogeneity structure of the subducted plate: Intensity anomalies in northern Japan. In: *Journal of Geophysical Research: Solid Earth* 110 (B10). Publisher: Wiley Online Library. DOI: 10.1029/2004JB003486.

Furumura, T. and B. L. N. Kennett (2008). Chapter 7 A Scattering Waveguide in the Heterogeneous Subducting Plate. In: *Advances in Geophysics*. Vol. 50. Earth Heterogeneity and Scattering Effects on Seismic Waves. Elsevier, pp. 195–217. DOI: 10.1016/S0065-2687(08)00007-1.

Furumura, T. and B. L. N. Kennett (2021). Azimuthal variation of lithospheric heterogeneity in the Northwest Pacific inferred from Po/So propagation characteristics and anomalously large ground motion of deep in-slab earthquakes. In: *Journal of Geophysical Research: Solid Earth* 126.5, e2021JB021717. ISSN: 2169-9356. DOI: 10.1029/2021JB021717.

Furumura, T. et al. (2016). Enhanced waveguide effect for deep-focus earthquakes in the subducting Pacific slab produced by a metastable olivine wedge. In: *Journal of Geophysical Research: Solid Earth* 121.9. Publisher: Wiley Online Library, pp. 6779–6796. DOI: 10.1002/2016JB013300.

Garth, T. and A. Rietbrock (2014a). Downdip velocity changes in subducted oceanic crust beneath Northern Japan—insights from guided waves. In: *Geophysical Journal International* 198.3, pp. 1342–1358. ISSN: 0956-540X. DOI: 10.1093/gji/ggu206.

Garth, T. and A. Rietbrock (2014b). Order of magnitude increase in subducted H_2O due to hydrated normal faults within the Wadati-Benioff zone. In: *Geology* 42.3, pp. 207–210. ISSN: 0091-7613. DOI: 10.1130/G34730.1.

Garth, T. and A. Rietbrock (2017). Constraining the hydration of the subducting Nazca plate beneath Northern Chile using subduction zone guided waves. In: *Earth and Planetary Science Letters* 474, pp. 237–247. ISSN: 0012-821X. DOI: 10.1016/j.epsl.2017.06.041.

Goes, S. et al. (2017). Subduction-transition zone interaction: A review. In: *Geosphere* 13.3, pp. 644–664. ISSN: 1553-040X. DOI: 10.1130/GES01476.1.

Hayes, G. P. et al. (2018). Slab2, a comprehensive subduction zone geometry model. In: *Science* 362.6410. Publisher: American Association for the Advancement of Science, pp. 58–61. DOI: 10.1126/science.aat4723.

Iidaka, T. and D. Suetsugu (1992). Seismological evidence for metastable olivine inside a subducting slab. In: *Nature* 356.6370. Publisher: Nature Publishing Group, pp. 593–595. DOI: 10.1038/356593a0.

Iyer, K. et al. (2012). Controls of faulting and reaction kinetics on serpentinization and double Benioff zones. In: *Geochemistry, Geophysics, Geosystems* 13.9. ISSN: 1525-2027. DOI: 10.1029/2012GC004304.

Karato, S.-i. (2006). Remote sensing of hydrogen in Earth's mantle. In: *Reviews in Mineralogy and Geochemistry* 62.1, pp. 343–375. ISSN: 1529-6466. DOI: 10.2138/rmg.2006.62.15.

Katz, R. F. et al. (2006). The dynamics of melt and shear localization in partially molten aggregates. In: *Nature* 442.7103. Bandiera_abtest: a Cg_type: Nature Research Journals Number: 7103 Primary_atype: Research Publisher: Nature Publishing Group, pp. 676–679. ISSN: 1476-4687. DOI: 10.1038/nature05039.

Kawakatsu, H. and S. Yoshioka (2011). Metastable olivine wedge and deep dry cold slab beneath southwest Japan. In: *Earth and Planetary Science Letters* 303.1. Publisher: Elsevier, pp. 1–10. DOI: 10.1016/j.epsl.2011.01.008.

Kennett, B. L. N. and T. Furumura (2015). Toward the reconciliation of seismological and petrological perspectives on oceanic lithosphere heterogeneity. In: *Geochemistry, Geophysics, Geosystems* 16.9, pp. 3129–3141. ISSN: 1525-2027. DOI: 10.1002/2015GC006017.

Li, C. et al. (2008). A new global model for P wave speed variations in Earth's mantle. In: *Geochemistry, Geophysics, Geosystems* 9.5. ISSN: 1525-2027. DOI: 10.1029/2007GC001806.

Li, D. et al. (2014). Global synthetic seismograms using a 2-D finite-difference method. In: *Geophysical Journal International* 197.2, pp. 1166–1183. ISSN: 0956-540X. DOI: 10.1093/gji/ggu050.

Lu, C. et al. (2019). TX2019slab: A new P and S tomography model incorporating subducting slabs. In: *Journal of Geophysical Research: Solid Earth* 124.11, pp. 11549–11567. ISSN: 2169-9356. DOI: 10.1029/2019JB017448.

Moresi, L. et al. (2007). Computational approaches to studying non-linear dynamics of the crust and mantle. In: *Physics of the Earth and Planetary Interiors* 163.1. Publisher: Elsevier, pp. 69–82. DOI: 10.1016/j.pepi.2007.06.009.

Obana, K. et al. (2019). Seismic velocity structure and its implications for oceanic mantle hydration in the trench–outer rise of the Japan Trench. In: *Geophysical Journal International* 217.3, pp. 1629–1642. ISSN: 0956-540X. DOI: 10.1093/gji/ggz099.

Ohira, I. et al. (2019). Compressional behavior and spin state of δ-(Al,Fe)OOH at high pressures. In: *American Mineralogist* 104.9, pp. 1273–1284. ISSN: 0003-004X. DOI: 10.2138/am-2019-6913.

Ohtani, E. (2020). The role of water in Earth's mantle. In: *National Science Review* 7.1, pp. 224–232. ISSN: 2095-5138. DOI: 10.1093/nsr/nwz071.

Omori, S. et al. (2004). Dehydration and earthquakes in the subducting slab: Empirical link in intermediate and deep seismic zones. In: *Physics of the Earth and Planetary Interiors*. Plumes and Superplumes 146.1, pp. 297–311. ISSN: 0031-9201. DOI: 10.1016/j.pepi.2003.08.014.

Ritsema, J. et al. (2011). S40RTS: a degree-40 shear-velocity model for the mantle from new Rayleigh wave dispersion, teleseismic traveltime and normal-mode splitting function measurements. In: *Geophysical Journal International* 184.3, pp. 1223–1236. ISSN: 0956-540X. DOI: 10.1111/j.1365-246X.2010.04884.x.

Sato, H. et al. (2012). *Seismic wave propagation and scattering in the heterogeneous earth*. Springer Science & Business Media. ISBN: 978-3-642-44318-3. DOI: 10.1007/978-3-642-23029-5.

Savage, B. (2012). Seismic constraints on the water flux delivered to the deep Earth by subduction. In: *Geology* 40.3, pp. 235–238. ISSN: 0091-7613. DOI: 10.1130/G32499.1.

Sdrolias, M. and R. D. Müller (2006). Controls on back-arc basin formation. In: *Geochemistry, Geophysics, Geosystems* 7.4. Publisher: Wiley Online Library. DOI: 10.1029/2005GC001090.

Shapiro, N. M. et al. (2005). High-resolution surface-wave tomography from ambient seismic noise. In: *Science*. Publisher: American Association for the Advancement of Science. DOI: 10.1126/science.1108339.

Shen, Z. and Z. Zhan (2020). Metastable olivine wedge beneath the Japan Sea imaged by seismic interferometry. In: *Geophysical Research Letters* 47.6, e2019GL085665. ISSN: 1944-8007. DOI: 10.1029/2019GL085665.

Simmons, N. A. et al. (2012). LLNL-G3Dv3: Global P wave tomography model for improved regional and teleseismic travel time prediction. In: *Journal of Geophysical Research: Solid Earth* 117 (B10). ISSN: 2156-2202. DOI: 10.1029/2012JB009525.

Stalder, R. and P. Ulmer (2001). Phase relations of a serpentine composition between 5 and 14 GPa: Significance of clinohumite and phase E as water carriers into the transition zone. In: *Contributions to Mineralogy and Petrology* 140.6, pp. 670–679. ISSN: 1432-0967. DOI: 10.1007/s004100000208.

Sun, D. et al. (2014). High frequency seismic waves and slab structures beneath Italy. In: *Earth and Planetary Science Letters* 391, pp. 212–223. ISSN: 0012-821X. DOI: 10.1016/j.epsl.2014.01.034.

Takemura, S. et al. (2015). Velocity increase in the uppermost oceanic crust of subducting Philippine Sea plate beneath the Kanto region due to dehydration inferred from high-frequency trapped P waves. In: *Earth, Planets and Space* 67.1. Publisher: SpringerOpen, pp. 1–14. DOI: 10.1186/s40623-015-0210-6.

Tonegawa, T. and K. Nishida (2010). Inter-source body wave propagations derived from seismic interferometry. In: *Geophysical Journal International* 183.2. Publisher: Blackwell Publishing Ltd Oxford, UK, pp. 861–868. DOI: 10.1111/j.1365-246X.2010.04753.x.

Van Keken, P. E. et al. (2011). Subduction factory: 4. Depth-dependent flux of H_2O from subducting slabs worldwide. In: *Journal of Geophysical Research: Solid Earth* 116 (B1). ISSN: 2156-2202. DOI: 10.1029/2010JB007922.

Zhan, Z. (2020). Mechanisms and implications of deep earthquakes. In: *Annual Review of Earth and Planetary Sciences* 48.1, pp. 147–174. DOI: 10.1146/annurev-earth-053018-060314.

Zhan, Z. et al. (2014). Imaging subducted slab structure beneath the Sea of Okhotsk with teleseismic waveforms. In: *Physics of the Earth and Planetary Interiors* 232. Publisher: Elsevier, pp. 30–35. DOI: 10.1016/j.pepi.2014.03.008.

Zhao, D. (2004). Global tomographic images of mantle plumes and subducting slabs: insight into deep Earth dynamics. In: *Physics of the Earth and Planetary Interiors*. Plumes and Superplumes 146.1, pp. 3–34. ISSN: 0031-9201. DOI: 10.1016/j.pepi.2003.07.032.

Chapter 4

ESTIMATING THE SLAB SEISMIC VELOCITY PERTURBATION USING A SLAB OPERATOR METHOD

4.1 Abstract

Subducted slab temperature provides fundamental constraints on petrological and mechanical processes. To infer the thermal state of subducting slab, an accurate seismic velocity estimation is a prerequisite. However, traveltime based tomography ubiquitously underestimates the absolute amplitude of slab velocity, and deterministic waveform modeling has better sensitivity, but involves great effort. Given that high-velocity slabs act similarly as an attenuation operator broadening seismograms, we develop a slab operator method using teleseismic waveforms from subduction zone earthquakes. With 2D synthetic tests, we demonstrate that the slab operator method is capable of measuring the slab velocity perturbation through an apparent attenuation factor (t_s^*) which is insensitive to complicated earthquake rupture processes. Applying this technique to the Kuril subduction zone, we resolve a velocity amplitude of 4% for the slab core, which is close to previous values derived from waveform modeling. For further global applications of our slab operator method, we suggest that more seismic data and advanced denoising technique should be integrated and implemented, respectively.

4.2 Introduction

Subduction zones are the descending legs of mantle convection cells. The sinking of subducting plates provides the primary driving forces of plate tectonics, and meanwhile, forms highly anomalous thermal and chemical heterogeneities in the mantle (Billen, 2008; Shen et al., 2021). With elevated temperature and pressure at depth, the subducting lithosphere goes through a series of continuous and discontinuous chemical reactions, causing devolatilization and replenishing the ambient mantle (Schmidt and Poli, 2014). As such, the slab temperature provides fundamental constraints on the slab petrological and mechanical process. For example, thermal-petrological calculations have shown that the crust and uppermost mantle of warm subducting slabs become entirely anhydrous at subarc depths, whereas the core of cold subducting plates can transport water to greater depth (Van Keken et al., 2011). As for the deep carbon cycle, in cold subduction zones (e.g. Tonga), the

metamorphic decarbonation mechanism is inefficient for carbon removal. While in warm subduction zones (e.g. Cascadia), carbon is vigorously lost through dissolution and melting of sedimentary carbon (Plank and Manning, 2019).

Also, there is emerging evidence of the temperature control on some intra-slab earthquake characteristics. For instance, the slab temperature indicated by the thermal parameter defined as the product of the slab age, convergence rate and the sine of the slab dip correlates with the separation distance and depth extent of the double seismicity zone at intermediate depths (Brudzinski et al., 2007; Wei et al., 2017). In cold slabs, deep earthquakes (>70 km) tend to present brittle failure with faster rupture velocity, higher aftershock productivity and higher seismic efficiency compared to those in warm slabs (Tibi et al., 2003; Wiens, 2001). In particular, Zhan et al. (2014b) compared the rupture behavior of the 1994 Bolivia and 2013 Sea of Okhotsk deep earthquakes occurred in two end-member slabs (cold vs. warm), respectively. The Okhotsk event in cold slab ruptured 90 km along strike with a velocity of ~4 km/s while the other ruptured ~40 km with a speed of ~1.5 km/s, implying different deep earthquake mechanisms. Even though the governing physics of deep earthquakes remains elusive, the current three leading hypotheses including dehydration embrittlement, transformational faulting and thermal runaway all tightly depend on the thermal state of subducting slabs (Hosseinzadehsabeti et al., 2021; Zhan, 2020). For inferring the thermal state of subducting slab, an accurate seismic structure, at least in the upper mantle, is a prerequisite (Cammarano et al., 2003; Cammarano et al., 2009; Stixrude and Lithgow-Bertelloni, 2012). Compared to the ambient mantle, the subducting slabs are cold and thus characterized as fast velocity anomalies on the order of 1~2% in traveltime based global tomography (Fukao and Obayashi, 2013; Hosseini et al., 2020; Goes et al., 2017; Li et al., 2008; Ritsema et al., 2011; Simmons et al., 2012; Zhao, 2004). In general, traveltime based tomography ubiquitously suffers from the wave front healing effect and thus underestimates the absolute amplitudes of velocity anomalies (Malcolm and Trampert, 2011). On the other hand, using synthetic tests, Lu and Grand (2016) demonstrated that the source mislocation could also significantly smooth the imaging of subducting slabs and introduce structural artifacts to the lower mantle. To reduce the earthquake mislocation effect, Lu et al. (2019) simultaneously inverted the seismic velocity and source locations. The resulting tomography models feature higher velocity amplitude (>2%) within subducting slabs than previous global tomography. Still, the inversion strategy of Lu et al. (2019) requires a thermal slab model as a prior.

Instead, compared to the traveltime inversion, the deterministic waveform modeling

has better sensitivity to the velocity perturbation. As demonstrated by synthetic tests, the fast velocity structure, similarly to the attenuation effect, can effectively broaden seismic waveforms (Mellman and Helmberger, 1974; Vidale, 1987). Utilizing such waveform sensitivity, Zhan et al. (2014a) suggested a 4% faster slab core than the ambient mantle in the Kuril subduction zone. To explain the regional seismograms recorded on Hi-net from two deep earthquakes, Chen et al. (2007) proposed a velocity anomaly of 4.5% within the cold slab and a complex low-velocity mantle wedge beneath Japan. Wang et al. (2014) also found that the observed triplications cannot be reproduced by synthetics based on global tomography models, thus invoked a Japan slab model with high velocity amplitude (~5%). By conducting a regional full waveform tomography with a large seismic dataset, Tao et al. (2018) determined sharp high velocity slabs up to ~5% in the upper mantle beneath the East Asia.

However, the deterministic waveform modeling involves great effort because the source rupture behavior, attenuation (Cormier, 1989), path effect (Ritsema et al., 2020), and receiver-side (Sun and Helmberger, 2011) could contribute great complexities on the seismograms. Not only the shallow earthquakes are complicated, systematic investigations on the source time function of deep earthquakes also reveals that almost half of events exhibit multiple sub-events in the waveforms (Houston, 2015; Persh and Houston, 2004). To reduce these effects, we develop a slab operator method in this study using teleseismic waveforms from deep earthquake pairs with one being a reference event sharing similar raypath with the other event except for the slab side. Using 2D seismic wavefield simulations, we show that the slab operator method is capable of measuring the slab velocity perturbation through an apparent attenuation factor (t_s^*) which is insensitive to complicated earthquake rupture processes. Applying this technique to the Kuril subduction zone, we estimate a velocity amplitude of ~4% for the slab core, which is close to previous values derived from waveform modeling. For further global applications of our slab operator method, we propose that more seismic data and advanced denoising technique should be integrated and implemented, respectively.

4.3 Methodology: Slab Operator

Given two receivers at teleseismic distances ($30^\circ < \Delta < 90^\circ$) and two deep earthquakes A and B (Figure 4.1), the corresponding displacements (U) can be described as a combination of the source term (S), instrumental response (I) and Green's function (G).

$$U_{Ai} = S_{Ai} * G_{Ai} * I_{Ai} \tag{4.1}$$

$$U_{Aj} = S_{Aj} * G_{Aj} * I_{Aj} \tag{4.2}$$

$$U_{Bi} = S_{Bi} * G_{Bi} * I_{Bi} \tag{4.3}$$

$$U_{Bj} = S_{Bj} * G_{Bj} * I_{Bj} \tag{4.4}$$

where $*$ denotes the convolution operator. The subscripts $i(j)$ and $A(B)$ represent the station and event index, respectively. Combining equations 4.1~4.4, the waveform convolution functions $U_{Ai} * U_{Bj}$ and $U_{Aj} * U_{Bi}$ can be expressed as:

$$U_{Ai} * U_{Bj} = S_{Ai} * S_{Bj} * G_{Ai} * G_{Bj} * I_{Ai} * I_{Bj} \tag{4.5}$$

$$U_{Aj} * U_{Bi} = S_{Aj} * S_{Bi} * G_{Aj} * G_{Bi} * I_{Aj} * I_{Bi}. \tag{4.6}$$

In general, the instrumental responses are invariant for permanent broadband stations such that:

$$I_{Ai} = I_{Bi} = I_i \;\&\; I_{Aj} = I_{Bj} = I_j. \tag{4.7}$$

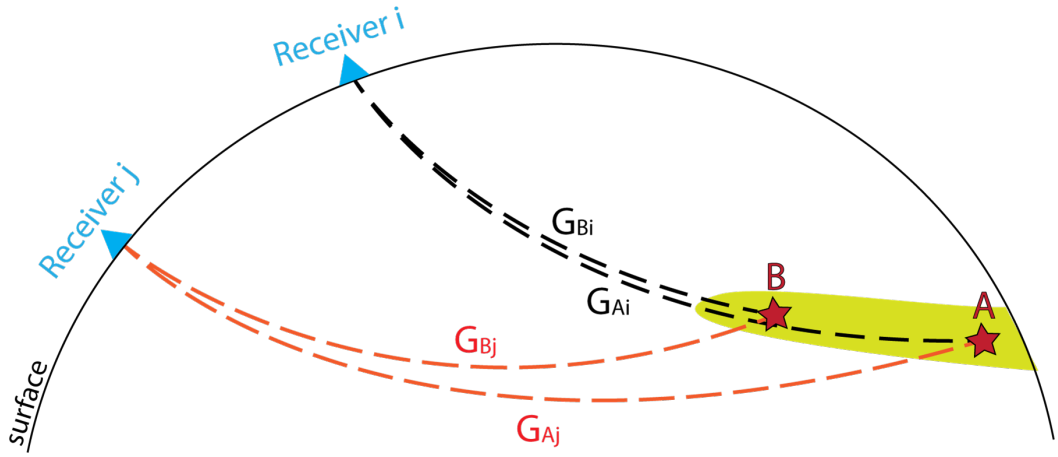

Figure 4.1: Cartoon for the slab operator method. The intraplate earthquakes (A and B) and receivers (i and j) at teleseismic distances are denoted as red stars and blue triangles, respectively. The black and red dashed lines represent the raypaths from earthquakes to receivers i and j, respectively.

For cases that equation 4.7 does not hold, the instrumental responses can be easily removed in the data pre-processing step. As shown in Figure 4.1, seismic waves (e.g. P and S) propagating from events A and B to receiver i share similar raypaths outside the slab, but with an additional segment within the slab for event A (G_{Ai} vs. G_{Bi}). Thus, the Green's function G_{Ai} can be estimated as:

$$G_{Ai} = G_{Bi} * \eta_{slab} \tag{4.8}$$

where η_{slab} represents the slab effect on the Green's function and hereafter is referred to as the slab operator. With equations 4.7~4.8, the waveform convolution functions are written as:

$$U_{Ai} * U_{Bj} = S_{Ai} * S_{Bj} * G_{Bj} * \eta_{slab} * G_{Bi} * I_i * I_j \tag{4.9}$$

$$U_{Aj} * U_{Bi} = S_{Aj} * S_{Bi} * G_{Aj} * G_{Bi} * I_i * I_j. \tag{4.10}$$

To simplify the problem, we make the following two assumptions:

a). Given the same earthquake, the source time functions at receivers i and j are approximately identical. Note that such assumption still holds for deep earthquakes with multi-staged rupture process (Houston, 2015; Persh and Houston, 2004), but not strong rupture directivity (Zhan et al., 2014c). For receivers at teleseismic distances, the vertical rupture directivity can be minimized since the body wave take-off angles only differ by less than 30°. To reduce the horizonal rupture directivity bias, we can choose stations within a limited azimuthal range.

$$S_{Ai} \cong S_{Aj} \;\&\; S_{Bi} \cong S_{Bj} \tag{4.11}$$

b). The high-velocity slab is the major seismic structural anomaly near the source. Because the raypaths from events A and B to receiver j barely sample the slab, but share similar lower mantle and receiver-side structures, the Green's functions G_{Aj} and G_{Bj} are approximately the same. Note that this assumption might be problematic when receivers i and j are interchanged in Figure 4.1.

$$G_{Aj} \cong G_{Bj} \tag{4.12}$$

Substituting equations 4.11~4.12 into equations 4.9~4.10, we have:

$$\eta_{slab} * (U_{Aj} * U_{Bi}) = U_{Ai} * U_{Bj}. \tag{4.13}$$

Without loss of generality, we refer the waveform convolutions $U_{Aj} * U_{Bi}$ and $U_{Ai} * U_{Bj}$ as the reference (W_{ref}) and master (W_{master}) convolution functions, respectively. In this way, equation 4.13 can be reformatted as:

$$\eta_{slab} * W_{ref} = W_{master}. \tag{4.14}$$

Based on the Cagniard-de Hoop method, Mellman and Helmberger (1974) found that a high-velocity layer is nearly equivalent to an attenuation operator that broadens the

seismograms. Since then, similar slab broadening effect has been widely confirmed by numerical experiments (Cormier, 1989; Vidale, 1987; Zhan et al., 2014a). However, opposite to intrinsic attenuation effect that delays the peak arrival, the fast-velocity slab advances seismic signals. Therefore, to analytically describe the slab operator η_{slab}, we adopt a modified Futterman attenuation function solely focusing on the waveform shapes (Shearer, 2019).

$$\eta_{slab}(\omega, t_s^*) = e^{-\frac{1}{2}\omega t_s^*} e^{-i\omega t_s^* ln(\omega)/\pi} \tag{4.15}$$

where t_s^* is the apparent attenuation factor (t^*) due to the high-velocity slab. The two exponential terms on the right-hand side of equation 4.15 represent the waveform amplitude reduction and a frequency-dependent phase shift, respectively. The waveform shapes of slab operator η_{slab} are asymmetric with more emergent onsets than the tails (Figure 4.2). Compared to small t_s^* (e.g. 1.0 s), η_{slab} with larger value (e.g., t_s^*=4.0) s is more depleted of high frequencies and thus can severely broaden the seismic waveforms.

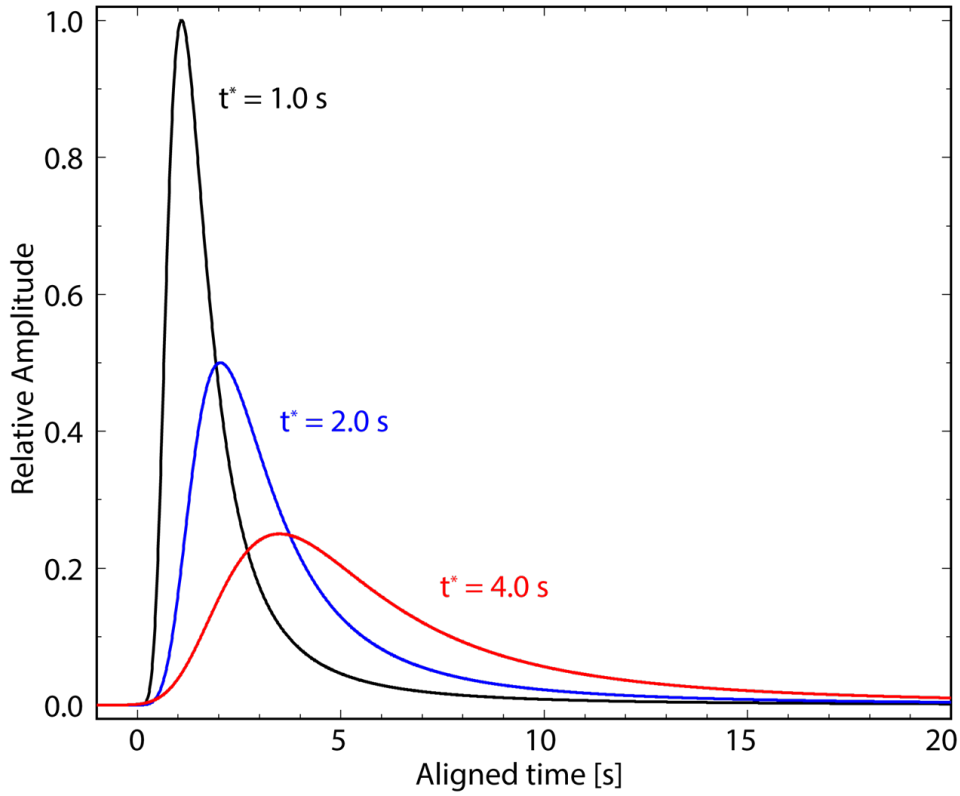

Figure 4.2: The slab operator (η_{slab}) pulse shape for a set of t^*(=1.0 s, 2.0 s, and 4.0 s). The slab operator functions are aligned with onset.

Once we computed the master and reference convolution functions W_{master} and W_{ref}

from teleseismic waveforms, we grid search the optimal t_s^* that gives the highest waveform similarity (or cross-correlation coefficient) between the left-hand side and right-hand side of equation 4.15 to represent the slab velocity anomaly. Note that we do not directly perform the deconvolution using equation 4.15 due to the ill-posedness of deconvolution (Zhong and Zhan, 2020).

4.4 Synthetic Test

Slab Operator Workflow

To validate our proposed slab operator method, we proceed to compute the teleseismic synthetics for a subducting slab with a dip angle of 40° (Figure 4.3a). Our background velocity and density models are adopted from IASP91 (Kennett and Engdahl, 1991). Within the subducting slab, the velocity and density are linearly increased by 5% from the slab interface to its center. More sophisticated slab velocity models should be considered to approach the reality. For example, reconstructing the slab velocity based on the slab temperature profile (Lu et al., 2019; Shen and Zhan, 2020). Here, for the sake of simplicity, the linear velocity profile within the slab is sufficient to demonstrate the feasibility of our slab operator idea. To simulate realistic coda waves, we imposed small-scale isotropic heterogenety in the lithosphere (above 200 km) decribed by a Von K*á*rm*á*n type autocorrelation function (equation 3.1; Sato et al., 2012) with characteristic length of $a_x = a_z = 6.0$ km and a velocity fluctuation of $\varepsilon = 2.0\%$, and elongated intra-slab heterogeneity within the slab with $a_x = 0.5$ km, $a_z = 10$ km and $\varepsilon = 2.5\%$ as suggested by Furumura and Kennett (2005) (Figure 4.3a). Once the velocity and density profiles are setup, teleseismic displacements for two deep earthquakes *A* and *B* at depths of 250 km and 580 km, respectively (Figure 4.3a) are simulated using a fully elastic GPU-based two-dimensional finite difference code which is eighth order in space and second order in time (Li et al., 2014). With a minimum shear velocity of ~3.0 km/s, a grid spacing of 0.5 km, and time step of 0.01 s, synthetic waveforms can be accurate up to ~1 Hz with sampling of at least six grids per wavelength. Here we simplified the problem into a 2D slab geometry since we mainly focus on the down-dip direction and relatively long period waveforms at teleseismic distances. The resulting record sections are shown in Figures 4.3b and 4.3c. Because ray paths from event *A* travel through the high-velocity slab, significant waveform broadening on the direct P wave displacement can be observed at epicnetral distances of 30° ~60°, which is consistent with Mellman and Helmberger (1974) and Zhan et al. (2014a). Whereas the other event *B* is close to the terminus of the subducting slab such that its tele-

seismic waveforms are relatively sharp without slab influence. Therefore, event *B* is used as a reference event to reduce the lower mantle or receiver-side structure effect.

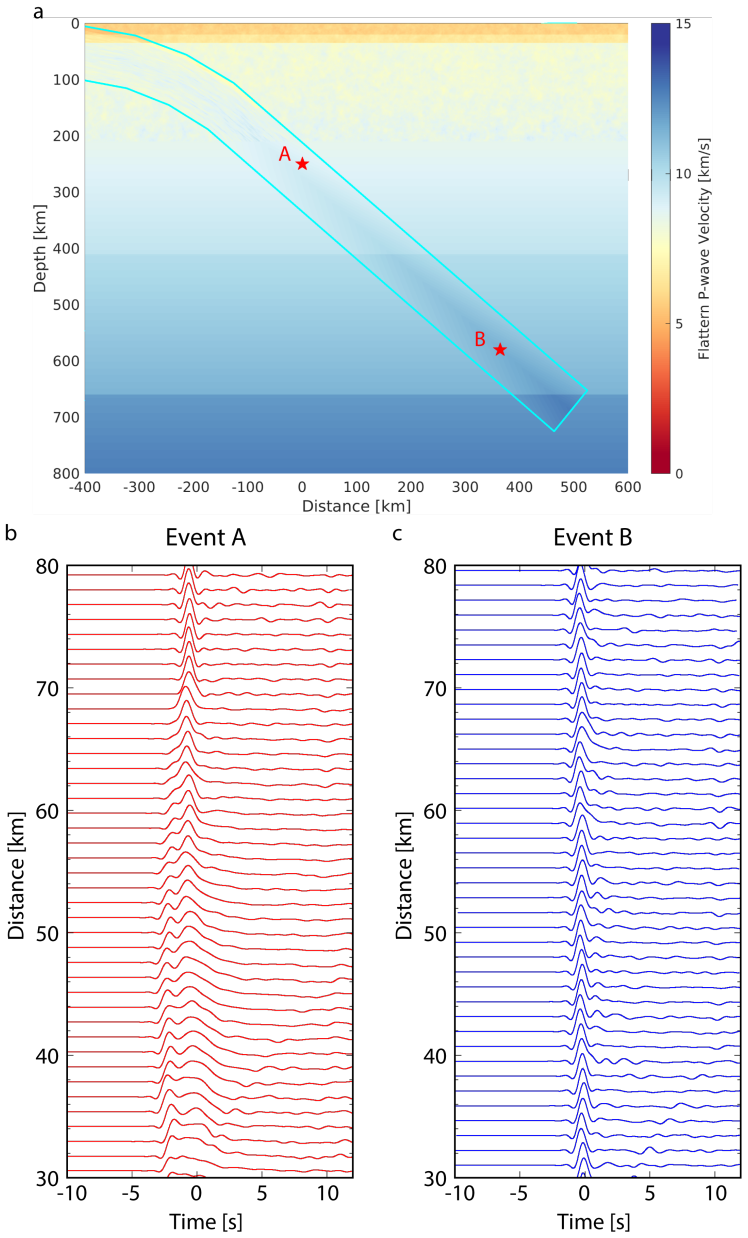

Figure 4.3: Synthetic waveforms for events *A* and *B*. (a). P-wave velocity profile for the subducting slab with a dip angle of 40°. The slab velocity is linearly increased by 5% from the slab interfaces to the center. The cyan line denotes the slab geometry and red stars represent earthquakes *A* and *B*. The distance at 0 km indicates the horizontal location of event A. (b). P-wave synthetic waveform record section for earthquake A. The waveforms are low-pass filtered at 1 Hz and aligned by predicted P-wave arrival times. Note the significant waveform broadening at distances of 30° ∼ 60° for event *A*. (c). Similar to (b), but for deep earthquake *B*.

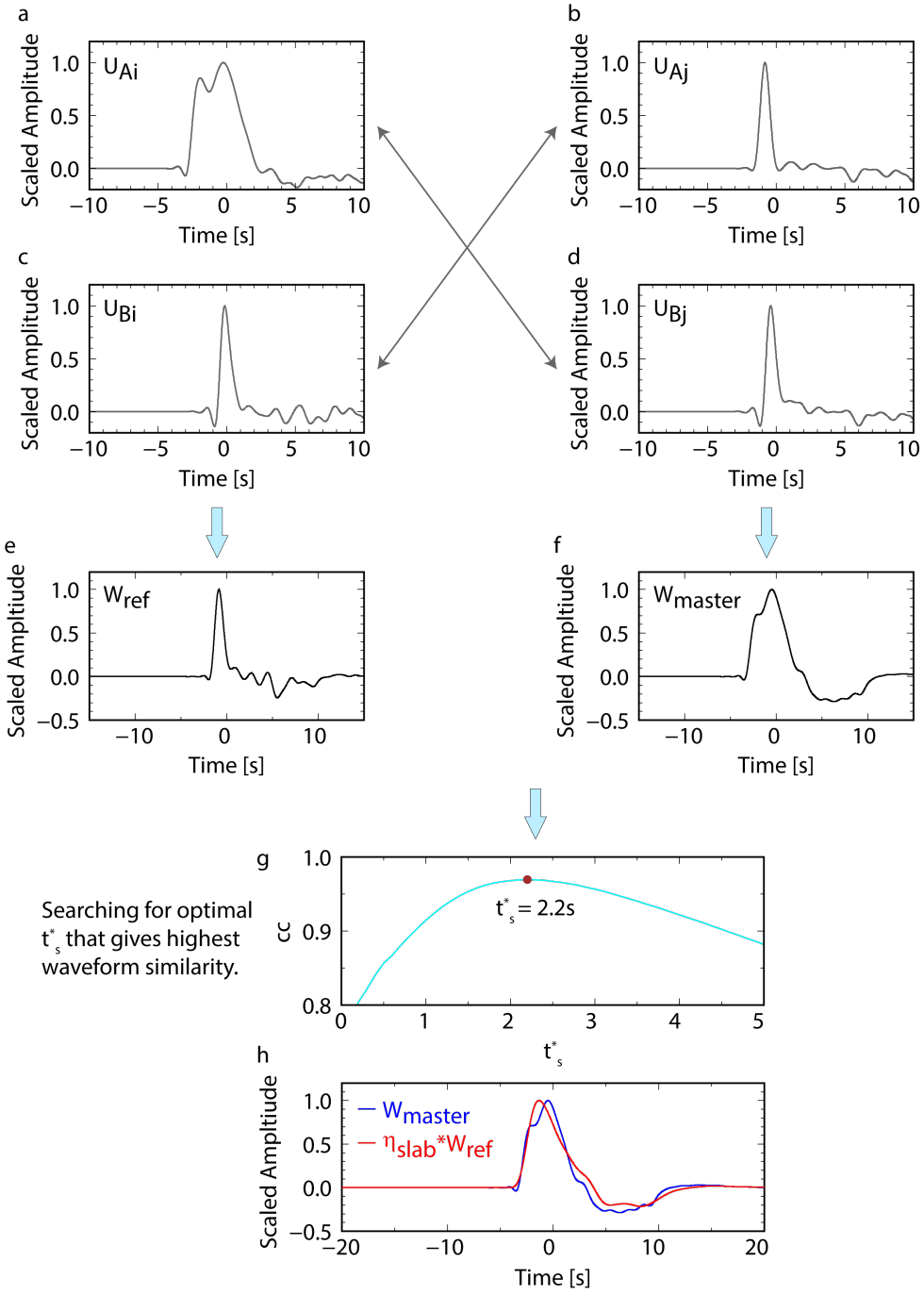

Figure 4.4: Example for the slab operator workflow. (a)~(d). P-wave displacements of U_{Ai}, U_{Aj}, U_{Bi} and U_{Bj}, respectively. The waveforms are low-pass filtered at 1.0 Hz and 10 s before and after the predicted arrivals is used for slab operator. Receivers i and j are at distances of ~40° and ~70°, respectively. (e) and (f). Waveforms of the master and reference convolution functions W_{ref} and W_{master}. (g). Cross-correlation coefficients (cc) as a function of the apparent slab attenuation factor t_s^*. The brown circle denotes the optimal t_s^* (= 2.2 s) that gives highest waveform similarity between $W_{ref} * \eta_{slab}$ and W_{master}. (h). The waveform comparison between W_{master} (blue) and $W_{ref} * \eta_{slab}$ (red) for optimal t_s^* = 2.2 s.

Given the synthetic displacements, we low-pass filter them at 1.0 Hz and cut the vertical-component P wave waveforms from 10 s before to 10 s after the predicted arrivals for U_{Ai}, U_{Aj}, U_{Bi} and U_{Bj}. For the workflow example in Figure 4.4, the receivers i and j are at epicentral distances of ~40° and ~70°, respectively. U_{Ai} is severely broadened by the high-velocity slab while U_{Aj}, U_{Bi} and U_{Bj} barely present waveform distortions (Figures 4.4a~4.4d). Then we compute the waveform convolution functions W_{master} and W_{ref} as defined by equations 4.5 and 4.6, respectively (Figures 4.4e and 4.4f). Note that the master convolution function W_{master} displays much broader waveform (longer duration) than that of reference convolution function W_{ref}. Based on equation 4.15, we grid search the optimal t_s^* ranging from 0.0 s to 5.0 s with an interval of 0.1 s to best satisfy equation 4.14 quantified as highest cross-correlation coefficient (cc) between W_{master} and $\eta_{slab} * W_{ref}$. As shown in Figure 4.4g, a case of $t_s^* = 2.2$ s is found to have the highest cc with a value of 0.97 in the example scenario. After convolving the slab operator η_{slab} of $t_s^* = 2.2$ s and W_{ref}, the duration of $\eta_{slab} * W_{ref}$ is almost identical to the master convolution waveform W_{master} (Figure 4.4h).

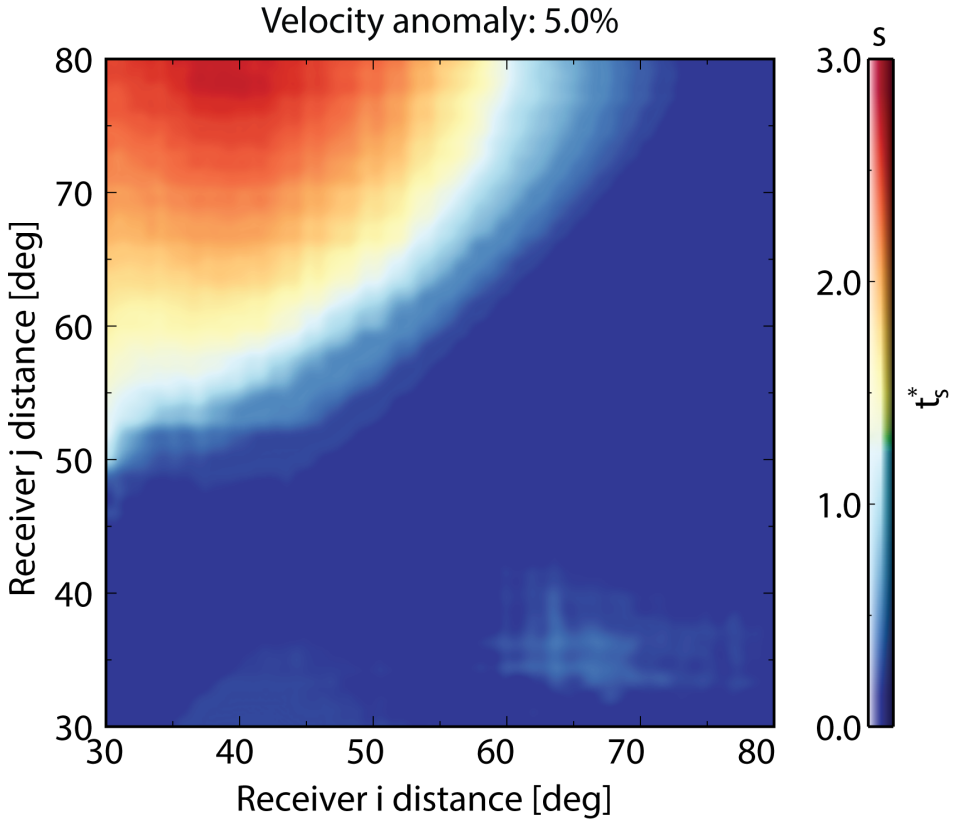

Figure 4.5: Apparent attenuation factor t_s^* map for a subducting slab with a dip angle of 40° and a velocity increase of 5.0% in the center of the slab (Figure 4.3a).

Following the same procedure, we calculate the t_s^* of all the receiver combinations as shown in Figure 4.5. Note that we only utilize the teleseismic waveforms from 30° to 80° here since the core reflected phases (e.g. PcP) can potentially contaminate the direct P phases at distances greater than 80°. In Figure 4.5, the t_s^* gradually increases from bottom right toward top left (40°, 78°) , which is consistent with the displacement record section where event *A* exhibits most severe waveform broadening at distances of ~40° (Figure 4.3b). In our example scenario with a dip angle of 40° and a velocity increase of 5% (Figure 4.3a), the t_s^* can be as large as 2.7 s. Additionally, there appears to be a cluster of relatively higher-than-background t_s^* near (65°, 35°). This is probably an artifact due to the broadened waveform of U_{Aj} in the slab operator method violating our second assumption (equation 4.12).

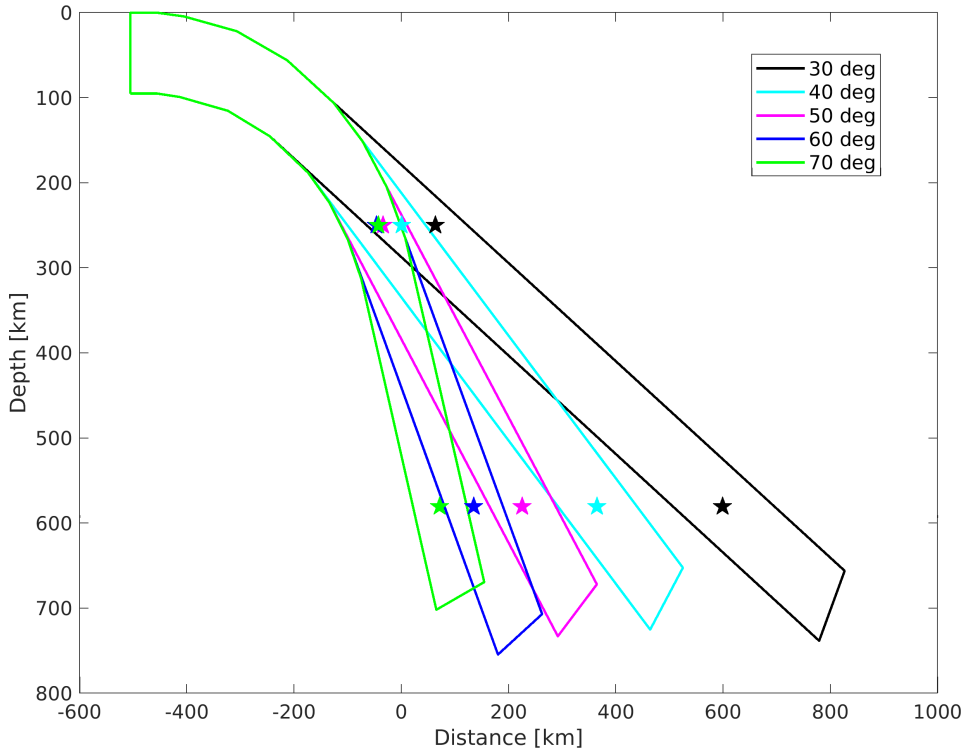

Figure 4.6: Slab geometries for different dip angles from 30° to 70°. The slab velocity is linearly increased from the slab interfaces to the center. The stars represent deep events used in the synthetic tests.

Slab Dip Angle and Velocity Perturbation Effect

Having shown the feasibility of extracting the apparent attenuation factor t_s^* using the slab operator method, we further explore the relation among t_s^*, slab geometry and velocity perturbation. We simulated a variety of slab geometries with dip angles ranging from 30 ° to 70 ° with an interval of 10 ° (Figure 4.6; Hayes et al., 2018;

Hu and Gurnis, 2020) and velocity perturbations linearly increasing to 0.0%, 2.0% and 5.0% from the slab interface to its center (Zhan et al., 2014a). All the slab model parameters and the resulting maximum t_s^* values are summarized in Table 4.1. In each scenario, earthquakes A and B are fixed at depths of 250 km and 580 km, respectively, and their horizontal locations relative to the slab interface are kept constant (Figure 4.6). t_s^* results for different slab geometries and velocity perturbations are shown in Figure 4.7. Due to the lack of slab broadening effect in scenarios without high-velocity slabs (e.g., slab models with velocity perturbation of 0.0%), the values of t_s^* mapped from our slab operator method are always minimum for any receiver combinations (Figures 4.7a,d,g,j and m; Table 4.1). Given the same dip angle, the maximum value of t_s^* increases with the slab velocity perturbation (Figure 4.7). For example, maximum t_s^* values are 0.0 s, 1.1 s and 2.4 s for slab models D30V0, D30V2 and D30V5, respectively (Table 4.1). For cases with velocity perturbations of 2.0% and 5.0%, the maximum t_s^* values are generally 0.8~1.2 s and 2.0~2.7 s, respectively (Table 4.1), suggesting that our resolved t_s^* map could be used to probe the subducting slab velocity anomaly. It should be stated that some symmetric patterns observed in our calculated t_s^* maps (e.g., D50V2 and D50V5 in Figures 4.7h and 4.7i), are likely the artifacts due to the violation of our second assumption (equation 4.12) from broadened U_{Aj}.

Slab Model	**Dip Angle**	**Velocity Perturbation**	**Max t_s^* Value and Location**
D30V0	30°	0.0%	0.0 s @ everywhere
D30V2	30°	2.0%	1.1 s @ (30.2°, 47.9°)
D30V5	30°	5.0%	2.4 s @ (30.2°, 57.9°)
D40V0	40°	0.0%	0.0 s @ everywhere
D40V2	40°	2.0%	1.2 s @ (41.4°, 76.6°)
D40V5	40°	5.0%	2.7 s @ (39.9°, 78.0°)
D50V0	50°	0.0%	0.0 s @ everywhere
D50V2	50°	2.0%	0.8 s @ (60.8°, 36.5°)
D50V5	50°	5.0%	1.6 s @ (59.1°, 31.2°)
D60V0	60°	0.0%	0.0 s @ everywhere
D60V2	60°	2.0%	0.8 s @ (80.0°, 38.7°)
D60V5	60°	5.0%	2.1 s @ (79.2°, 39.4°)
D70V0	70°	0.0%	0.0 s @ everywhere
D70V2	70°	2.0%	0.2 s @ (30.7°, 69.8°)
D70V5	70°	5.0%	0.8 s @ (80.0°, 56.9°)

Table 4.1: Summary of simulated slab model parameters and t_s^* results.

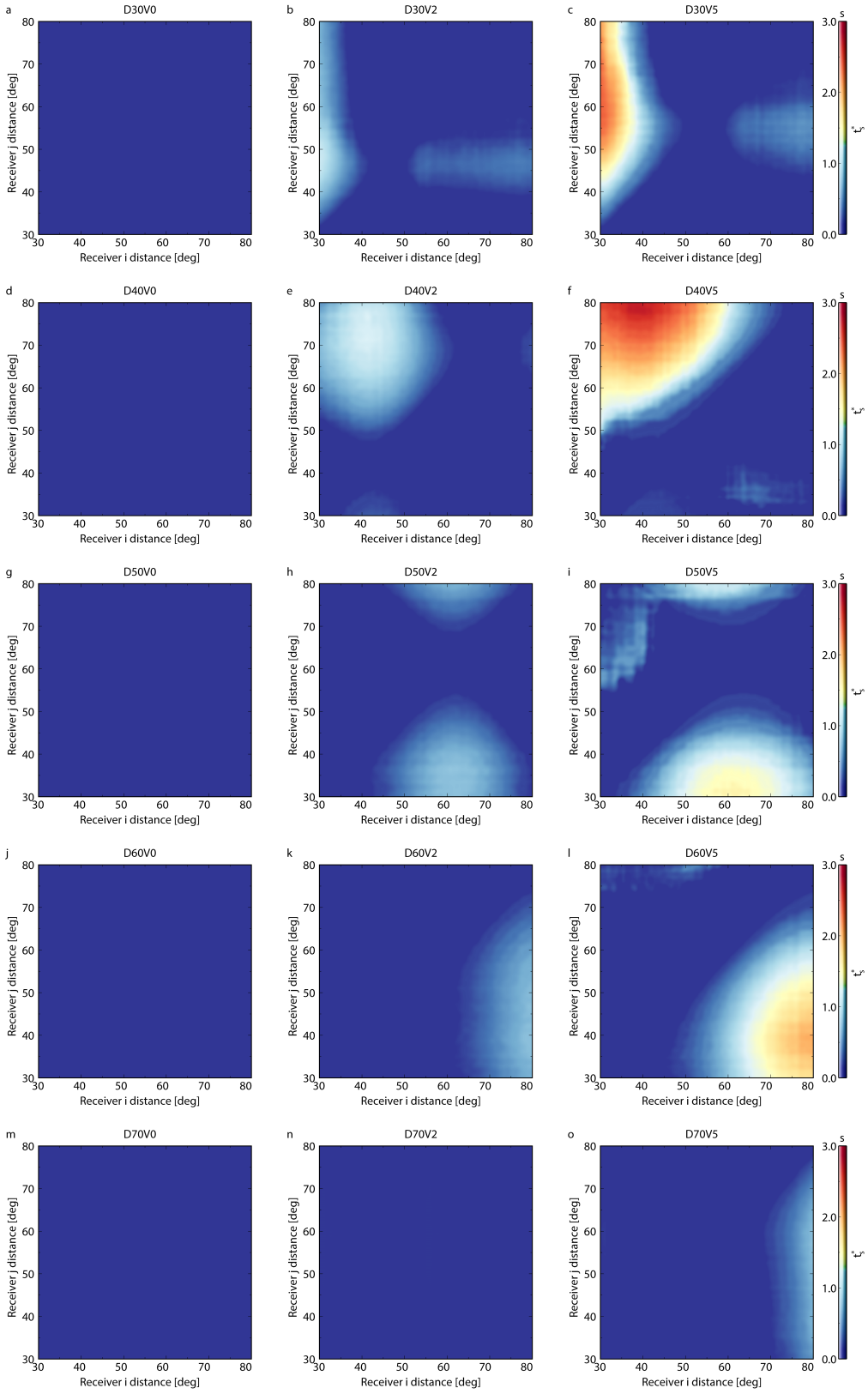

Figure 4.7: Apparent attenuation factor t_s^* map for different slab models. The dip angles and velocity perturbations of all the models are summarized in Table 4.1.

Note that the locations of maximum t_s^* for cases with same dip angles can be slightly shifted (e.g. D40/50V2 vs. D40/50V5 in Table 4.1) because different slab velocity anomalies slightly perturb stationary raypaths from event A to event B. One exception is for cases with a dip angle of 70° in which their stationary raypaths are outside our distance range (Figure 4.7m~o). Furthermore, given the same slab velocity perturbation, the slab geometry can also significantly modulate t_s^* not only on its maximum values but also the locations (Table 4.1). Because the raypaths from event A to event B are closer to vertical for steeper dipping slabs, the maximum t_s^* locations generally increase with dip angles along the receiver i distance dimension (Figure 4.7).

Source Time Function Effect

For more than a half of deep earthquakes, their source rupture processes can be complex with multiple stages (Houston, 2015; Persh and Houston, 2004). Since both W_{ref} and W_{master} include the source terms of events A and B (equations 4.11 and 4.14), our slab operator method is theoretically capable of resolving the slab velocity anomaly by utilizing teleseismic waveforms with complicated source time functions. To verify this point, we constructed two source time funtions (STF1 and STF2) with a duration of 1.5 s as shown in Figure 4.8a to represent complicated source rupture process. STF1 is consist of two Gaussian type subevents at a centroid time of 0.32 s and 0.75 s, respectively, whereas STF2 includes three subevents at centroid time of 0.40 s, 0.75 s and 1.10 s, respectively (Figure 4.8). Based on the slab model D40V2, we tested two scenarios Astf1Bstf2_D40V2 indicating that synthetic waveforms of event A and B are convolved with STF1 and STF2, respectively, and Astf2Bstf1_D40V2 representing that synthetic waveforms of event A and B are convolved with STF2 and STF1, respectively. The resulting t_s^* maps are almost identical as that of D40V2 (Figures 4.8b and 4.8c vs. 4.7e; Table 4.2). The maximum t_s^* are the same but with slight location differences within 2°. Furthermore, we also calculate the t_s^* difference between Astf1Bstf2_D40V2 (Astf2Bstf1_D40V2) and D40V2 which only considers δ-like source time functions as shown in Figure 4.8d(e). The differences in t_s^* are generally less than 0.3 s, validating our slab operator method for complicated source processes. Similar results also hold for higher slab velocity anomaly case D40V5 (Figure 4.9; Table 4.2). Intriguingly, involving the source complexity seems to diminish the t_s^* artifact near (65°,35°) (Figure 4.9 vs. 4.5). Therefore, our synthetic tests confirm that our slab operator method can resolve the slab velocity anomaly by using t_s^* as a proxy and has little

sensitivity on the deep earthquake rupture complexity, allowing us to utilize more real data with complicated but coherent waveforms.

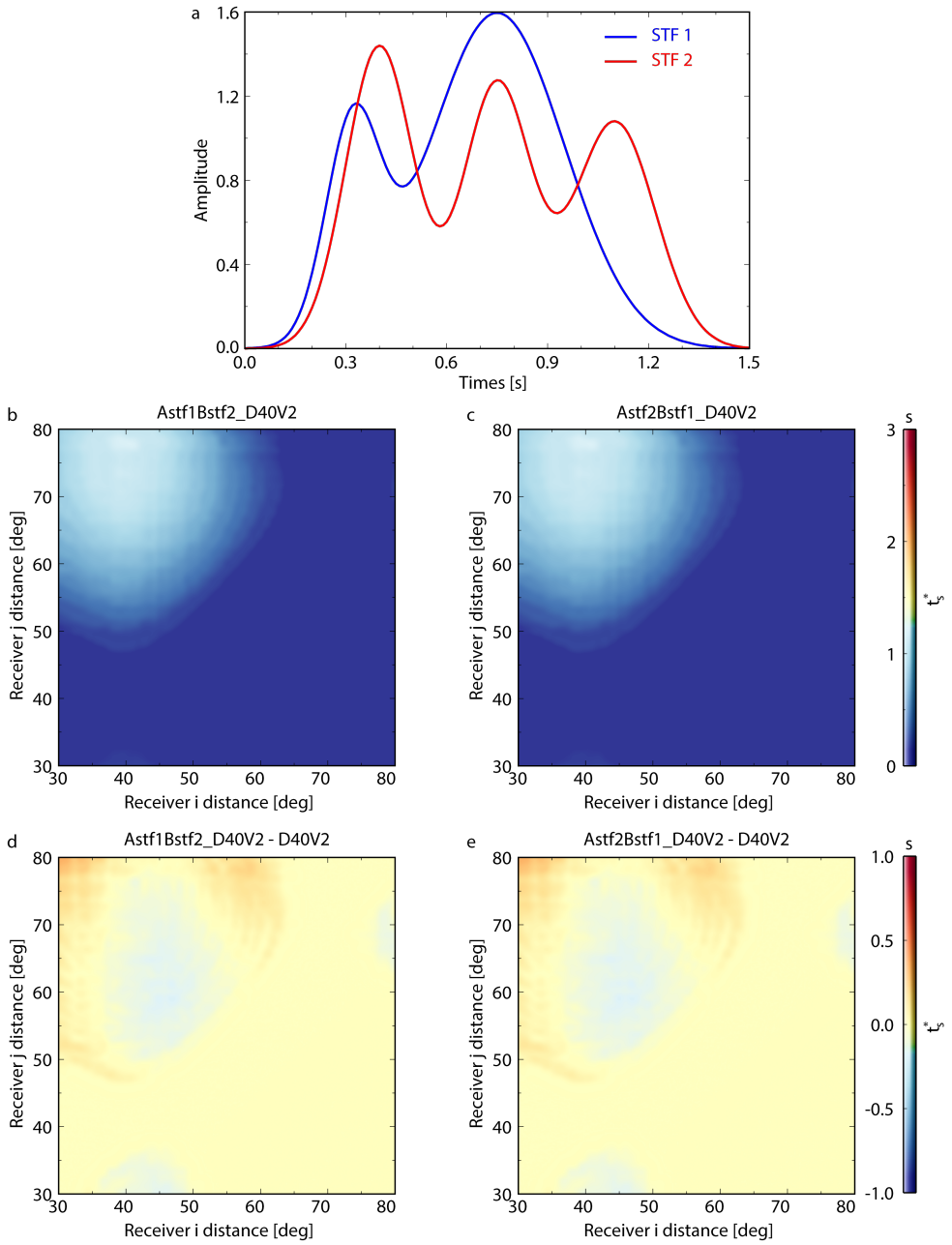

Figure 4.8: Source time function effect on t_s^* estimation for D40V2 cases. (a). Constructed source time functions (STF1 and STF2) with a duration of 1.5 s. (b). t_s^* map for slab case Astf1Bstf2_D40V2 in which synthetic waveforms of event *A* and *B* are convolved with STF1 and STF2, respectively. (c). Similar to (b), but for slab case Astf2Bstf1_D40V2 in which synthetic waveforms of event *A* and *B* are convolved with STF2 and STF1, respectively. (d). t_s^* map difference between slab cases Astf1Bstf2_D40V2 and D40V2. (e). t_s^* map difference between slab cases Astf2Bstf1_D40V2 and D40V2.

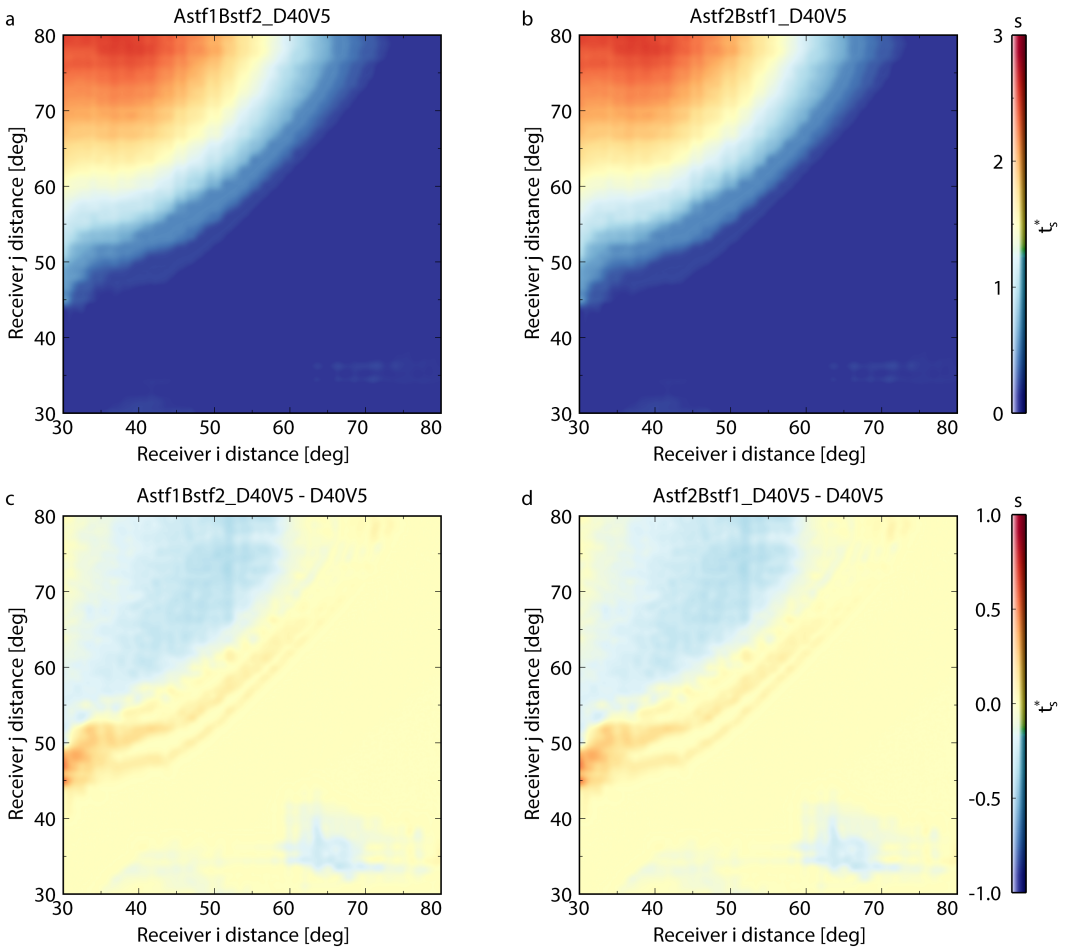

Figure 4.9: Source time function effect on t_s^* estimation for D40V2 cases. (a). t_s^* map for slab case Astf1Bstf2_D40V5 in which synthetic waveforms of event *A* and *B* are convolved with STF1 and STF2, respectively. (b). Similar to (a), but for slab case Astf2Bstf1_D40V5 in which synthetic waveforms of event *A* and *B* are convolved with STF2 and STF1, respectively. (c). t_s^* map difference between slab cases Astf1Bstf2_D40V5 and D40V5. (d). t_s^* map difference between slab cases Astf2Bstf1_D40V5 and D40V5.

Slab Model	**Event *A* STF**	**Event *B* STF**	**Max t_s^* Value and Location**
D40V2	δ	δ	1.2 s @ (41.4°, 76.6°)
Astf1Bstf2_D40V2	STF1	STF2	1.2 s @ (40.6°, 77.8°)
Astf2Bstf1_D40V2	STF2	STF1	1.2 s @ (40.6°, 77.8°)
D40V5	δ	δ	2.7 s @ (39.9°, 78.0°)
Astf1Bstf2_D40V5	STF1	STF2	2.6 s @ (36.8°, 80.0°)
Astf2Bstf1_D40V5	STF2	STF1	2.6 s @ (36.8°, 80.0°)

Table 4.2: Summary of tested source time function scenarios and t_s^* results.

4.5 Application

Kuril Subduction Zone

We further apply the slab operator method to estimate the slab velocity anomaly of the Kuril subduction zone where the Eurasian continental plate is overriding old Pacific oceanic lithosphere (90~135 m.y.; Sdrolias and Müller, 2006). As shown in Figure 4.10, event *A* is the 2009/04/21, Mw6.2 earthquake with a focal depth of ~160 km while event *B* is the 2013/10/01, Mw6.9 earthquake at a depth of ~580 km (Engdahl et al., 2020). To account for our 2D assumption and the nonuniform distribution of seismic stations, we download data for stations that record both events at distances of 30° ~ 90° and within azimuths of ±45°. We remove the instrumental response, mean value and linear trend, and filter the seismograms with a two-pole Butterworth band-pass filter of 0.01-1 Hz. Roughly 160 stations of high signal-to-noise ratios (>2.0) are selected and most of them are clustered in Europe at distances of 45° ~ 85° (Figure 4.10a). A 30 s time window with 10 s before and 20 s after the direct P arrival is used for our slab operator method, and the polarities of all the seismograms are corrected to positive for later convolution processing. To achieve robust results, we stack waveforms located within a area of 1° in distance and 10° in azimuth.

As shown in Figure 4.10b, high t_s^* values are clustered near (50°, 80°) with a peak value of ~2.0. To estimate the velocity perturbation, we examine a set of slab scenarios with a dip angle of 45 ° as suggested by Hayes et al. (2018) and velocity perturbations ranging from 2% to 5% with an interval of 1%. Similar to aforementioned synthetic tests, regardless of the artifacts around (55°, 35°), the higher the slab velocity perturbation, the larger t_s^* is (Figures 4.10c~f). The case of D45V2 generally underestimates the observed t_s^* (Figures 4.10b vs. 4.10c), suggesting a higher slab velocity anomaly at the Kuril subduction zone. When the slab velocity perturbation reaches 5%, the synthetic result has a much broader high t_s^* area than observations. In fact, our observed maximum t_s^* for the event pair 20090421-20131001 is closer to that of case D45V4 with a peak value of 2.1 s (Figures 4.10b vs. 4.10e). Therefore, we imply that the Kuril subduction zone can be characterized by a velocity increase of ~4% within the slab between depths 160 km and 580 km. Our suggested 4% is slightly lower than 5% derived from Zhan et al. (2014a), but significantly higher than 2% from tomography models. Nevertheless, more seismic waveforms and deep earthquake pairs should be utilized to accurately estimate the velocity anomaly of the Kuril subduction zone.

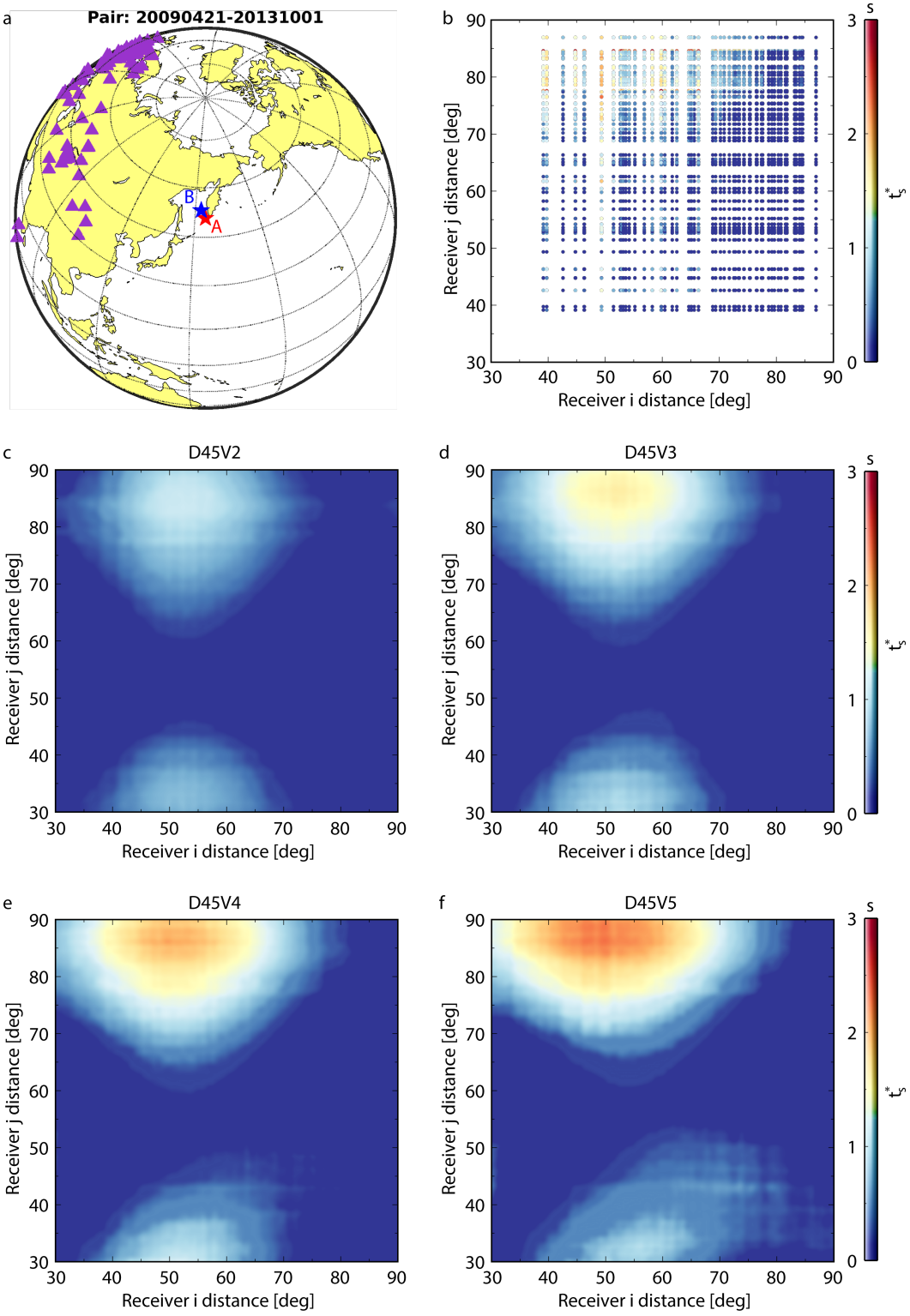

Figure 4.10: Slab operator application in the Kuril subduction zone. (a). Map view of selected stations (purple triangles) and deep earthquakes 20090421 (red star) and 20131001 (blue star). (b). t_s^* result for earthquake pair the 20090421-20131001. t_s^* maps for synthetic slab cases (c). D45V2, (d). D45V3, (e). D45V4, and (f). D45V5.

Current Limitations for Global Applications

Compared to the deterministic waveform modeling which involves great effort in scrutinizing waveform details from earthquakes with relatively simple source time functions, our slab operator method, due to its little dependence of the source complexity, is a more generalizable approach to resolve the velocity perturbations of global subduction zones. With abundant deep earthquakes across the globe (Figure 4.11), the slab operator method provides an effective way to accurately evaluate the relation between the slab thermal state and corresponding seismic velocity anomaly. However, we should also point out the challenge of global applications of the slab operator method. Since more than 70% of the Earth's surface is covered by the ocean where is logistically challenging for seismic instrumentations (Figure 4.11), only limited number of seismic data are available for several subduction zones scenarios. For example, the teleseismic distances of deep earthquakes in South America are in the Atlantic Ocean. While for the cold Fiji-Tonga subduction, most teleseismic areas are covered by the Indian Ocean (Figure 4.11). To account for the nonuniform distribution of global seismic stations, regional seismic networks and marine instrumentations should be integrated, collected and analyzed in the future.

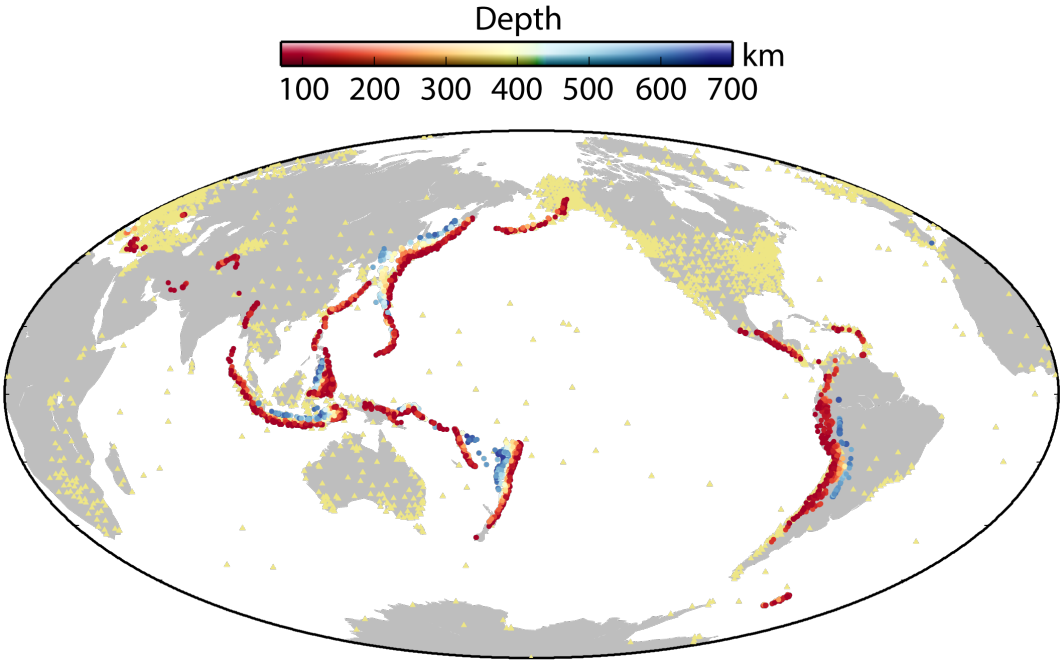

Figure 4.11: Global distribution of M5.5+ deep earthquakes (circles; Engdahl et al., 2020) and permanent seismic stations (khaki triangles).

On the other hand, because all the signals around the direct P arrival time window contribute to the convolution functions W_{master} and W_{ref}, the t_s^* results are also

sensitive to the noise level and coda waves in the real data. For example, given the same stations and earthquake pair, different convolution time windows (e.g., 20 s vs. 30 s) and processing procedures (e.g., removing linear trend before or after cutting waveforms) can perturb t_s^* up to 0.5 s, which could result in a big estimation uncertainty of the slab velocity. To achieve robust t_s^* measurements, we suggest that machine learning algorithms, such as deep neural networks, could be used for denoising or decomposing targeted seismic signals (Zhu et al., 2019).

4.6 Conclusions

In this study, we develop a slab operator method to resolve slab velocity perturbations using teleseismic waveforms from earthquake pairs. We perform synthetic tests to illustrate the feasibility of estimating the slab velocity perturbation through an apparent attenuation factor (t_s^*) and the slab operator approach is insensitive to complicated source processes, which enabling making use of a large number of waveform sets. Applying this technique to the Kuril subduction zone, we suggest a velocity amplitude of 4% within the slab core, which is consistent with previous waveform modeling studies, but higher than that suggested in tomography models. Nevertheless, as for global and robust applications of our slab operator method, more regional seismic networks and marine instrumentations should be integrated and advanced algorithms, such as machine learning based denoising methods, should be implemented.

References

Billen, M. I. (2008). Modeling the dynamics of subducting slabs. In: *Annual Review of Earth and Planetary Sciences* 36.1, pp. 325–356. DOI: 10.1146/annurev.earth.36.031207.124129.

Brudzinski, M. R. et al. (2007). Global prevalence of double Benioff zones. In: *Science*. DOI: 10.1126/science.1139204.

Cammarano, F. et al. (2003). Inferring upper-mantle temperatures from seismic velocities. In: *Physics of the Earth and Planetary Interiors* 138.3. Publisher: Elsevier, pp. 197–222. DOI: 10.1016/S0031-9201(03)00156-0.

Cammarano, F. et al. (2009). Inferring the thermochemical structure of the upper mantle from seismic data. In: *Geophysical Journal International* 179.2, pp. 1169–1185. ISSN: 0956-540X. DOI: 10.1111/j.1365-246X.2009.04338.x.

Chen, M. et al. (2007). Waveform modeling of the slab beneath Japan. In: *Journal of Geophysical Research: Solid Earth* 112 (B2). ISSN: 2156-2202. DOI: 10.1029/2006JB004394.

Cormier, V. F. (1989). Slab diffraction of S waves. In: *Journal of Geophysical Research: Solid Earth* 94 (B3), pp. 3006–3024. ISSN: 2156-2202. DOI: 10.1029/JB094iB03p03006.

Engdahl, E. R. et al. (2020). ISC-EHB 1964–2016, an improved data set for studies of Earth structure and global seismicity. In: *Earth and Space Science* 7.1, e2019EA000897. ISSN: 2333-5084. DOI: 10.1029/2019EA000897.

Fukao, Y. and M. Obayashi (2013). Subducted slabs stagnant above, penetrating through, and trapped below the 660 km discontinuity. In: *Journal of Geophysical Research: Solid Earth* 118.11, pp. 5920–5938. ISSN: 2169-9356. DOI: 10.1002/2013JB010466.

Furumura, T. and B. L. N. Kennett (2005). Subduction zone guided waves and the heterogeneity structure of the subducted plate: Intensity anomalies in northern Japan. In: *Journal of Geophysical Research: Solid Earth* 110 (B10). Publisher: Wiley Online Library. DOI: 10.1029/2004JB003486.

Goes, S. et al. (2017). Subduction-transition zone interaction: A review. In: *Geosphere* 13.3, pp. 644–664. ISSN: 1553-040X. DOI: 10.1130/GES01476.1.

Hayes, G. P. et al. (2018). Slab2, a comprehensive subduction zone geometry model. In: *Science* 362.6410. Publisher: American Association for the Advancement of Science, pp. 58–61. DOI: 10.1126/science.aat4723.

Hosseini, K. et al. (2020). Global mantle structure from multifrequency tomography using P, PP and P-diffracted waves. In: *Geophysical Journal International* 220.1, pp. 96–141. ISSN: 0956-540X. DOI: 10.1093/gji/ggz394.

Hosseinzadehsabeti, E. et al. (2021). The rupture mechanisms of intraslab earthquakes: A multiscale review and re-evaluation. In: *Earth-Science Reviews* 221, p. 103782. ISSN: 0012-8252. DOI: 10.1016/j.earscirev.2021.103782.

Houston, H. (2015). 4.13 - Deep Earthquakes. In: *Treatise on Geophysics (Second Edition)*. Ed. by G. Schubert. Oxford: Elsevier, pp. 329–354. ISBN: 978-0-444-53803-1. DOI: 10.1016/B978-0-444-53802-4.00079-8.

Hu, J. and M. Gurnis (2020). Subduction duration and slab dip. In: *Geochemistry, Geophysics, Geosystems* 21.4, e2019GC008862. ISSN: 1525-2027. DOI: 10.1029/2019GC008862.

Kennett, B. L. N. and E. R. Engdahl (1991). Traveltimes for global earthquake location and phase identification. In: *Geophysical Journal International* 105.2. Publisher: Oxford University Press, pp. 429–465. DOI: 10.1111/j.1365-246X.1991.tb06724.x.

Li, C. et al. (2008). A new global model for P wave speed variations in Earth's mantle. In: *Geochemistry, Geophysics, Geosystems* 9.5. ISSN: 1525-2027. DOI: 10.1029/2007GC001806.

Li, D. et al. (2014). Global synthetic seismograms using a 2-D finite-difference method. In: *Geophysical Journal International* 197.2, pp. 1166–1183. ISSN: 0956-540X. DOI: 10.1093/gji/ggu050.

Lu, C. and S. P. Grand (2016). The effect of subducting slabs in global shear wave tomography. In: *Geophysical Journal International* 205.2, pp. 1074–1085. ISSN: 0956-540X. DOI: 10.1093/gji/ggw072.

Lu, C. et al. (2019). TX2019slab: A new P and S tomography model incorporating subducting slabs. In: *Journal of Geophysical Research: Solid Earth* 124.11, pp. 11549–11567. ISSN: 2169-9356. DOI: 10.1029/2019JB017448.

Malcolm, A. E. and J. Trampert (2011). Tomographic errors from wave front healing: more than just a fast bias. In: *Geophysical Journal International* 185.1, pp. 385–402. ISSN: 0956-540X. DOI: 10.1111/j.1365-246X.2011.04945.x.

Mellman, G. R. and D. V. Helmberger (1974). High-frequency attenuation by a thin high-velocity layer. In: *Bulletin of the Seismological Society of America* 64.5, pp. 1383–1388. ISSN: 0037-1106. DOI: 10.1785/BSSA0640051383.

Persh, S. E. and H. Houston (2004). Deep earthquake rupture histories determined by global stacking of broadband P waveforms. In: *Journal of Geophysical Research: Solid Earth* 109 (B4). ISSN: 2156-2202. DOI: 10.1029/2003JB002762.

Plank, T. and C. E. Manning (2019). Subducting carbon. In: *Nature* 574.7778, pp. 343–352. ISSN: 1476-4687. DOI: 10.1038/s41586-019-1643-z.

Ritsema, J. et al. (2011). S40RTS: a degree-40 shear-velocity model for the mantle from new Rayleigh wave dispersion, teleseismic traveltime and normal-mode splitting function measurements. In: *Geophysical Journal International* 184.3, pp. 1223–1236. ISSN: 0956-540X. DOI: 10.1111/j.1365-246X.2010.04884.x.

Ritsema, J. et al. (2020). The dimensions of scatterers in the lower mantle using USArray recordings of S-wave to P-wave conversions. In: *Physics of the Earth and Planetary Interiors* 306, p. 106541. ISSN: 0031-9201. DOI: 10.1016/j.pepi.2020.106541.

Sato, H. et al. (2012). *Seismic wave propagation and scattering in the heterogeneous earth*. Springer Science & Business Media. ISBN: 978-3-642-44318-3. DOI: 10.1007/978-3-642-23029-5.

Schmidt, M. W. and S. Poli (2014). 4.19 - devolatilization during subduction. In: *Treatise on Geochemistry (Second Edition)*. Ed. by H. D. Holland and K. K. Turekian. Oxford: Elsevier, pp. 669–701. ISBN: 978-0-08-098300-4. DOI: 10.1016/B978-0-08-095975-7.00321-1.

Sdrolias, M. and R. D. Müller (2006). Controls on back-arc basin formation. In: *Geochemistry, Geophysics, Geosystems* 7.4. Publisher: Wiley Online Library. DOI: 10.1029/2005GC001090.

Shearer, P. M. (2019). *Introduction to Seismology*. Publisher: Cambridge University Press. DOI: 10.1017/9781316877111.

Shen, Z. and Z. Zhan (2020). Metastable olivine wedge beneath the Japan Sea imaged by seismic interferometry. In: *Geophysical Research Letters* 47.6, e2019GL085665. ISSN: 1944-8007. DOI: 10.1029/2019GL085665.

Shen, Z. et al. (2021). Small-scale intraslab heterogeneity weakens into the mantle transition zone. In: *Geophysical Research Letters* 48.23, e2021GL094470. ISSN: 1944-8007. DOI: 10.1029/2021GL094470.

Simmons, N. A. et al. (2012). LLNL-G3Dv3: Global P wave tomography model for improved regional and teleseismic travel time prediction. In: *Journal of Geophysical Research: Solid Earth* 117 (B10). ISSN: 2156-2202. DOI: 10.1029/2012JB009525.

Stixrude, L. and C. Lithgow-Bertelloni (2012). Geophysics of chemical heterogeneity in the mantle. In: *Annual Review of Earth and Planetary Sciences* 40.1, pp. 569–595. DOI: 10.1146/annurev.earth.36.031207.124244.

Sun, D. and D. Helmberger (2011). Upper-mantle structures beneath USArray derived from waveform complexity. In: *Geophysical Journal International* 184.1. ISSN: 0956-540X. DOI: 10.1111/j.1365-246X.2010.04847.x.

Tao, K. et al. (2018). Seismic structure of the upper mantle beneath eastern Asia from full waveform seismic tomography. In: *Geochemistry, Geophysics, Geosystems* 19.8, pp. 2732–2763. ISSN: 1525-2027. DOI: 10.1029/2018GC007460.

Tibi, R. et al. (2003). Source characteristics of large deep earthquakes: Constraint on the faulting mechanism at great depths. In: *Journal of Geophysical Research: Solid Earth* 108 (B2). ISSN: 2156-2202. DOI: 10.1029/2002JB001948.

Van Keken, P. E. et al. (2011). Subduction factory: 4. Depth-dependent flux of H_2O from subducting slabs worldwide. In: *Journal of Geophysical Research: Solid Earth* 116 (B1). ISSN: 2156-2202. DOI: 10.1029/2010JB007922.

Vidale, J. E. (1987). Waveform effects of a high-velocity, subducted slab. In: *Geophysical Research Letters* 14.5, pp. 542–545. ISSN: 1944-8007. DOI: 10.1029/GL014i005p00542.

Wang, T. et al. (2014). Two-dimensional/three-dimensional waveform modeling of subducting slab and transition zone beneath Northeast Asia. In: *Journal of Geophysical Research: Solid Earth* 119.6, pp. 4766–4786. ISSN: 2169-9356. DOI: 10.1002/2014JB011058.

Wei, S. S. et al. (2017). Slab temperature controls on the Tonga double seismic zone and slab mantle dehydration. In: *Science Advances*. Publisher: American Association for the Advancement of Science. DOI: 10.1126/sciadv.1601755.

Wiens, D. A. (2001). Seismological constraints on the mechanism of deep earthquakes: temperature dependence of deep earthquake source properties. In: *Physics of the Earth and Planetary Interiors*. Processes and Consequences of Deep Subduction 127.1, pp. 145–163. ISSN: 0031-9201. DOI: 10.1016/S0031-9201(01)00225-4.

Zhan, Z. (2020). Mechanisms and implications of deep earthquakes. In: *Annual Review of Earth and Planetary Sciences* 48.1, pp. 147–174. DOI: 10.1146/annurev-earth-053018-060314.

Zhan, Z. et al. (2014a). Imaging subducted slab structure beneath the Sea of Okhotsk with teleseismic waveforms. In: *Physics of the Earth and Planetary Interiors* 232. Publisher: Elsevier, pp. 30–35. DOI: 10.1016/j.pepi.2014.03.008.

Zhan, Z. et al. (2014b). Rupture complexity of the 1994 Bolivia and 2013 Sea of Okhotsk deep earthquakes. In: *Earth and Planetary Science Letters* 385. Publisher: Elsevier, pp. 89–96. DOI: 10.1016/j.epsl.2013.10.028.

Zhan, Z. et al. (2014c). Supershear rupture in a Mw 6.7 aftershock of the 2013 Sea of Okhotsk earthquake. In: *Science*. Publisher: American Association for the Advancement of Science. DOI: 10.1126/science.1252717.

Zhao, D. (2004). Global tomographic images of mantle plumes and subducting slabs: insight into deep Earth dynamics. In: *Physics of the Earth and Planetary Interiors*. Plumes and Superplumes 146.1, pp. 3–34. ISSN: 0031-9201. DOI: 10.1016/j.pepi.2003.07.032.

Zhong, M. and Z. Zhan (2020). An array-based receiver function deconvolution method: methodology and application. In: *Geophysical Journal International* 222.1, pp. 1–14. ISSN: 0956-540X. DOI: 10.1093/gji/ggaa113.

Zhu, W. et al. (2019). Seismic signal denoising and decomposition using deep neural networks. In: *IEEE Transactions on Geoscience and Remote Sensing* 57.11, pp. 9476–9488. ISSN: 1558-0644. DOI: 10.1109/TGRS.2019.2926772.

Chapter 5

HIGH-RESOLUTION VADOSE ZONE WATER SATURATION MONITORING USING DISTRIBUTED ACOUSTIC SENSING

5.1 Abstract

Water in the critical zone is vital, but its current monitoring techniques are mostly for surface water content with few probing the vadose zone. To fill in this gap, time-lapse seismology is a complimentary tool, but suffers from large conventional sensor spacing. The emerging distributed acoustic sensing (DAS) technology provides an affordable and scalable solution for deploying large-aperture and ultra-dense seismic arrays, thus feasible for the vadose zone monitoring. With two years of ambient noise recorded on the Ridgecrest DAS array in California, the resulting seismic changes (dv/v) reveal an unprecedented high-resolution spatiotemporal evolution of water saturation in the vadose zone. We observe a striking correlation between the dv/v amplitude and the sedimentary thickness. The frequency analysis of dv/v measurements further suggests an uppermost 10 m hydrologic source as the cause for dv/v temporary and seasonal variability. Our results indicate the great potential of DAS for long-term subsurface water monitoring.

5.2 Introduction

Water in the critical zone that spans from the top of vegetation canopy to the base of groundwater plays a vital and strategic role in sustaining all life on Earth (National Research Council, 2001; Grant and Dietrich, 2017). For example, groundwater in the saturated zone serves as a primary source of drinking water worldwide (Döll et al., 2012), and strengthens the resilience of anthropogenic uses of water to climate variability and change (Cuthbert et al., 2019; Lall et al., 2020). Soil moisture, another fundamental ecohydrological ingredient, controls microbial activities and plant transpiration with consequent impacts on the partitioning of water and energy budget and biochemical cycles (Oki and Kanae, 2006; Seneviratne et al., 2010). Furthermore, between the surface and the groundwater table, infiltrating precipitation can pass through and be stored in unsaturated weathered bedrock, forming a deep vadose zone reservoir with significant volume of water accessible to plants during drought years (Rempe and Dietrich, 2018). However, intense water withdrawals due to frequent climate extremes and global urbanization have led to a phenomenal

depletion of water, threatening the sustainability of the critical zone (Brantley et al., 2007). To develop sustainable water management strategies, it is essential to closely monitor the water movement in the critical zone across time and space (Richter Jr. and Mobley, 2009).

Over the past decades, tremendous advances in technology from different disciplines have enabled hydrologic monitoring of the critical zone (Parsekian et al., 2015), enhancing our vision of water cycle dynamics (Brooks et al., 2015; Sprenger et al., 2019). In general, these monitoring tools can be classified into two categories: ground-based techniques and remote sensing. For instance, ground-based instruments include, but not limit to, cosmic-ray neutron sensors, time domain reflectometry, ground penetrating radar and global positioning system (GPS) for soil moisture observations (Dobriyal et al., 2012; Ochsner et al., 2013), and in situ groundwater wells for groundwater monitoring. Whereas remote sensing from space can be used to determine surface soil moisture through L-band measurements (Entekhabi et al., 2010), and to infer the groundwater storage from satellite gravity (Rodell et al., 2009) or interferometric synthetic aperture radar (InSAR; Riel et al., 2018). Nevertheless, since most monitoring methods lack depth-dependent sensitivity, current critical zone hydrological experiments mainly focus on either surface soil moisture or groundwater monitoring, leaving the hydrologic dynamics of vadose zone, the intermediate layer, in response to climatic and anthropogenic activities poorly understood.

Alternatively, given a diffusive noise field, seismic interferometry can extract the Green's function of seismic waves propagating from one seismometer to the other (Campillo and Paul, 2003; Shapiro et al., 2005). In particular, the seismic surface wave that travels along Earth's surface has a dispersive nature with longer periods sensitive to greater depths. Also, the surface wave can be retrieved from weekly or even daily noise data, delivering a superior temporal resolution compared to in situ wells and geodetic measurements. Therefore, by quantifying the velocity change of surface waves using seismic interferometry, time-lapse seismology provides a complementary approach for long-term subsurface monitoring. Indeed, such passive technique has been shown effective in tracking groundwater (Clements and Denolle, 2018; Fokker et al., 2021; Illien et al., 2021; Lecocq et al., 2017) and other geophysical phenomena (Brenguier et al., 2008; Mao et al., 2019; Nakata and Snieder, 2014; Sens-Schönfelder and Wegler, 2006; Wegler and Sens-Schönfelder, 2007; Zhan, 2019). However, limited by the conventional network spacing (typically hundreds or tens of kilometers) used in previous studies, seismic interferometry can

only recover surface waves at relatively long periods ranging from tens of to a few seconds, corresponding to a depth profile of top hundreds of meters, much deeper than that of vadose zone (a few to tens of meters at depth).

In fact, distributed acoustic sensing (DAS), an emerging technology, offers an affordable and scalable solution for deploying ultra-dense seismic arrays. By converting Rayleigh backscattering due to intrinsic fiber impurities to longitudinal strain or strain rate, DAS can repurpose pre-existing telecommunication fiber-optic cables into strings of thousands of vibration sensors (Lindsey and Martin, 2021; Zhan, 2020). As an array of tens of kilometers aperture with a channel spacing of several meters, DAS can record unaliased high-frequency wavefields (Atterholt et al., 2022), featuring a great potential for boosting the spatiotemporal resolution of long-term subsurface monitoring (Tribaldos and Ajo-Franklin, 2021).

5.3 Data and Methods

In this study, we use a DAS array in the Ridgecrest city, California to explore the feasibility of long-term vadose zone monitoring (Figure 5.1a). Supplying over one-third of US's food but suffering from frequent droughts (e.g., a severe drought in 2021), California is currently under intensified water stress. In addition, the Indian Wells Valley where the Ridgecrest DAS cable situated in, is one of the six critically overdrafted groundwater basins in California (Figure 5.1a), urging for subsurface hydrologic monitoring. The Ridgecrest DAS array is converted from a 10-km telecommunication optic cable along a major road (U.S. Route 395 Business) with total 1250 channels in 8-meter spacing. Even though the Ridgecrest DAS array was initially deployed for a rapid response to the 2019 Mw7.1 Ridgecrest earthquake (Li et al., 2021), it has been continuously operating since then and documented almost 2-years acquisition (Jul. 2019 ~ Jun. 2021) with a few short gaps (e.g., Oct. 2019). Following standard ambient noise cross-correlation procedures (Bensen et al., 2007), we first preprocess daily seismograms by removing mean and linear trend, bandpass filtering between 0.1 and 10 Hz, downsampling, time domain moving average normalization and spectral whitening. The 24-hour data are then cut into 40-s segments for each channel. For any given channel pair, all the segments are cross-correlated, normalized, and stacked to present the daily cross-correlation. Regarding the massive computational cost, we downsample the data to 50 Hz and implement GPU-based parallel processing to accelerate the calculation. Once computed, we smooth the daily cross correlations over a 1-week moving window since noise sources recorded on our cable are governed by traffic with weekly periodicity (Yang

et al., 2022). To further enhance the signal-to-noise ratio (SNR), we average the causal and acausal part of each cross-correlation for later dv/v analysis. The 2-years stacked cross-correlation record sections present clear surface waves propagating along the DAS cable from different virtual sources (Figure 5.1b and 5.2). Here we only use an 8-km linear segment along an east-west oriented major road to ensure Rayleigh-type dominated surface waves (Figure 5.1b). These stacked surface waves have been successfully exploited to image subsurface seismic structure and identify fault zones in Ridgecrest (Yang et al., 2022).

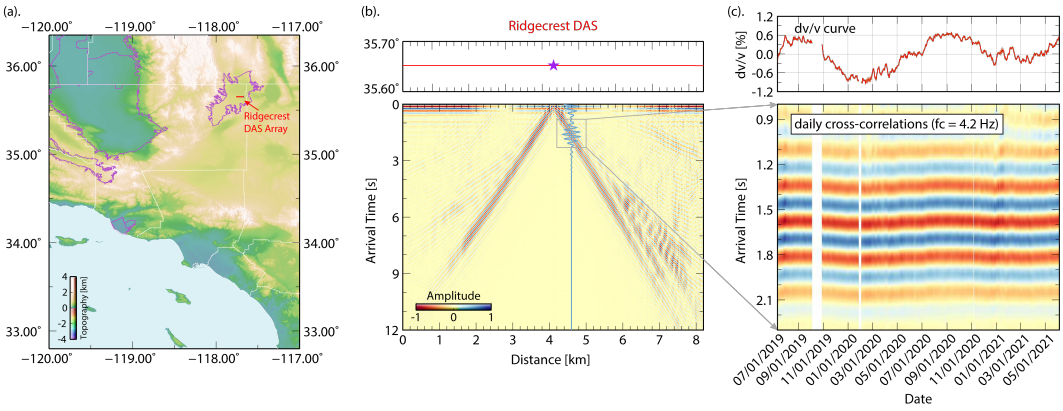

Figure 5.1: Our study region and an example of ambient noise cross-correlations and dv/v measurements. (a). Map view of the Ridgecrest DAS array (red line). The Ridgecrest DAS array is located within the Indian Wells Valley groundwater basin, one of the critically overdrafted groundwater basins in California as delineated by purple lines. The white lines are California county boundaries. (b). An example of ambient noise cross-correlations. Top panel is a zoom-in view of the 8-km Ridgecrest DAS segment along an east-west oriented major road. Purple star denotes the location of our virtual source. Bottom panel shows the 2-years stacked cross-correlation record section for a virtual source in the middle of the array. The cyan waveform presents the cross-correlation function for a particular receiver that is 60-channels apart from the virtual source. Clear surface waves are observed. All the waveforms are half-octave filtered with a center frequency of 4.2 Hz. (c). An example of dv/v results for the channel pair in (b). Bottom panel shows the temporal variation of direct surface wave arrivals at 4.2 Hz. White areas are the data gaps. Top panel shows the corresponding dv/v curve using a cross-spectrum method. Orange errorbars denote uncertainties of dv/v measurements.

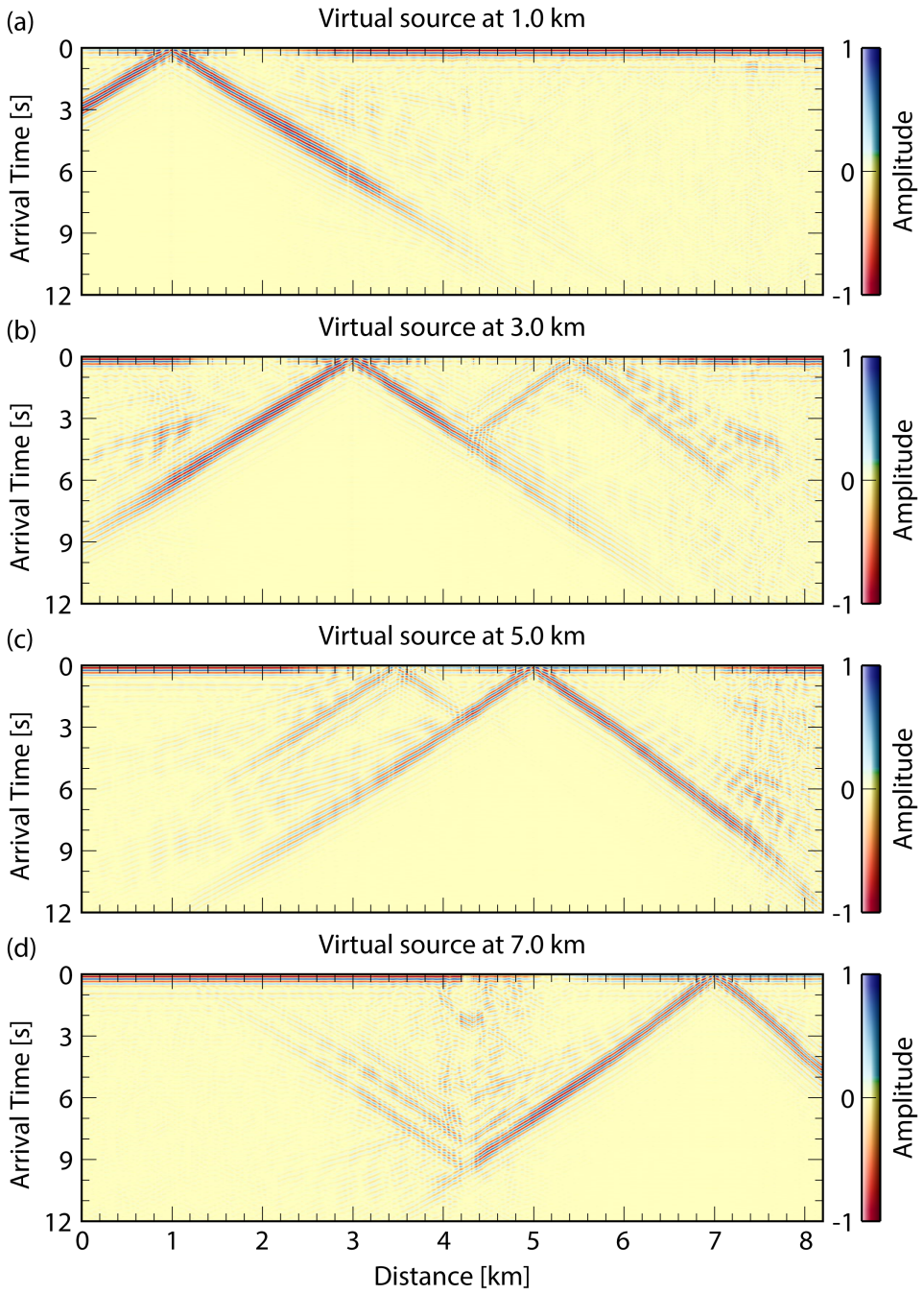

Figure 5.2: 2-year stacked cross-correlation record sections for different virtual sources at distances of (a). 1.0 km, (b). 3.0 km, (c). 5.0 km, and (d) 7.0 km along the DAS cable. The wavefields are half-octave filtered with a center frequency of 4.2 Hz.

5.4 Results

For a particular channel pair spaced 60 channels apart, its daily cross correlations for a half-octave frequency band centered at 4.2 Hz present coherent direct surface

waves with discernable arrival time variations (Figure 5.1c). To quantify, we apply a cross-spectrum method to compute the relative time shifts between 1-s surface wave windows of daily and reference cross correlations (Clarke et al., 2011). The reference waveform is obtained by averaging over all the daily cross correlations and the 1-s window is chosen as 0.5 s before and after the peak of the reference surface wave. Only time shifts with coherency larger than 0.5 are accepted. The resulting arrival time variation is opposite to the relative change in seismic velocity (dv/v). Rather than coda waves (Pacheco and Snieder, 2005; Obermann et al., 2013; Obermann et al., 2016), we use direct surface waves for dv/v estimation in this study because its sensitivity kernel is more deterministic. The resulting dv/v curve presents seasonal variability with negative dv/v in winter and spring and positive dv/v in summer and fall (Figure 5.1c). The dv/v amplitude at 4.2 Hz can vary from -0.9% in February 2020 to 0.6% in September 2019/2020, which is one order of magnitude larger than that in previous studies using longer period surface waves (Clements and Denolle, 2018; Fokker et al., 2021). Also, we spot a remarkable dv/v amplitude difference between the winter of 2020 and 2021 (-0.9% vs. -0.3%), probably owing to a severe drought in 2021. Beyond its seasonality, the dv/v variation also reveals some temporary fluctuations such as a rapid dv/v drop in April 2020 (Figure 5.1c).

Having shown the feasibility of seismic monitoring using a particular DAS channel pair, we proceed to investigate the spatiotemporal evolution of subsurface velocity changes. Rolling along the 8-km DAS cable, dv/v of channel pairs spaced 60 channels apart are measured through the cross-spectrum method and pinpointed to their center locations correspondingly. By satisfying the three-wavelength criterion (Bensen et al., 2007), an inter-channel distance of 60 channels (480 m) is sufficient to develop robust high-frequency (> 2 Hz) Rayleigh waves. The resulting time-lapse images offer a unique opportunity to scrutinize dv/v variations in an unprecedented spatial and temporal resolution (Figure 5.3b). For the case of a center frequency at 4.2 Hz, the dv/v amplitude gradually weakens westward from a maximum peak-to-peak variation of ±1.5% on the east end (6-8 km) to a lowest fluctuation of ±0.5% at 2-3 km with a slight amplification at 0-2 km (Figure 5.3b and 5.4). The lateral variation in dv/v amplitude strikingly correlates with the spatial pattern of shallow-most sediment thickness from 60 m on the east end tapering west to less than 20 m (Figure 5.3a; Yang et al., 2022). This is consistent with previous dv/v observations of large amplitudes in basins (Clements and Denolle, 2018), but on a finer scale. Except for the spatial heterogeneity, we also reinforce the temporal

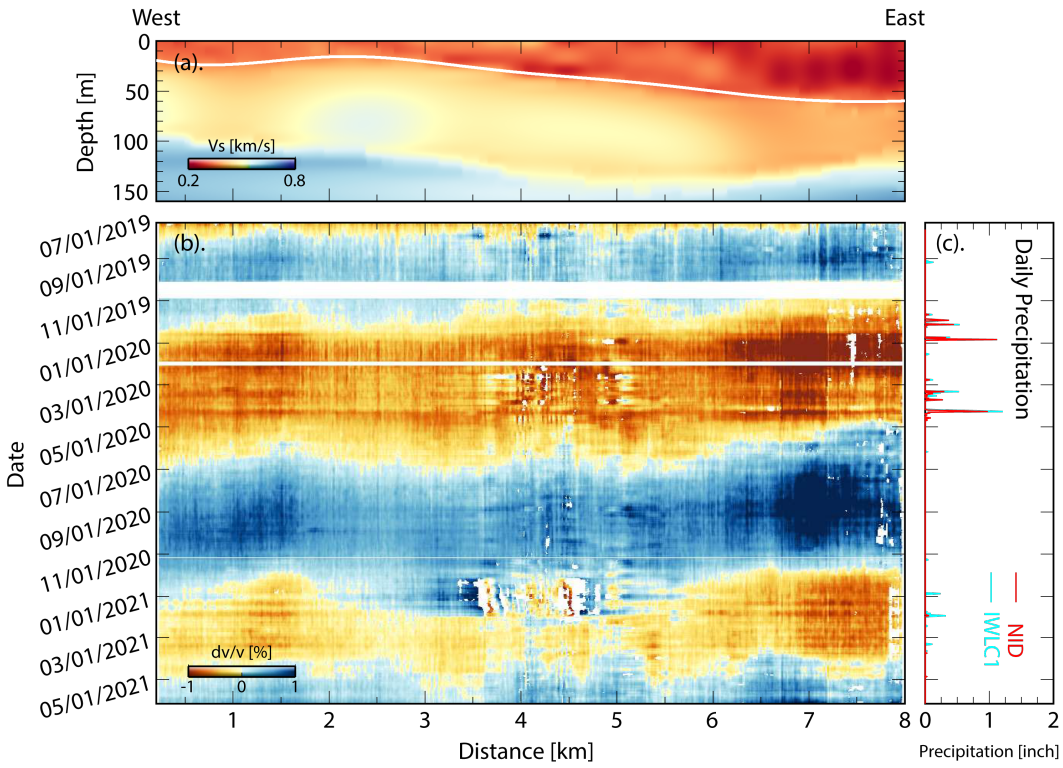

Figure 5.3: The spatiotemporal evolution of dv/v results across the Ridgecrest DAS array and its correlation with tomography and precipitation data. (a). Shear wave tomography model beneath the Ridgecrest DAS cable from Yang et al. (2022) The white line roughly indicates the boundary of the top low-velocity layer. Note the shallow micro-basin at the eastern edge of the Ridgecrest DAS array. (b) dv/v results along the 8-km DAS profile for a half-octave frequency band centered at 4.2 Hz. The white areas indicate either acquisition gaps or bad dv/v measurements with coherency lower than 0.5. (c). Daily precipitation data from two nearby meteorological stations. The cyan and red lines are for NID and IWLC1 station, respectively. Note the correlation between rain fall events and horizontal dv/v anomalies in (b).

variability of dv/v. In response to rainfalls, dv/v can drop temporarily and leave horizontal anomalies across the DAS cable (Figure 5.3b vs. 5.3c). In addition, temporary dv/v variations can be linked to weekly temperature fluctuations when there is no precipitation (Figure 5.5). The thermal expansion of the fiber itself with a coefficient of $10^{-5} \sim 10^{-6}\ K^{-1}$ is too small to account for a temporary dv/v variation of ~0.1%, evoking a temperature control for the subsurface dynamics. On the other hand, our 4.2 Hz dv/v results present coherent seasonal patterns of negative dv/v in wet seasons charging the subsurface and positive dv/v in dry seasons discharging the subsurface (Figure 5.3b). The seasonal variation appears to exhibit a lateral phase lag advancing from east to west (Figure 5.3b), possibly reflecting the permeability

variation along the cable. Because of the severe drought in 2021, less water was charged into the subsurface and consequently the dv/v in 2021 has much lower negative amplitude than that in 2020 (Figure 5.3b and 5.3c).

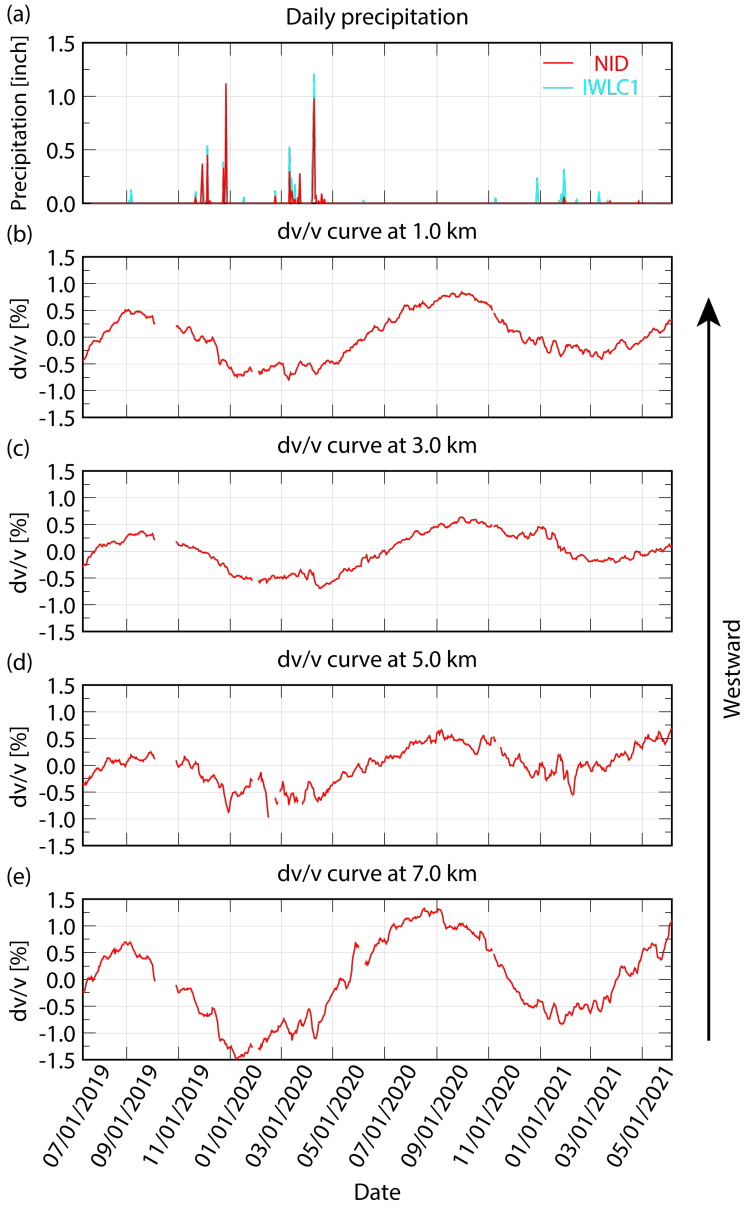

Figure 5.4: dv/v variations along the DAS cable. (a). Daily precipitation data from two nearby meteorological stations and 4.2 Hz dv/v curve at distances of (b). 1.0 km, (c). 3.0 km, (d). 5.0 km, and (e) 7.0 km along the DAS cable. Orange errorbars denote uncertainties of dv/v measurements.

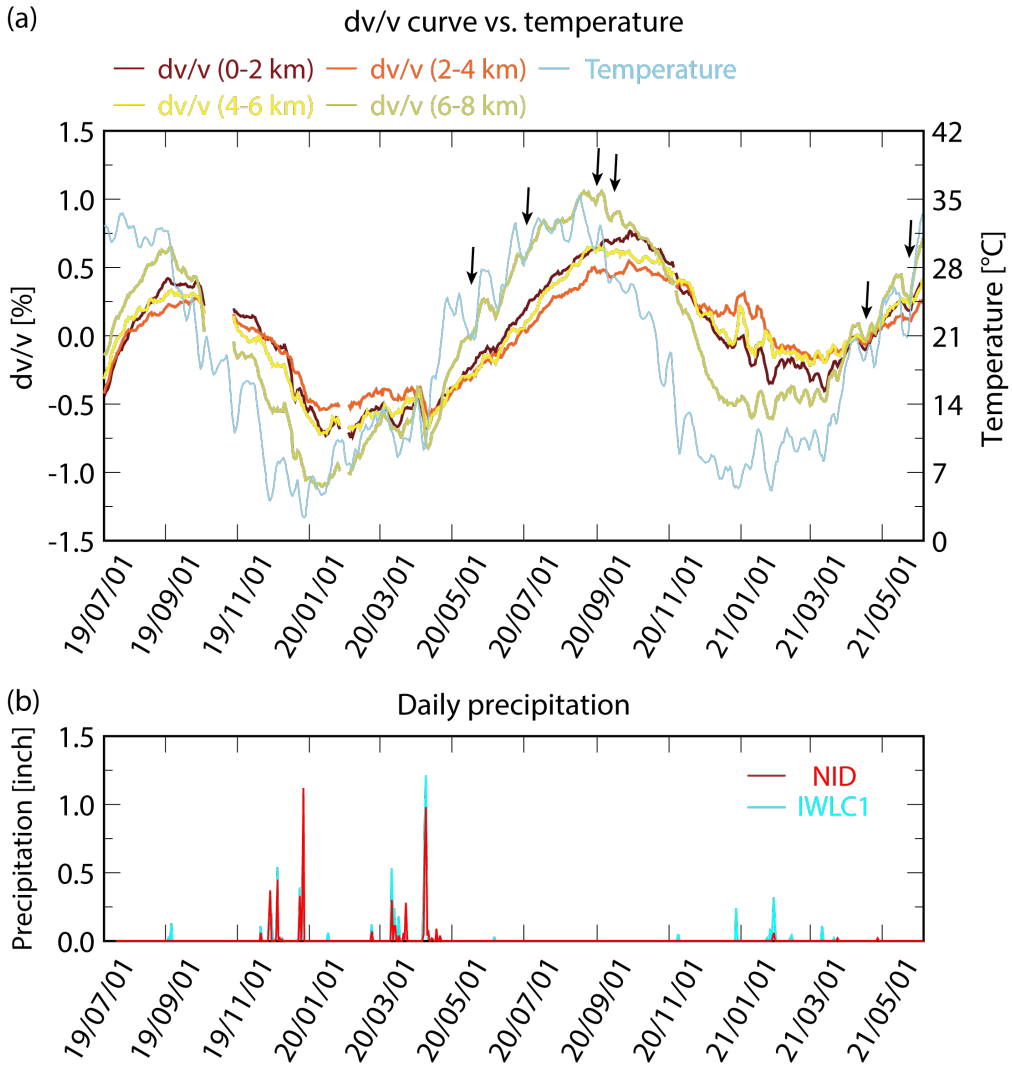

Figure 5.5: Comparison of the temperature and dv/v variations. (a). Daily temperature variation vs. dv/v curves at a distance of 6.6 km for different frequencies. The gray arrows mark the correlations between the temperature and dv/v curves during the dry season. (b). Daily precipitation data from two nearby meteorological stations.

Similarly to the 4.2 Hz scenario above, we measure the seismic velocity changes for other six half-octave frequency bands centered from 2.45 Hz to 7.14 Hz with an interval of 0.18 in the natural log space. Having identified the rainfall and temperature as major sources for temporary dv/v fluctuations, we smooth dv/v measurements with a moving-average window of three months to further explore the seasonal variation. The time-lapse images of different frequency bands all present spatiotemporal evolution similar to that of the 4.2 Hz case, but with larger amplitudes at higher frequency (Figure 5.6).

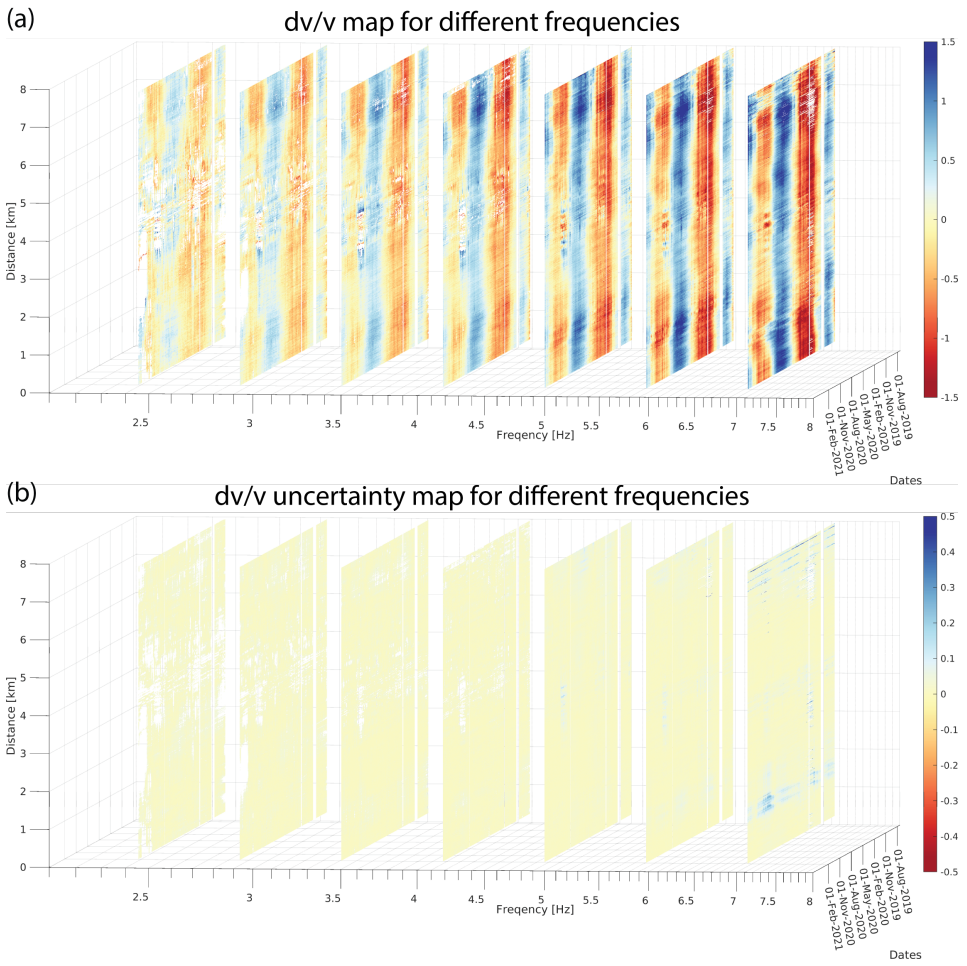

Figure 5.6: Frequency dependent dv/v maps. (a). dv/v map for different frequencies. (b). dv/v uncertainty map for different frequencies.

For example, the dv/v amplitude on the east side of our DAS cable (6.6 km) increases from ±0.4% at 2.45 Hz to ±1.5% at 7.14 Hz, implying a shallow force driving the seasonality (Figure 5.7a). To quantify its depth extent, we calculate sensitivity kernels for a set of 10-m layers at depths ranging from the surface to 70 m with an interval of 10 m (Figure 5.7b). Based on the reference velocity profile in Figure 5.3a, the sensitivity kernel is given as the dispersion curve difference by applying a local velocity perturbation to each layer (Herrmann, 2013). To intuitively compare the depth sensitivity kernels to observations, we focus on slope changes of dv/v as a function of frequency by scaling dv/v to the same values at 2.93 Hz (Figure 5.7b). The uppermost 10 m layer sensitivity kernel well captures our dv/v observations across a broad frequency band from approximately 2 Hz to 8 Hz (Figure 5.7b). Whereas at greater depths, the sensitivity kernels in response to a seismic velocity perturbation are either too steep to fit observations (e.g., 10-20 m)

or present opposite trends of dv/v amplitude decaying with frequency (e.g., >40 m; Figure 5.7b). Furthermore, on the west end of the DAS cable, the frequency analysis of dv/v yields similar results (Figure 5.8), fortifying a seasonal manifestation from the top 10 m.

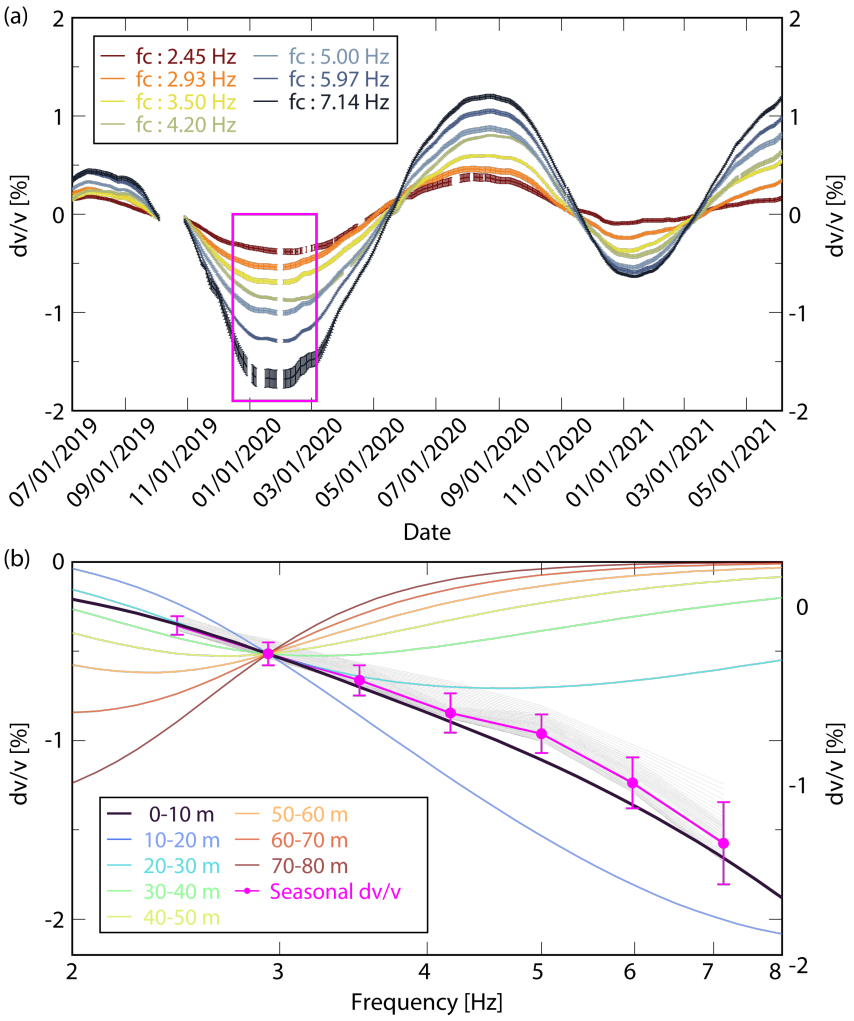

Figure 5.7: Frequency analysis of dv/v measurements indicates a shallow source (top 10 m) for the seasonal variation. (a). dv/v curves of different frequency bands ranging from 2.45 Hz to 7.14 Hz at a location of 6.6 km along the cable. The errorbars denote the uncertainty of dv/v measurements. The magenta box indicates the dv/v observations used for frequency analysis. (b). Comparison between dv/v observations and sensitivity kernels. Solid lines in different colors represent dv/v sensitivity kernels as a function of frequency for different 10-m layers at depths ranging from the surface to 70 m with an interval of 10 m. The gray lines are daily dv/v observations within the magenta box in (a). The magenta line with errorbars represents the median dv/v curve with the 95% confidence interval. All the curves are scaled to the same dv/v values at 2.93 Hz to solely focus on the slope changes.

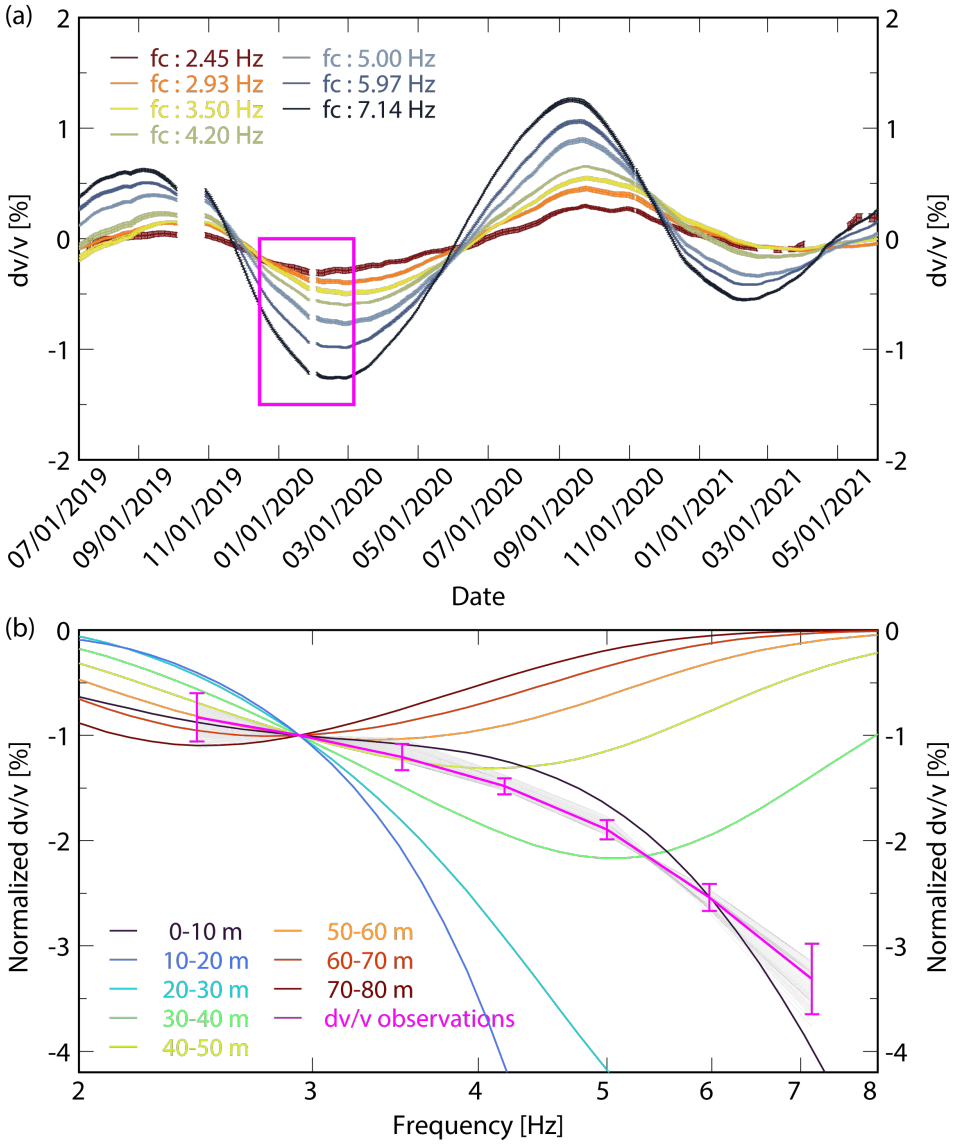

Figure 5.8: Same as Figure 5.7, but for a location of 0.7 km on the west side of the DAS cable. (a). dv/v curves of different frequency bands ranging from 2.45 Hz to 7.14 Hz. (b). Comparison between normalized dv/v observations and sensitivity kernels.

5.5 Discussion

Even though its temporary perturbation can modulate our dv/v observations on a weekly scale, the temperature is not the dominate driving force for the dv/v seasonal variation. This is supported by significant dv/v amplitude differences between wet seasons in 2020 (water year) and 2021 (drought year), but the temperature steadily varies with a constant annual amplitude (Figure 5.9). Moreover, the seasonal variation in temperature advances the dv/v by roughly one month, whereas on a

weekly scale, both temperature and dv/v variations have zero phase lag (Figure 5.9 and 5.11a). Therefore, we suggest that it is water saturation in the uppermost 10 m controlling our observed seasonal cycle in dv/v.

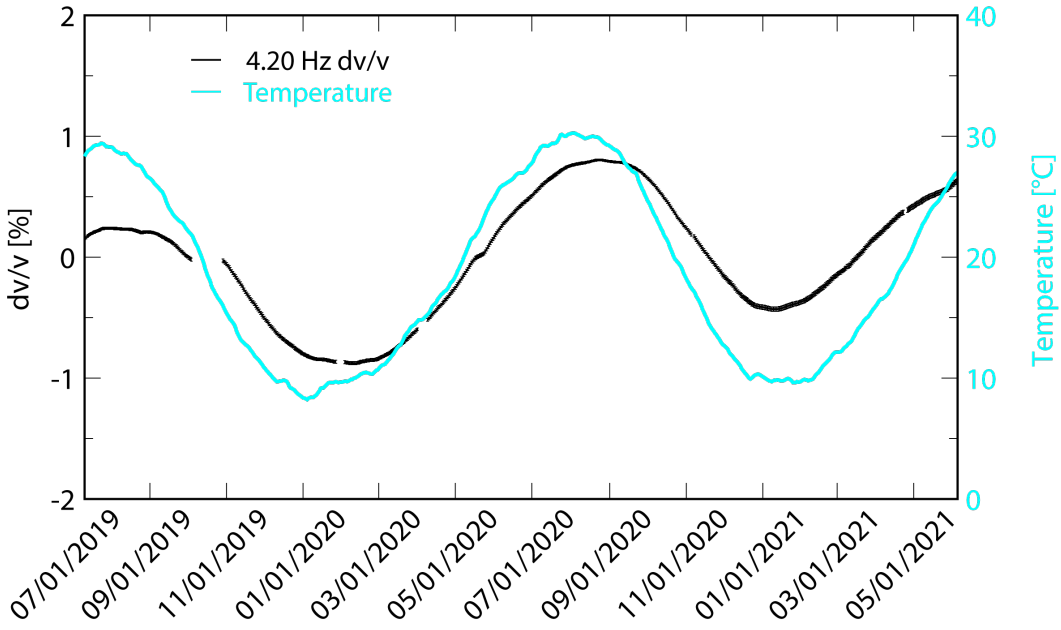

Figure 5.9: Comparison of seasonal variations in dv/v (black line) and temperature (cyan line).

Using long period surface waves, previous seismic studies attribute the seasonal pattern of dv/v measurements to groundwater fluctuations. However, the groundwater table beneath our Ridgecrest DAS cable is ~70 m, which is too deep for the groundwater evaporation front to reach a near-surface depth given the sandy soil texture in our study region (Shokri, 2019). On the other hand, the frequency analysis with absolute dv/v amplitudes indicates a maximum velocity reduction of 7% in the top 10 m (Figure 5.10a and 5.10b), which in turn would perturb long periods (1~2 s) dv/v measurements up to a value of ~0.4% (Figure 5.10c). Such dv/v variation is about the same order of magnitude as previous observations in a typical frequency band of 0.05~4 Hz. Therefore, we suggest that the shallow soil layer cannot be neglected and should be considered in long period dv/v observations.

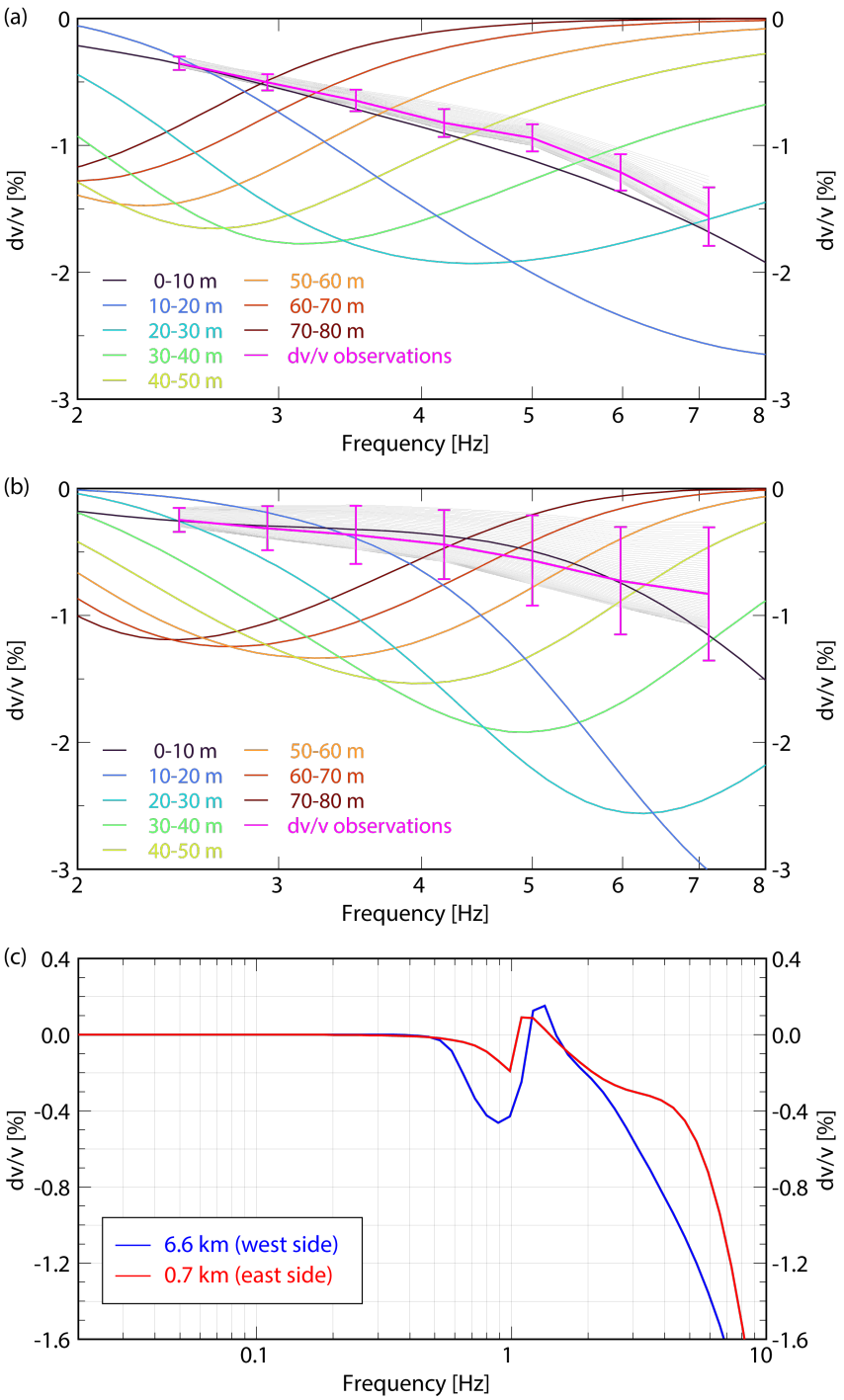

Figure 5.10: Comparison between absolute dv/v amplitudes and sensitivity kernels for a location of (a). 6.6 km and (b). 0.7 km along the cable. The sensitivity kernels are calculated for a velocity reduction of 7.0% in each layer. (c). The effect of a 7% velocity reduction within the uppermost 10 m on long-period dv/v measurements.

Lastly, to reconcile our dv/v observations on temporal scales, we propose a vadose zone water reservoir model which can act as a buffer zone (Figure 5.11c). When there

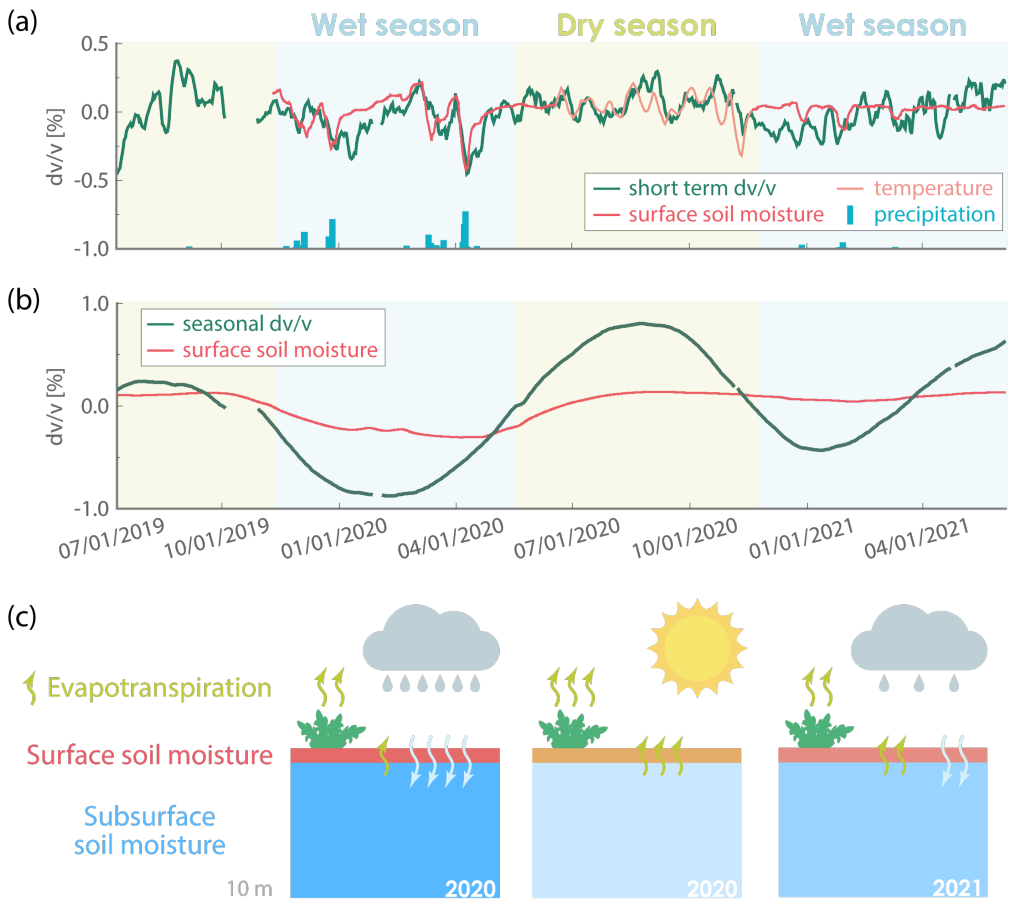

Figure 5.11: Summary of observed short-term and seasonal results. (a). Comparison of temporary variations in dv/v measurements, temperature fluctuations and surface soil moisture. (b). Seasonal dv/v variation and the dv/v contribution from surface soil moisture only. (c). Cartoon for the vadose zone water cycle. The year of 2021 has less precipitation than the year of 2020.

is abundant water occupying the pore-space of soil material in the vadose zone, the subsurface seismic velocity can decrease with increasing water saturation as a result from the increase in subsurface soil density, and vice versa (Knight et al., 1998). On a temporary scale, rainfall events could charge the subsurface, resulting a drop in dv/v (Figure 5.11a). Similarly, rapid temperature fluctuation might affect the root zone water saturation through evapotranspiration (Figure 5.11a and 5.11c). For arid regions like Ridgecrest, it is so dry that the seismic velocity change approximately follows a linear scaling with water saturation (Knight et al., 1998). Indeed, we find a good correlation between the surface soil moisture measurement (Entekhabi et al., 2010) and our dv/v in wet seasons (Figure 5.11a) with a 0.06% change in dv/v amplitude per one percent change in surface soil moisture. With this scaling, we find that surface soil moisture only is inadequate to explain our dv/v seasonal

variation with a contribution to dv/v ampltidue up to 0.3% (Figure 5.11b), favoring a seasonal source in the vadose zone. In this manner, we suggest that more water can be stored in the vadose zone during wet seasons resulting in negative dv/v (Figure 5.11b vs. 5.11c). Meanwhile, evapotranspiration during dry seasons will discharge the vadose zone water saturation, leading to positive dv/v (Figure 5.11b vs. 5.11c). Such hydrologic cycle naturally explains the dv/v amplitude differences between 2020 and 2021 (Figure 5.11c). Nonetheless, the surface soil moisture and seasonal dv/v measurements appear to have a phase shift (Figure 5.11b), which may indicate an important role of evapotranspiration diffusing through a certain thickness. Yet, to quantitatively link our dv/v observations to water cycle in the vadose zone requires more detailed investigations.

5.6 Conclusion

With the two years of Ridgecrest DAS data, we perform time-lapse interferometry to track water in the vadose zone. Using the seismic velocity change as an indicator, our results demonstrate that DAS-based noise monitoring is capable of capturing subsurface hydrology processes in unprecedented spatiotemporal resolution. Such fine-scale monitoring of water in the vadose zone is significant for sustainable water management. Although the physics linking the dv/v observations and hydrology dynamics requires further investigation, the observation we report here highlights the potential of DAS for long-term subsurface water monitoring as an efficient and inexpensive tool.

5.7 Acknowledgement

The authors are grateful to the instrument and field support provided by Martin Karrenbach, Vlad Bogdanov, and Lisa LaFlame of OptaSense Inc., Thomas Coleman of Silixa Inc., and Andrew Klesh of JPL. We thank the Digital 395 and JPL for providing fiber access promptly after the Ridgecrest earthquake. We are also grateful to Ethan Williams, Yan Yang, and Xin Wang for helpful discussions and suggestions. The California critically overdrafted groundwater basin boundary shapefiles are downloaded from https://sgma.water.ca.gov/webgis/?appid=SGMADataViewer#boundaries (Last accessed in March 2022). The daily temperature and precipitation data can be downloaded from https://cdec.water.ca.gov/ and https://www.cnrfc.noaa.gov/rainfall_data.php, respectively (Last accessed in April 2022). The groundwater table information in Indian Wells Valley is available from https://iwvgsp.com/map/map.php (Last accessed in April 2022).

References

Atterholt, J. et al. (2022). A unified wavefield-partitioning approach for distributed acoustic sensing. In: *Geophysical Journal International* 228.2, pp. 1410–1418. DOI: 10.1093/gji/ggab407.

Bensen, G. et al. (2007). Processing seismic ambient noise data to obtain reliable broad-band surface wave dispersion measurements. In: *Geophysical Journal International* 169.3, pp. 1239–1260. DOI: 10.1111/j.1365-246X.2007.03374.x.

Brantley, S. L. et al. (2007). Crossing disciplines and scales to understand the critical zone. In: *Elements* 3.5, pp. 307–314. DOI: 10.2113/gselements.3.5.307.

Brenguier, F. et al. (2008). Postseismic relaxation along the San Andreas fault at Parkfield from continuous seismological observations. In: *Science* 321.5895, pp. 1478–1481. DOI: 10.1126/science.1160943.

Brooks, P. D. et al. (2015). Hydrological partitioning in the critical zone: Recent advances and opportunities for developing transferable understanding of water cycle dynamics. In: *Water Resources Research* 51.9, pp. 6973–6987. DOI: 10.1002/2015WR017039.

Campillo, M. and A. Paul (2003). Long-range correlations in the diffuse seismic coda. In: *Science* 299.5606, pp. 547–549. DOI: 10.1126/science.1078551.

Clarke, D. et al. (2011). Assessment of resolution and accuracy of the Moving Window Cross Spectral technique for monitoring crustal temporal variations using ambient seismic noise. In: *Geophysical Journal International* 186.2, pp. 867–882. DOI: 10.1111/j.1365-246X.2011.05074.x.

Clements, T. and M. A. Denolle (2018). Tracking groundwater levels using the ambient seismic field. In: *Geophysical Research Letters* 45.13, pp. 6459–6465. DOI: 10.1029/2018GL077706.

Cuthbert, M. O. et al. (2019). Observed controls on resilience of groundwater to climate variability in sub-Saharan Africa. In: *Nature* 572.7768, pp. 230–234. DOI: 10.1038/s41586-019-1441-7.

Dobriyal, P. et al. (2012). A review of the methods available for estimating soil moisture and its implications for water resource management. In: *Journal of Hydrology* 458, pp. 110–117. DOI: 10.1016/j.jhydrol.2012.06.021.

Döll, P. et al. (2012). Impact of water withdrawals from groundwater and surface water on continental water storage variations. In: *Journal of Geodynamics* 59, pp. 143–156. DOI: 10.1016/j.jog.2011.05.001.

Entekhabi, D. et al. (2010). The soil moisture active passive (SMAP) mission. In: *Proceedings of the IEEE* 98.5, pp. 704–716. DOI: 10.1109/JPROC.2010.2043918.

Fokker, E. et al. (2021). Physics-based relationship for pore pressure and vertical stress monitoring using seismic velocity variations. In: *Remote Sensing* 13.14, p. 2684. DOI: 10.3390/rs13142684.

Grant, G. E. and W. E. Dietrich (2017). The frontier beneath our feet. In: *Water Resources Research* 53.4, pp. 2605–2609. DOI: 10.1002/2017WR020835.

Herrmann, R. B. (2013). Computer programs in seismology: An evolving tool for instruction and research. In: *Seismological Research Letters* 84.6, pp. 1081–1088. DOI: 10.1785/0220110096.

Illien, L. et al. (2021). Subsurface moisture regulates Himalayan groundwater storage and discharge. In: *AGU Advances* 2.2, e2021AV000398. DOI: 10.1029/2021AV000398.

Knight, R. et al. (1998). Acoustic signatures of partial saturation. In: *Geophysics* 63.1, pp. 132–138. DOI: 10.1190/1.1444305.

Lall, U. et al. (2020). A snapshot of the world's groundwater challenges. In: *Annual Review of Environment and Resources* 45, pp. 171–194. DOI: 10.1146/annurev-environ-102017-025800.

Lecocq, T. et al. (2017). Monitoring ground water storage at mesoscale using seismic noise: 30 years of continuous observation and thermo-elastic and hydrological modeling. In: *Scientific Reports* 7.1, pp. 1–16. DOI: 10.1038/s41598-017-14468-9.

Li, Z. et al. (2021). Rapid response to the 2019 Ridgecrest earthquake with distributed acoustic sensing. In: *AGU Advances* 2.2, e2021AV000395. DOI: 10.1029/2021AV000395.

Lindsey, N. J. and E. R. Martin (2021). Fiber-optic seismology. In: *Annual Review of Earth and Planetary Sciences* 49, pp. 309–336. DOI: 10.1146/annurev-earth-072420-065213.

Mao, S. et al. (2019). High temporal resolution monitoring of small variations in crustal strain by dense seismic arrays. In: *Geophysical Research Letters* 46.1, pp. 128–137. DOI: 10.1029/2018GL079944.

Nakata, N. and R. Snieder (2014). Monitoring a building using deconvolution interferometry. II: Ambient-vibration analysis. In: *Bulletin of the Seismological Society of America* 104.1, pp. 204–213. DOI: 10.1785/0120130050.

National Research Council (2001). *Basic Research Opportunities in Earth Science*. National Academies Press. ISBN: 978-0-309-07133-8. DOI: 10.17226/9981.

Obermann, A. et al. (2013). Depth sensitivity of seismic coda waves to velocity perturbations in an elastic heterogeneous medium. In: *Geophysical Journal International* 194.1, pp. 372–382. DOI: 10.1093/gji/ggt043.

Obermann, A. et al. (2016). Lapse-time-dependent coda-wave depth sensitivity to local velocity perturbations in 3-D heterogeneous elastic media. In: *Geophysical Journal International* 207.1, pp. 59–66. DOI: 10.1093/gji/ggw264.

Ochsner, E. et al. (2013). State of the art in large-scale soil moisture monitoring. In: *Soil Science Society of America Journal*, pp. 1–32. DOI: 10.2136/sssaj2013.03.0093.

Oki, T. and S. Kanae (2006). Global hydrological cycles and world water resources. In: *Science* 313.5790, pp. 1068–1072. DOI: 10.1126/science.1128845.

Pacheco, C. and R. Snieder (2005). Time-lapse travel time change of multiply scattered acoustic waves. In: *The Journal of the Acoustical Society of America* 118.3, pp. 1300–1310. DOI: 10.1121/1.2000827.

Parsekian, A. et al. (2015). Multiscale geophysical imaging of the critical zone. In: *Reviews of Geophysics* 53.1, pp. 1–26. DOI: 10.1002/2014RG000465.

Rempe, D. M. and W. E. Dietrich (2018). Direct observations of rock moisture, a hidden component of the hydrologic cycle. In: *Proceedings of the National Academy of Sciences* 115.11, pp. 2664–2669. DOI: 10.1073/pnas.1800141115.

Richter Jr., D. d. and M. L. Mobley (2009). Monitoring Earth's critical zone. In: *Science* 326.5956, pp. 1067–1068. DOI: 10.1126/science.1179117.

Riel, B. et al. (2018). Quantifying ground deformation in the Los Angeles and Santa Ana Coastal Basins due to groundwater withdrawal. In: *Water Resources Research* 54.5, pp. 3557–3582. DOI: 10.1029/2017WR021978.

Rodell, M. et al. (2009). Satellite-based estimates of groundwater depletion in India. In: *Nature* 460.7258, pp. 999–1002. DOI: 10.1038/nature08238.

Seneviratne, S. I. et al. (2010). Investigating soil moisture—climate interactions in a changing climate: A review. In: *Earth-Science Reviews* 99.3-4, pp. 125–161. DOI: 10.1016/j.earscirev.2010.02.004.

Sens-Schönfelder, C. and U. Wegler (2006). Passive image interferometry and seasonal variations of seismic velocities at Merapi Volcano, Indonesia. In: *Geophysical research letters* 33.21. DOI: 10.1029/2006GL027797.

Shapiro, N. M. et al. (2005). High-resolution surface-wave tomography from ambient seismic noise. In: *Science* 307.5715, pp. 1615–1618. DOI: 10.1126/science.1108339.

Shokri, N. (2019). Comment on "analytical estimation show low depth-independent water loss due to vapor flux from deep aquifers by John S. Selker (2017)". In: *Water Resources Research* 55.2, pp. 1730–1733. DOI: 10.1029/2018WR023347.

Sprenger, M. et al. (2019). The demographics of water: A review of water ages in the critical zone. In: *Reviews of Geophysics* 57.3, pp. 800–834. DOI: 10.1029/2018RG000633.

Tribaldos, V. R. and J. B. Ajo-Franklin (2021). Aquifer monitoring using ambient seismic noise recorded with distributed acoustic sensing (DAS) deployed on dark fiber. In: *Journal of Geophysical Research: Solid Earth* 126.4, e2020JB021004. DOI: 10.1029/2020JB021004.

Wegler, U. and C. Sens-Schönfelder (2007). Fault zone monitoring with passive image interferometry. In: *Geophysical Journal International* 168.3, pp. 1029–1033. DOI: 10.1111/j.1365-246X.2006.03284.x.

Yang, Y. et al. (2022). Sub-kilometer correlation between near-surface structure and ground motion measured with distributed acoustic sensing. In: *Geophysical Research Letters*, e2021GL096503. DOI: 10.1029/2021GL096503.

Zhan, Z. (2019). Seismic noise interferometry reveals transverse drainage configuration beneath the surging Bering Glacier. In: *Geophysical Research Letters* 46.9, pp. 4747–4756. DOI: 10.1029/2019GL082411.

Zhan, Z. (2020). Distributed acoustic sensing turns fiber-optic cables into sensitive seismic antennas. In: *Seismological Research Letters* 91.1, pp. 1–15. DOI: 10.1785/0220190112.

Chapter 6

CONCLUSION AND FUTURE DIRECTION

In this thesis, I present several independent case studies where I use seismic interferometry methods to gain insights on the water below the surface. In Chapter 2, I apply inter-source interferometry to untangle the potentially subtle seismic signature of metastable olivine wedge (MOW) from complex shallow Earth heterogeneities. I first validate the feasibility to retrieve the P wave strain Green's functions between two deep earthquakes for two synthetic scenarios with and without MOW. With real data from Hi-net, I obtain interferometric observations for six deep earthquake pairs in the Japan subduction zone. By simultaneously fitting the 2 Hz and 5 Hz waveform details, I resolve the MOW geometry to be ~30 km thick at 410-km depth and gradually thinning to a depth of 580 km at least. The existence and dimension of MOW support transformational faulting of metastable olivine as the initiation mechanism of deep earthquakes, while M7.0+ events probably rupture beyond the wedge. Furthermore, the slab core must be dehydrated at shallower depth and only transports negligible amount of water into the mantle transition zone (MTZ).

Chapter 3 describes a case study where I apply inter-source interferometry to interrogate the small-scale intraslab scatterers below 410 km. With numerical simulations for various intra-slab heterogeneity scenarios, I first validate the robustness of the MOW model proposed in Chapter 2 and find that strong scattering models tend to complicate the high-frequency waveforms, leading to a worse fit to the interferometric observations. To explain the 5 Hz waveforms, I quantify the intra-slab heterogeneity level to be less than 1.0% below 410 km. Combining with strong scattering observations (~2.5%) at intermediate depths, the intra-slab heterogeneity weakens as the slab subducts. Given the pervasive faults extending to the oceanic lithosphere at the Japan trench and the existence of a MOW in the MTZ, I propose that the scatterers are caused by hydration processes in the outer rise. The weakening of scattering strength reveals that the dehydration process of the slab core must be complete before reaching 410 km and could possibly lead to hydration of the slab crust and formation of dense oxyhydroxide phases. Even though focusing on different seismic scales, Chapter 2 and Chapter 3 point toward a consistent picture of a dry slab core in the MTZ beneath the Japan Sea.

In Chapter 4, borrowing the idea from inter-source interferometry, I develop a slab operator method to resolve large-scale slab velocity perturbations. Using synthetic waveforms from deep earthquake pairs with one being a reference event sharing similar raypath with the other event except for the slab side, I illustrate the feasibility of estimating the slab velocity perturbation through an apparent attenuation factor (t_s^*). In general, t_s^* increases with the slab velocity anomaly for a set of scenarios of different dip angles. The slab operator method is shown insensitive to complicated source processes, hosting a great potential for utilizing a large amount of earthquake waveforms. Applying to the Kuril subduction zone, I determine a velocity amplitude of 4% within the slab core, which is consistent with previous waveform modeling study. For global applications, more regional seismic networks should be incorporated for achieving appropriate source-receiver configurations.

Lastly, Chapter 5 presents a case study of vadose zone water monitoring with distributed acoustic sensing (DAS). By performing inter-receiver interferometry to 2-years of ambient noise recorded on the Ridgecrest DAS array, I reconstruct surface waves propagating along the 8-km cable and observe the spatiotemopral evolution of subsurface seismic change (dv/v) in high resolution. I find a striking correlation between the lateral variation of dv/v amplitudes and the shallow sediment thickness derived from seismic tomography. The temporary dv/v fluctuations can be related to occasional rainfalls and temperature perturbations. Moreover, the seasonality of dv/v measurements reflects subsurface being charged and discharged in wet and dry seasons, respectively. For a severe drought in 2021, the observed dv/v amplitude is much smaller than that in 2020. To further explain the frequency dependent dv/v observations, I suggest a water reservoir in vadose zone (top 10 m) modulating the water saturation seasonally. The time-lapse dv/v result demonstrates the feasibility of DAS for long-term subsurface water monitoring.

As shown in each individual case study, new observational insights of water below the surface can not be achieved without the advance in seismic instrumentation (e.g., DAS) or the development of seismic interferometry. Looking ahead, several directions are worth further explorations for bringing new understandings to multiple disciplines. Firstly, by turning deep earthquakes into virtual receivers, inter-source interferometry can better image the seismic structure between earthquakes at depth. For example, the seismic structure and dynamics of the slab core at intermediate depths (70~350 km) are yet poorly constrained, leaving the origin of lower plane seismicity mysterious (e.g., dehydration vs. thermal runaway). Inter-source interferometry is placed at a unique position to tackle this problem with dense seismic

networks. Secondly, water exists everywhere above, on and below the surface. Efforts in tracking water must not be stopped by any means. For example, it is still debatable how much water has been stored in the MTZ. High-frequency body waves bouncing from the 410 and 660 discontinuity and maybe even small-scale scatterers could be retrieved by inter-receiver interferometry or from direct observations of reflected seismic phases (i.e., P'P'). New observations might help to shed light on the thermal and chemical properties of the Earth's interior. On the other hand, for water above the surface, integrated marine instruments including OSBs and hydrophones could contribute to understand the hydrothermal activity or even ocean warming. Thirdly, from an instrumentation perspective, DAS is still in its infancy but has a great potential in a variety of geological environments, in particular for, places logistically challenging for conventional seismometers (e.g., ocean, volcano and glacier). For instance, closely listening to the glacier movement with DAS is essential to understand the stability of ice sheet over years, especially under the intensified climate change.